UNIVERSITÉ DE STRASBOURG

Thèse présentée pour obtenir le titre de

Docteur de l'Université de Strasbourg

Discipline : Physique

Molecular Dynamics Simulations of Sheared Polymer Brushes

André Galuschko

Thèse soutenue publiquement le 6 septembre 2010

Membres du Jury :

Directeur de thèse : **J. Baschnagel**

Professeur UDS, ICS, Strasbourg

Co-directeur de thèse : **J. Wittmer**

Directeur de recherche, ICS, Strasbourg

Examinateur : **T. Charitat**

Professeur UDS, ICS, Strasbourg

Rapporteur externe : **H. Xu**

Professeur UPV, LPMD, Metz

Rapporteur externe : **J.-P. Ryckaert**

Professeur ULB, LPMM, Bruxelles

Invité : **T. Kreer**

Docteur, Universität Mainz

INSTITUT
Charles
SADRON
CNRS - UdS - STRASBOURG

Abstract

Polymers end-grafted onto surfaces ("polymer brushes") display extraordinary tri-
bological properties. When two polymer-brushes coated surfaces come in contact,
they strongly repel one another and interpenetrate weakly. Thus, opposing brushes
can carry high normal loads, whereas simultaneously lateral sliding resistance may
be extremely small. First experiments on polymer brushes under shear were carried
out by J. Klein [*Annu. Rev. Matter. Sci.* **26**, 581 (1996)] reporting that the re-
sulting friction coefficients may be orders of magnitude smaller than those found in
dry friction. Therefore, polymer brushes have important applications as lubricants.
Due to limitations of the experiments, information about molecular factors causing
the rheological response is not provided, such that the interpretation of the observed
phenomena remain challenging for theoretical description.

The main subject of this thesis is to investigate the complex fluid response utiliz-
ing Molecular Dynamics simulation of the generic bead-spring model by Kremer and
Grest [*J. Chem. Phys.* **92**, 5057 (1990)] as a "high-resolution microscope" to resolve
molecular structure beyond static equilibrium. The model system contains charge-
neutral polymer chains attached to two substrates under good solvent condition,
creating two opposing polymer brushes. Furthermore, explicit solvent molecules
(Lennard-Jones dimers) are added to the system simulating an incompressible fluid.
The Dissipative Particle Dynamics Thermostat is implemented to keep the temper-
ature constant fulfilling Newtons third law, thus assuring momentum conservation
and simulating hydrodynamic correlations correctly. Those systems are compared
to solvent-free counterparts while varying the wall distance between the grafted lay-
ers and their molecular parameters, such as chain length and grafting density.This
work employs the planar Couette flow geometry, where both opposing brushes are
strongly compressed and a simple shear flow is applied by moving the substrates
laterally in opposite directions. Approaching the problem with scaling theory, the
interpenetration length of the compressed bilayer at equilibrium is introduced as a
relevant length scale. This allows to predict the dependence of the critical shear rate,
which separates linear and non-linear behavior, on compression and the molecular
parameters of the bilayer in stationary shear motion. A strong correlation is found
between the microscopic response (e.g. lateral chain extension) and macroscopic
transport properties (e.g. fluid viscosity) beyond Newtonian response. In agree-
ment with the developed theory, the simulation reveals simple power-laws in those

observables. Additionally, a very good agreement with recent experimental data by Schorr *et. al.* [*Macromolecules* **36**, 389 (2003)] is demonstrated to substantiate our study.

Besides the stationary regimes (equilibrium and steady state) the transient regime, starting from a steady shear situation and inverting the shear direction is explored. The presence of the explicit solvent, which is carrying extra inertia, is changing the responses dramatically versus the complementary systems with the continuous solvent. All these cases are present in the experimental setup in terms of a single transitional regime, the oscillatory regime. A connection to all those cases is established, discussing the reachability of those limits by a standard macroscopic rheology-like analysis. Finally, the dissertation summarizes and discusses the limitation of the mean field theory and revisits the brushes at static equilibrium. The interface is defining the frictional properties, a simple Green-Kubo relation introduced by Bocquet and Barrat [*Phys. Rev. Lett.* **70**, 2726 (1993)] evaluates the fluctuations at the junction. A non-trivial behavior of long time correlations inside the interface of the double layer is illustrated and will give rise for further studies.

Keywords: Nano-Tribology, Rheology, Lubrication, Friction, Polymer Brush

Résumé

Les polymères greffés sur une surface ("brosse de polymères") présentent des propriétés tribologiques uniques. Quand deux brosses de polymères sont en contact, elles se repoussent fortement et on observe une faible interpénétration. De plus ces brosses peuvent supporter de fortes charges tout en affichant une très faible friction latérale. Les premières expériences sur les brosses de polymères sous contrainte de cisaillement ont été réalisées par J. Klein [*Annu. Rev. Matter. Sci.* **26**, 581 (1996)]. Celles-ci ont démontré que les coefficients de friction de ces brosses pouvaient être de plusieurs ordres de grandeur inférieurs à ceux observés pour le frottement solide. D'ou le grand potentiel applicatif de ces brosses dans le domaine de la lubrification. En raison des limitations des expériences réalisées, les phénomènes microscopiques à l'origine de ces propriétés n'ont pas pu être définis et l'interprétation de ces résultats par une description théorique reste un important challenge.

Le principal objectif de cette thèse est d'enquêter sur la réponse des brosses polymères à une contrainte de cisaillement par le biais de simulations de dynamique moléculaire utilisant le modèle générique bille-ressort de Kremer et Grest [*J. Chem. Phys.* **92**, 5057 (1990)]. Ces simulations peuvent être vues comme un "microscope à haute résolution" qui va fournir des informations microscopiques au-delà du simple cas de la description statistique du système à l'équilibre. Le système modèle de brosses de polymères utilisé lors des simulations numériques est constitué de chaînes de polymères neutres et monodisperses attachées à deux substrats plans sous condition de bon solvant. De plus, des molécules de solvant (dimères Lennard-jones) sont ajoutés au système pour fournir les propriétés d'un fluide incompressible. Le thermostat DPD (Dissipative Particle Dynamics) est implémenté pour maintenir la température du système à une valeur donnée tout en assurant la conservation de la quantité de mouvement et des propriétés hydrodynamiques du système. Ces systèmes sont comparés à leur équivalent sans solvant explicite tout en faisant varier la distance entre les substrats, leurs paramètres moléculaires comme la densité et la longueur des chaines greffées à la surface des substrats. Ces travaux ont employé une conformation géométrique qui permet un cisaillement de type "écoulement de Couette". C'est à dire que les deux brosses opposées sont soumises à une forte pression et un cisaillement simple est appliqué en imprimant des mouvements latéraux de sens opposés aux deux substrats. Si on interprète le système avec des lois d'échelle, la distance d'interpénétration des deux brosses sous pression à l'équilibre peut être

utilisée comme une échelle de longueur. Ceci nous permet de prédire la dépendance de la vitesse de cisaillement critique (qui sépare les réponses linéaire et non-linéaire) à la compression et aux paramètres moléculaires pour l'état stationnaire (cisaillement constant). Une forte corrélation entre les réponses microscopiques (extension latérale des chaines) et macroscopique de transport (viscosité du fluide) a été trouvée au delà de la réponse newtonienne. En agrément avec la description théorique développée, les simulations révèlent une loi de puissance simple qui lie ces phénomènes. De plus un bon agrément a été trouvé avec des expériences récentes réalisées par Schorr [*Macromolecules* **36**, 389 (2003)].

Au delà du régime stationnaire (équilibre ou cisaillement constant) le régime transitoire, qui part de l'état du système sous cisaillement constant et inverse le sens du cisaillement a été exploré. La présence du solvant explicite, qui ajoute au système un terme supplémentaire d'inertie, change dramatiquement la réponse du système comparé au cas avec solvant implicite. Tout ces cas, en terme de régime transitoire simple sont présents dans un dispositif expérimental, le régime oscillatoire. Une connexion entre tout ces cas a été établie et la limite d'accessibilité de ces régimes par le biais de simulation reproduisant le protocole ces expériences de rhéologiques a été discutée. Finalement ce document résumera et discutera les limitations de la théorie de champ moyen et revisitera l'étude de ces systèmes a l'équilibre statique. Une simple relation de Green-Kubo introduite par Bocquet et Barrat [*Phys. Rev. Lett.* **70**, 2726 (1993)] évalue les propriétés de friction à partir des fluctuations du système à l'équilibre au niveau de l'interface entre les brosses. Un comportement non-trivial des corrélations au temps longs au niveau de l'interface a été observé et devra faire l'objet d'étude complémentaire.

Contents

List of Figures

List of Tables

Chapter 1

Introduction

Figure 1.1: Egyptians pulling a Colossus, to aid the movement they use lubricant, domestiques carry vase of water to wetten the sand, El-Bersheh, circa 1800 B.C. [1]

In everyday life we are hardly aware of friction and how it is affecting us. In many examples friction is needed, e.g. walking, where the bare foot "pushes" with an angle on the floor, or rubber covered tires become bend due to contact with the surface. That general case represents static friction or stiction, where a threshold of parallel force is needed to overcome static adhesion. On the other hand, a force, called "kinetic friction force", is needed to move two interacting surfaces laterally with a given velocity. The research field of friction, lubrication and wear is called "tribology" [2].

In human history many examples are known where friction is reduced by changing the surface properties [3]. Figure 1.1 shows a wall painting where Egyptians wet the sand to transport stones or like in the painting large objects like a Colossus [4].

A first systematic study was done by Leonardo da Vinci and later rediscovered by

Amontons [4]. Their empirical finding connects the load L with the friction force F via the coefficient of friction

$$\mu = \frac{F}{L} \ .$$
(1.1)

The latter is independent of the contact area and the velocity, in a moderate regime of velocities [3]. This first observation approaches the problem of dry friction.

In order to reduce the friction force F a surface optimization can be applied, which may lead to an extremely small friction coefficient. This phenomenon is known as superlubricity. In such exotic situations, incommensurable contacts between layered crystals (i.e. graphite) slide past each other, with $\mu \sim 10^{-4}$ [5]. Such an optimization on the nanoscale seems to be challenging when it is applied to mesoscopic or macroscopic surfaces, although it may work on nanostructures. Furthermore, the presence of contaminants, i.e. absorbed molecules, and the assumption of almost infinite rigidity of asperities on such surfaces appears to be more theoretical and may not be the first choice for a reduction of friction.

A prerequisite for industrial revolution was the usage of lubricants, which helps to reduce the energy consumption and increases the lifetime of machines by minimizing the wear. The surface is covered with organic or inorganic loose matter, e.g. long-chain carbohydrates like oils or wax, water, molybdenum sulfate or nanotubes, minimizing the contact area [6]. One common example for hydrodynamic lubrication is the effect of aqua planning when a car is driven at high speed on a wet surface, and the tires are losing traction separating the wheels from the road. The friction force is determined by the viscous friction of the lubricant. Sliding on ice is similar. The ice creates a small layer of water between the surfaces resulting in a weak friction, $\mu \sim 10^{-2}$ [2]. When the lubricant is based on polymeric liquids the term "elastohydrodynamic lubrication" suits the same physical argument.

Under excessive loads and low sliding velocities the lubricating film is squeezed out of the gap and elasto-/hydrodynamic lubrication breaks down. If the lubricant is completely removed, dry friction will set in, which would imply high friction and wear. If a thin film remains absorbed, friction between surfaces is strongly reduced to dry friction. This is called boundary lubrication. One effect of boundary lubrication is the reduction of adhesion between solids dominated by van der Waals forces, F_{vdW}. These forces add to the effective load, yielding

$$F = \mu \left(L + F_{\mathrm{vdW}} \right)$$
(1.2)

for the friction force. The lubricant may reduce F_{vdW} leading to reduced load and therefore a reduced effective friction.

Nature is rich in many solutions minimizing friction, especially thin films of molecular thickness as they are studied in the context of nanotribology [2]. One example combines both varieties of boundary and hydrodynamic lubrication. Organic suitable solvent molecules wet an irregular array of macromolecular chains which are attached to a substrate, called "polymer brushes" [7]. Opposing brush-covered surfaces can carry very high normal loads, where simultaneously the resistance to lateral sliding motion may be orders of magnitude smaller than in dry friction [8, 9]. Polymer brushes have thus important applications as lubricants, e.g. in machine parts or artificial joints [10], and in biolubrication, e.g. synovial joints [11]. Experiments utilize the surface force apparatus (SFA) measuring in an oscillatory manner the fluids response. In Figure 1.2 such data taken from Ref. [9] are shown. Both normal and shear forces are measured as a function of compression. The smallest friction coefficient μ [Eq. 1.1] found is in the order 10^{-4}. While the extremely low friction forces are well established experimentally, the understanding of the underlying mechanisms are rather poor.

Tethered polymer chains gained attention in the 1950s preventing flocculation of colloidal particles [12]. Some of the first quantitative treatments to understand single polymer brushes on flat surfaces were done by Alexander [13], de Gennes [14], and Semenov [15]. At high surface coverage one may find that endgrafted chains strongly stretch and that this strong stretching implies that fluctuations around the "classical" path are negligible [16]. Milner *et. al.* [17] and Zhulina *et. al.* [18] independently implemented the idea of the strong stretching limit, which means that the brush height is much larger than the unperturbed extension of the single chain. Contrary to Alexander and de Genne not a step-like density brush profile but a parabolic profile (MWC profile) was found [17]. Many theoretical approaches to the problem of solvent flow past an endgrafted polymer layer employ the Brinkman equation [19], where the brush is interpreted as a porous medium. A qualitative agreement with the experiment of compressed brushes [20] was found by Frederickson and Pincus [21]. Another approach via self consistent field calculations of the monomer density and the solvent velocity profiles was presented by Harden, Cates, and Aubouy [22]. All studies used a step-like brush profile, the Alexander brush [14], forecasting a shear induced swelling of the brush. Contrary to the swelling Ra-

4
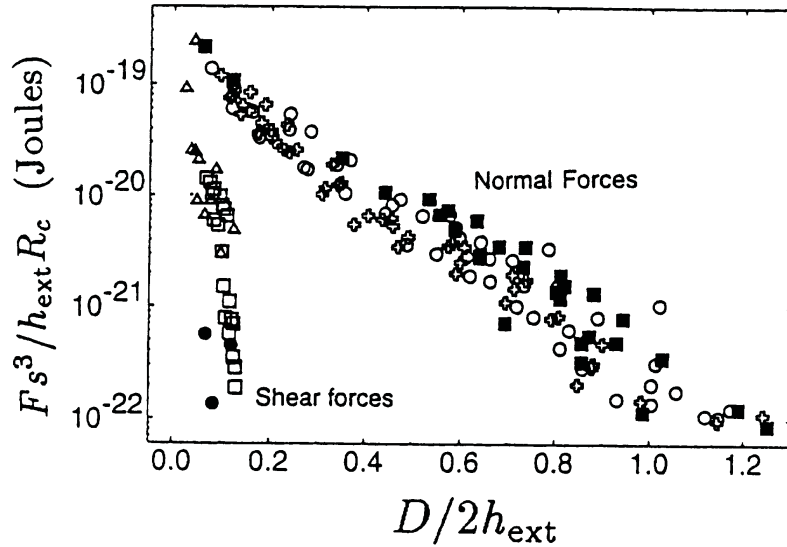
Figure 1.2: Shear and normal forces F between two sliding compressed polymer brushes in a good solvent. The force and the surface separation D are rescaled for a wide range of molecular weights, surface densities (s^{-2}), and unperturbed (single) brush heights (h_{ext}). For the case of lowest friction, a kinetic friction coefficient (eq. 1.1) $\mu \sim 10^{-4}$ is measured. (R_c is the curvature of the substrates). Taken from Ref. [9].

bin and Alexander [23] predicted an unperturbed brush height. On the other hand, Milner showed that the hydrodynamic interpenetration into a brush with parabolic density profile is larger than in a step-like brush [24]. Another study by Joanny [25] discusses two opposing sheared molten polymer layers, where chains disinterpenetrate at a finite critical relative velocity and no longer sustain the viscous stress.

Due to experimental difficulties, experiments do not provide sufficiently detailed information about the molecular factors causing the rheological response to external stimuli. Computer simulations can be employed as a "high resolution microscope". They work with idealized models controlling effects of contamination, surface roughness, polydispersity of the chains, and hydrodynamic correlations inside the complex fluids explaining the large activity in this field.

Several studies utilized self-consistent field solvers implementing hydrodynamics via the Brinkman equation for solvent- and monomer-flow field [26–31]. Solvent effects can also be treated implicitly via the Lattice-Boltzmann method [32] or stochastic rotational dynamics [33]. Several studies used molecular dynamics simulations (MD)

to simulate sheared polymer brushes without explicitly including solvent molecules implementing various thermostats and adjusting the interaction potentials between monomers, see for instance Refs. [34–42]. A small number of investigations were carried out with explicit solvent [36, 43–47]. The effects of explicit solvent are rarely studied by a direct comparison to implicit solvent implementations [43]. One of the main subject of this work, complementary to Ref. [43] is studying the effects of explicit solvent molecules. In this work, the nanotribological aspects of polymer brushes under shear using MD simulations of a classical coarse-grained model are studied. The considered systems consist of two opposing polymer brushes under good solvent condition. The degree of compression, density, and polymerization of the grafted chains are varied for systems with and without explicit solvent molecules. In chapter 2 the coarse-grained model, simulation parameters, and simulation details are presented. The third chapter contains the equilibrium properties of two opposing brushes analyzing the influence of solvent molecules on the density profiles. In the sliding regime most of the energy dissipation takes place in the overlap of the brushes. To quantify the interfacial zone a well established mean field model for a single polymer brush is introduced and conveyed to the problem of a compressed brush bilayer using a scaling theory approach. This theory is tested with simulation data.

The fourth chapter will carry on with the discussion of the stationary regime, where the two brushes are sliding with a constant velocity. The scaling theory will be extended to the non-linear response regime. It is supported by the numerical observations. Additionally the velocity profiles of brushes and solvent will be discussed.

Chapter 5 will look at the transient regime. First, the equilibrium brushes are set into motion reaching steady shear regime, and second the shear directions are inverted.

Chapter 6 will present the properties when remaining inside the transient oscillatory process. Usually, the SFA experiment is carried out such the steady state motion is one limit of the harmonic driving. A standardized rheological analysis will be performed connecting all the other regimes.

Chapter 7 discusses the fluctuations inside a brush bilayer and the occurrence of nontrivial long time correlations, which give rise for further theoretical considerations.

The thesis will finish with a summary.

6

Chapter 2

Model

Several methods are available to simulate polymeric systems out-of-equilibrium. In our case, we are interested in physical properties which involve several polymer chains, with thousands of atoms. The method of choice is to neglected the fastest degrees of freedom, like electron movements, and to coarse-grain the chains without extending the coarse-graining to a continuous description of the fluid. To retain enough details of the fluid we adopt a method that allows us to keep track of the behavior of the chains themselves. Many methods are available approximating hydrodynamic properties to a certain extent, like Lattice-Boltzmann simulation [32] and Brownian dynamics simulation with hydrodynamics [48, 49]. A standard simulation model is introduced, utilizing a bead-spring model for polymers and integrating the equation of motion by the Velocity-Verlet algorithm. In order to maintain hydrodynamic correlations of the fluid the internal degrees of freedom are coupled to a special thermostat that provides momentum conservation and Galilean invariance.

2.1   Simulation model

We performed molecular dynamics (MD) simulations of the Kremer-Grest Model (KGM) [50], a so-called bead-spring model, where monomers are represented by Lennard-Jones (LJ) particles coarse graining 3-5 hydrocarbon groups to one effective monomer. The monomer-monomer interaction is given by the shifted LJ-potential and is truncated at a cut-off radius $r_{\mathrm{c}} = \sqrt[6]{2}\sigma = r_{\mathrm{min}}$,

$$U_{\mathrm{LJ}}(r) = 4\epsilon \left[\left(\frac{\sigma}{r}\right)^{12} - \left(\frac{\sigma}{r}\right)^{6} - \left(\frac{\sigma}{r_{\mathrm{c}}}\right)^{12} + \left(\frac{\sigma}{r_{\mathrm{c}}}\right)^{6} \right] \quad \text{for } r \leq r_{\mathrm{c}}, \qquad (2.1)$$
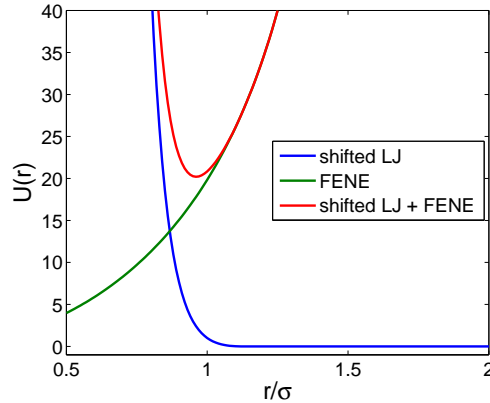
Figure 2.1: The shifted and truncated Lennard-Jones potential $U_{\mathrm{LJ}}(r)$ [Eq. 2.1], the FENE-potetnial $U_{\mathrm{FENE}}(r)$ [Eq. 2.2] and the sum of both are shown.

where ϵ and σ define the units of energy and length, respectively. Both are set to 1. The distance between two particles is denoted by r. In order to bind one end of the chain to the wall the LJ-potential is not shifted, but cut at $r_{\mathrm{c}} = 2.5\sigma$ and the depth of the potential well set to $\epsilon = 100$.

The connectivity between two adjacent monomers is given by the FENE (finitely extensible nonlinear elastic) potential of equilibrium distance $r_0 = 1.5\sigma$ and spring constant $k = 30\epsilon/\sigma^2$ [50],

$$U_{\mathrm{FENE}}(r) = -\frac{1}{2}kr_0^2 \ln\left[1 - (r/r_0)^2\right] \quad r \leq r_0. \tag{2.2}$$

The potentials are displayed in Figure 2.1.

In the following we will use LJ units. As mentioned, $\epsilon = 1$, $\sigma = 1$, and mass $m = 1$. The temperature is measured in units of ϵ/k_{B} (with the Boltzmann constant $k_{\mathrm{B}} = 1$), and the time is in units of $\tau = (m\sigma^2/\epsilon)^{1/2}$.

The solvent molecules are build up of two LJ particles connected via the FENE potential.

2.2 Molecular dynamics simulations

Classical molecular dynamics (MD) simulations [51] consists in solving Newton's equations of motion for a set of particles interacting via the coarse-grained model

potentials defined above. The coupled equation of motions need to be solved:

$$m_i \frac{d^2 \vec{r}_i}{dt^2} = \vec{F}_i \; , \tag{2.3}$$

where $\vec{r}_i$ and $\vec{F}_i$ are respectively the position of the ith monomer and the force exerted on it. The force $\vec{F}_i$ derives from the potentials describing the interactions

$$\vec{F}_i = -\frac{\partial U_{\text{pot}}(r_1, ..., r_N)}{\partial r_i} \; . \tag{2.4}$$

Under the assumption that the potential is dominated by the pairwise interactions, one can imply:

$$U_{\text{pot}} = \sum_{i \neq j}^{N} U_{\text{LJ}}(r_{ij}), \quad r_{ij} = |\vec{r}_i - \vec{r}_j| \; , \tag{2.5}$$

where the particle i interacts with particle j. By using a MD simulation scheme, the positions and velocities of all particles inside the system are calculated for the overall simulation time, allowing from there on to compute all physical properties. If the ergodic principle holds, the time-averaged quantities correspond to an ensemble average [51].

2.2.1 Dissipative particle dynamics (DPD) thermostat

The simulations are performed in an ensemble in which the particle number, the temperature, and the wall separation are held constant. The following section explains the usage of the DPD thermostat as a stochastic thermostat in MD simulations [52]. We do not perform dissipative particle dynamics in its original version. The DPD thermostat controls the temperature, as the Langevin thermostat [53], by counter-balancing a friction force removing instantaneously extra heat and a stochastic force pumping energy into the system. These two forces are connected via the fluctuation-dissipation theorem. Contrary to a Langevin thermostat, the DPD thermostat conserves local momentum by fulfilling Newton's third law. Such a conservation of momentum will treat problems with fluxes and thus hydrodynamics more accurately [54].

The equations of motion [Eq. (2.3)] include now the thermostat by

$$\dot{\vec{r}}_i = \frac{\vec{p}_i}{m_i} \; , \tag{2.6}$$

$$\dot{\vec{p}}_i = \vec{F}_i + \vec{F}_i^{\text{D}} + \vec{F}_i^{\text{R}} \; , \tag{2.7}$$

where $\vec{F}_i^{\mathrm{D}}$ is the damping force and $\vec{F}_i^{\mathrm{R}}$ is the random force, acting on particle i. The DPD forces are now given by the pairwise inter-particle forces:

$$\vec{F}_i^{\mathrm{D}} = \sum_{j\neq i} \vec{F}_{ij}^{\mathrm{D}} , \quad \vec{F}_i^{\mathrm{R}} = \sum_{j\neq i} \vec{F}_{ij}^{\mathrm{R}} . \tag{2.8}$$

The two forces are acting along the inter atomic axis $\vec{r}_{ij} = \vec{r}_i - \vec{r}_j$. Hydrodynamic correlations are maintained when damping the velocity differences in the DPD description. Following Warren *et al.* [54] the damping force is defined as

$$\vec{F}_i^{\mathrm{D}} = -\gamma_{\mathrm{DPD}} \sum_{j\neq i} \omega^{\mathrm{D}}(r_{ij})(\hat{r}_{ij} \cdot \vec{v}_{ij})\hat{r}_{ij} , \tag{2.9}$$

where $\gamma_{\mathrm{DPD}} = 5\tau_{\mathrm{LJ}}^{-1}$ defines a local friction constant, $\vec{v}_{ij} = \vec{v}_i - \vec{v}_j$ is the relative velocity of particles i and j, and the unit vector along the atomic axis $\hat{r}_{ij} = \vec{r}_{ij}/|\vec{r}_{ij}|$. The corresponding stochastic force is given by

$$\vec{F}_i^{\mathrm{R}} = \lambda \sum_{j\neq i} \omega^{\mathrm{R}}(r_{ij})\theta_{ij}\hat{r}_{ij} , \tag{2.10}$$

with λ being the strength of the noise and θ_{ij} is a Gaussian random variable defined by the first two moments

$$\langle \theta_{ij}(t) \rangle = 0 \tag{2.11}$$

$$\langle \theta_{ij}(t) \theta_{kl}(t') \rangle = (\delta_{ik}\delta_{jl} + \delta_{il}\delta_{jk}) \delta(t - t') . \tag{2.12}$$

It is pointed out that the DPD thermostat is neither acting between wall particles nor on wall-fluid interactions.

The fluctuation-dissipation theorem connects the strength of thermal fluctuations with the damping rate

$$\lambda^2 = 2k_{\mathrm{B}}T\gamma_{\mathrm{DPD}} , \tag{2.13}$$

and their corresponding weight functions

$$\left[\omega^{\mathrm{R}}\right]^2 = \omega^{\mathrm{D}} . \tag{2.14}$$

The functional form of ω^{D} can be chosen arbitrarily. Following [54] we chose for all the simulations

$$\omega^{\mathrm{D}}(r_{ij}) = (1 - r_{ij})^2 , \quad r < r_{\mathrm{c}} \tag{2.15}$$

with the same cut-off radius as the one used for the Lennard-Jones potential. Other choices are possible.

2.2.2 Integration of the equation of motion

Since no analytical solution of Eq. (2.3) exists for many-particle systems, an integration method of the interacting particles is used to follow their trajectories. There are several algorithms available to do so. All algorithms rely on the Taylor expansion of the positions at time $t + \Delta t$, with $\Delta t = 2 \cdot 10^{-3} \tau_{\mathrm{LJ}}$ being a short time interval or time-step

$$\vec{r}_i(t + \Delta t) = \vec{r}_i(t) + \Delta t \vec{v}_i(t) + \frac{\vec{F}_i^{\mathrm{tot}}(t)(\Delta t)^2}{2m_i} + \mathcal{O}(\Delta t^3) \, , \tag{2.16}$$

where $\vec{v}_i(t)$ represents the velocity, $\vec{F}_i^{\mathrm{tot}} = \vec{F}_i + \vec{F}_i^{\mathrm{D}} + \vec{F}_i^{\mathrm{R}}$ the total force, $\vec{F}_i^{\mathrm{tot}}(t)/m_i$ the acceleration of the particle i at the time t, and $\mathcal{O}(\Delta t^3)$ higher order polynomials of the Taylor expansion. Using the equivalent expression for the first order derivative $\vec{r}_i(t - \Delta t)$ one arrives at the Verlet formulation of Eq. (2.3). It gives an extrapolated position of particle i in time based on known velocities $\vec{v}_i(t)$ and forces $\vec{F}_i(t)$.

Velocity-Verlet algorithm with DPD thermostat

The positions are updated using

$$\vec{r}_i(t + \Delta t) = \vec{r}_i(t) + \Delta t \vec{v}_i(t) + \frac{1}{2m_i} \vec{F}_i(t)(\Delta t)^2 \, . \tag{2.17}$$

Next the velocity for half a time step is evaluated

$$\vec{v}_i^*(t + \frac{\Delta t}{2}) = \vec{v}_i(t) + \frac{1}{2m_i} \Delta t \vec{F}_i(t) \, . \tag{2.18}$$

Since the forces now depend on the positions and additionally on the velocities the extrapolated force becomes

$$\vec{F}_i(t + \Delta t) = \vec{F}_i \left(\vec{r}_i(t + \Delta t), \vec{v}_i^*(t + \frac{\Delta t}{2}) \right) \, , \tag{2.19}$$

while the velocities for the next time step are obtained by

$$\vec{v}_i(t + \Delta t) = \vec{v}_i(t) + \frac{1}{2m_i} \Delta t \left[\vec{F}_i(t) + \vec{F}_i(t + \Delta t) \right] \, , \tag{2.20}$$

and the procedure begins again assembling the trajectories for all particles, see Ref. [55].

2.3 Simulation procedure

Initial configuration

At the beginning the setup procedure creates two walls at a certain distance $\hat{D}_z$ relatively to each other build up of monomers. Based on the vectors of the fcc lattice the LJ particles create an egg carton like surface impenetrable for other LJ particles. Along this highly symmetric surface one end-monomer out of each chain is positioned randomly in the xy-plane at a small distance from the wall. In order to ensure that no artificial high symmetric polymer brush configuration is created a random number generator sets up a random configuration [56]. Based on two positive random numbers $\eta(0,1) \leq 1$ drawn from a flat distribution, the end monomer is positioned in $x = \eta(0,1)L_x$ and $y = \eta(0,1)L_y$ on the walls. The extension of the substrates in x and y direction are set to $L_x = 41.66\sigma$ and $L_y = 36.1\sigma$. All N_g grafted end-monomers are bound with an interaction energy of $\epsilon = 100$ to the wall. From that starting point the backbone of each chain is created via a random walk placing the next monomer of that chain via 2 random numbers in x and y directions and the step in z-direction is fixed to ensure the stretching. The random step distances is 20% smaller then σ. In order to avoid that the particles initially are set too close to each other and overlap too strongly, the initial wall distance $\hat{D}_z$ is chosen more than twice the desired wall distance D'_z. The solvent molecules can now be placed into the system with a higher acceptance rate. When a stable configuration is setup the fluid is shortly equilibrated (for $100\tau_{\mathrm{LJ}}$) and both walls are moved together to the desired wall distance D'_z. Both wall movements are given by

$$\Delta z = v_z^{\mathrm{wall}}\Delta t \ , \tag{2.21}$$

where $v_z^{\mathrm{wall}} = 0.1$ is chosen. Since the wall particles are of size σ, we may define an effective wall distance by $D_z = D'_z - 2 \cdot 2^{1/6}\sigma$, which reflects the distance between the grafted planes, see Figure 3.1.

Equilibration

After the configuration has reached the desired wall distance D'_z the overall density reaches $\rho = 0.9$ if the system is filled with brush and solvent molecules. To incorporate the fluid more correctly the overall density is chosen rather high to come close to the (ideal) situation of incompressible fluids [57]. A system without

explicit solvent has naturally a smaller density $\rho = N \cdot N_\mathrm{g}/(D_z \cdot L_x \cdot L_y)$. To obtain a numerically stable system the particles must reach a self-assembled maximal distance to each other maintaining on average a constant energy. To accelerate the mixing processes the excluded volume is arbitrary chosen to be small at the beginning of the equilibration process. The cut-off radius in Eq. (2.1) increases with time until it reaches its maximum volume r_c. Usually, after $20000\Delta t$ the maximal volume is reached. Afterwards, an equilibration run for $3 \cdot 10^5 \Delta t$ with full interaction range is performed. A system is assumed to be in a stationary state when all observables in average do not change in time and several observables are symmetric, e.g. density or velocity profiles. In comparison to the study of Grest [36], where the same polymer model for polymer brushes under shear with dimer solvent was studied, included the simpler Langevin thermostat. In shear direction the Langevin noise and frictional terms were switched off. The Kremer-Grest-Model has been studied extensively for single end-grafted polymer chains [58] without explicit solvent.

Furthermore, the temperature along the gap is watched carefully to fulfill the thermodynamic boundary condition for the NVT ensemble. For two grafting densities with the shortest chain length $N = 30$ at a wall separation $D'_z = 14.275$ the temperature profiles for both components, polymer brush and explicit solvent are shown in Figure 2.2 at equilibrium. The tethered ends are bound in the minimum of the steep LJ-potential and are hence less mobile than the rest of the fluid. This leads to a shallow parabolic temperature profile. For the highest grafting density $\rho_\mathrm{g} = 4.4\rho_\mathrm{g}^*$ a reduction of about 2.5% of the desired temperature T_0 is measured. For lower grafting densities the cooling effect is reduced. When the systems are driven into a constant shear regime a slight temperature increase is observed. For the highest wall velocity the temperature profile for each component grows by about 4%.

Wall shear protocol

Referring back to the experimental geometry a simple shear flow will be induced into the fluid by translating the lattice sites associated with wall atoms in the top and bottom walls in opposite directions by a distance Δx [59]. The magnitude of the displacement is determined by the applied shear rate

$$\dot{\gamma} = \frac{2v_x^\mathrm{wall}}{D_z} \, , \tag{2.22}$$

14
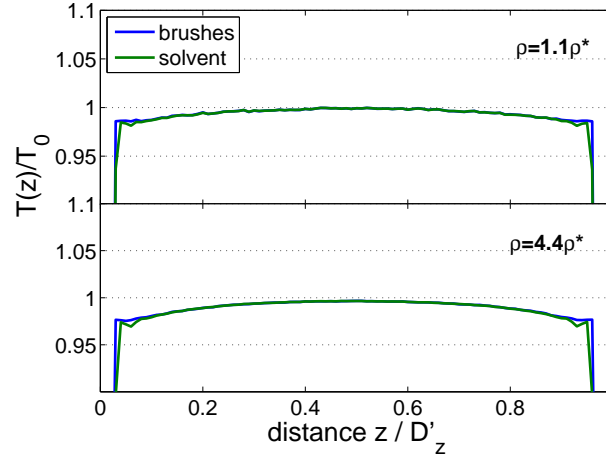
Figure 2.2: The layer-resolved temperatures of both components, brushes (blue line) and solvent molecules (green line) create parabolic shaped profiles, where in the middle the temperature is at the imprinted temperature T_0. Toward the walls the temperature drops symmetrically, with the highest grafting density the largest cooling of about 2.5% is observed. In the legend ρ denotes the grafting density, which is, e.g. 4.4 above the overlap density $\rho*$.
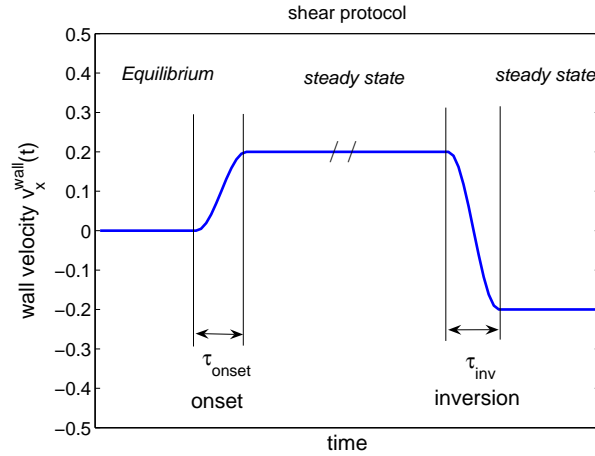
Figure 2.3: An example of a wall velocity v_x^{wall} in time. An equilibrated configuration is driven with a short onset of motion to a steady state. When the observables reached steady state, the system is observed separately (indicated by two slashes). The inversion is performed by changing rapidly the direction $v_x^{\mathrm{wall}} \rightarrow -v_x^{\mathrm{wall}}$. Both transitions times τ_{onset} and τ_{inv} are chosen to be small.

and given by

$$\Delta x = \pm 2\dot{\gamma} D_z \Delta t \ . \tag{2.23}$$

The pre-factor 2 in Eqs. (2.22) and (2.23) includes the driving of both walls, which doubles the relative motion.

Figure 2.3 shows a schematic sketch of the wall protocols (except the oscillatory motion), which we have implemented. Several regimes, two stationaries and a non-stationary regime, are shown, where the equilibrium and the steady state represent the stationary ones. The transition protocol for the onset of motion, given by

$$v_x^{\text{wall}}(t) = v_0 \left[1 - \cos\left(\frac{2\pi(t - t_0)}{\tau_{\text{onset}}} \right) \right] \ , \tag{2.24}$$

applied for a half of a complete cycle, where v_0 denotes the steady state velocity, t_0 the starting point of the transition, and τ_{onset} the transition time. Similar to the onset of motion a smooth function for the inversion $v_x^{\text{wall}} = -v_x^{\text{wall}}$ is implemented

$$v_x^{\text{wall}}(t) = v_0 \cos\left(\frac{2\pi(t - t_0)}{\tau_{\text{inv}}} \right) \ , \tag{2.25}$$

where τ_{inv} denotes the inversion time for the wall, and the transition is carried out for a half of a cycle. When both times are set to zero the velocities change in a step-like manner. Such a delta-function type of excitation induces a wide range frequencies into the flow. The induced responses must die out first before the flow can be examined. On the other hand, in an SFA experiment the transition works with finite acceleration, like in Ref. [9]. In the other limit, when the transition times become very large the brushes have time to relax during the transition. In order to observe a transition as in the experiment $\tau_{\text{onset}} \ll \tau_{\text{bilayer}}$ and $\tau_{\text{inv}} \ll \tau_{\text{bilayer}}$ are chosen to be much smaller than the relaxation time of the brush bilayer τ_{bilayer}. In chapter 5 this relaxation time is determined.

To ensure that the fluid remains at constant temperature, the second central moment of the particle's velocity is carefully observed. The local heat transfer rate $\gamma_{\text{DPD}} = 5\tau_{\text{LJ}}^{-1}$ is chosen not too large in order to avoid overdamping of local movements. In the study of Goujon *et. al.* [44] a higher rate was chosen, $\gamma_{\text{DPD}} = 12\tau_{\text{LJ}}^{-1}$ satisfying the thermodynamic boundary in the grand canonical ensemble at much higher shear rates. When the walls are moving kinetic energy must be dissipated in the fluid to maintain a constant temperature. The thermostat acts locally whenever two particles collide, however the heat transfer rate is instantaneously removing the

extra heat. At a extremely large velocities the heat production rate dominates over the dissipative rate and the fluid heats up. For the implemented algorithm and local friction term the maximum wall velocity is set to $v_x^{\text{wall}} = 0.23\sigma/\tau_{\text{LJ}}$, where the temperature between the walls increases up to 4% compared to the externally set temperature $T_0 = 1.68 m\sigma^2/\tau_{\text{LJ}}^2$. Another limit for the maximum wall velocities is given by the speed of sound of the fluid. For both solvent and solvent-free cases the speed of sound is measured, $v_{\text{sound}} \approx 4\sigma/\tau_{\text{LJ}}$.

The elements of the stress tensor σ_{ij}, with $i, j = 1 \ldots 3$ being the three independent spatial directions, is calculated via the Irving-Kirkwood implementation [60]. In the stationary regimes all components of the stress tensor along the gap must remain constant due to mechanical stability and constant in time. A second control for mechanical stability is given by the forces acting onto the walls, e.g. shear force f_x and normal force f_z, which are up to the geometric prefactor equal to the corresponding stress tensor components $(\sigma_{xz}, \sigma_{zz})$.

Chapter 3

Two opposing brushes at equilibrium
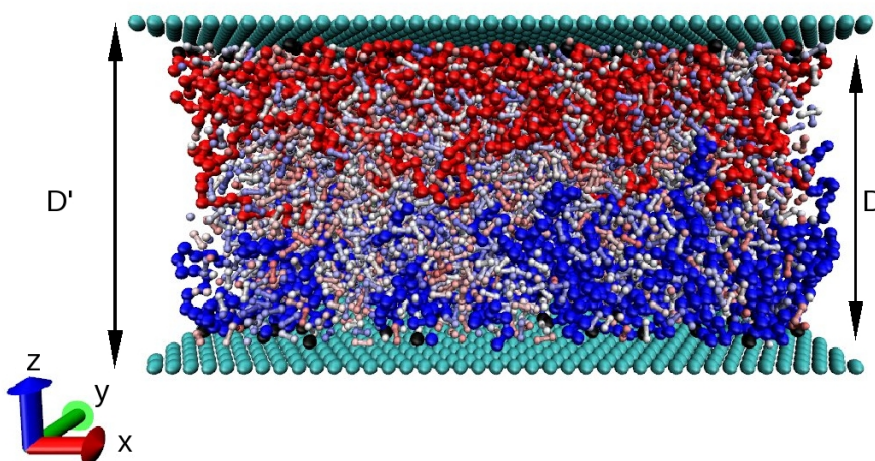
Figure 3.1: Typical snapshot of two polymer brushes at static equilibrium. The distance between the surfaces (light blue spheres) is $D'_z = 19.75$, corresponding to a distance between grafting planes of $D_z = 17.5$. Each brush consists of chains with $N = 30$ monomers per chain. The grafting density is approximately twice the critical grafting density, at which the chains overlap. Red and dark blue spheres represent monomers, and white spheres are solvent molecules. Their size has been scaled down for clarity.

In the last few decades much effort was made to investigate the behavior of two opposing surfaces covered with polymers. Here, the theory of Milner, Witten, and Cates [17] for a single brush and two compressed brushes in static equilibrium will be revisited. A description for the interface width between the two layers will be given and compared with simulations.

3.1 Single polymer brush: MWC-Theory
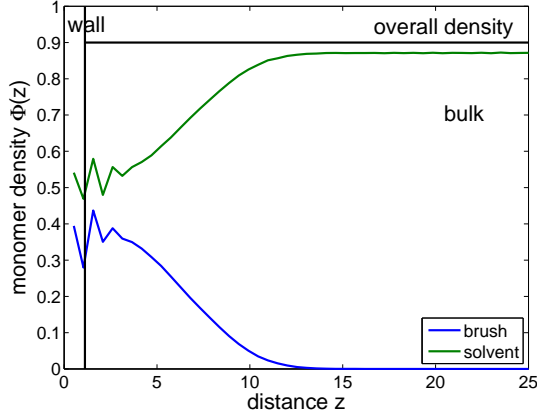
Figure 3.2: Single brush profile stretching into good solvent reservoir.
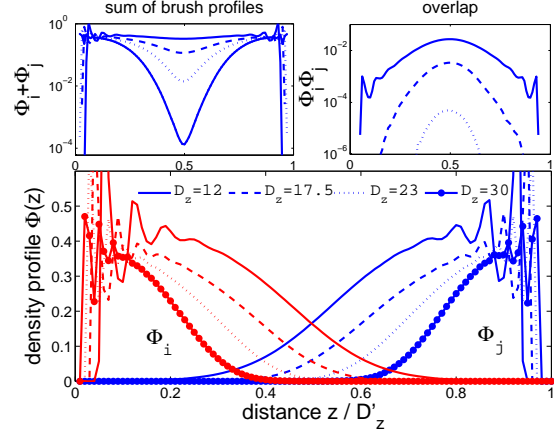
Figure 3.3: A bilayer density profile at different wall separations. The upper left plot shows the sum of both profiles and the right one shows the overlap at different compressions.

A grafted polymer layer can be obtained by using a functionalized end group that adsorbs onto a substrate. The grafting density is defined by

$$\rho_{\mathrm{g}} = \frac{N_{\mathrm{g}}}{A} \; , \tag{3.1}$$

with the number of absorbed end monomers N_{g} and the surface area A. If the density ρ_{g} is lower than a crossover value ρ_{g}^*, the critical grafting density, the chains will not interdigitate. The cross-over value ρ_{g}^* follows from the chain extension, e.g. the radius of gyration

$$R_{\mathrm{g}}^2 = \frac{1}{N} \sum_i \left(\vec{r}_i - \vec{r}_{\mathrm{cm}} \right)^2 \; , \tag{3.2}$$

quantifying the extension of one chain (with N monomers) by the relative position of each monomer $\vec{r}_i$ to the chain's center of mass position $\vec{r}_{\mathrm{cm}}$ [61]. The critical grafting density is defined by

$$\rho_{\mathrm{g}}^* = 1/\pi R_{\mathrm{g}}^2 \; , \tag{3.3}$$

with R_{g}^2 taken for an isolated chain in solution. The regime of lower grafting densities is referred to as the "mushroom" regime [7]. Larger grafting densities lead to a semi-dilute regime where a polymer brush [13, 14] is formed.
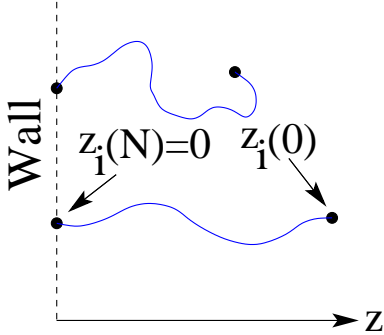
Figure 3.4: A sketch of endgrafted chains consisting of N monomers.
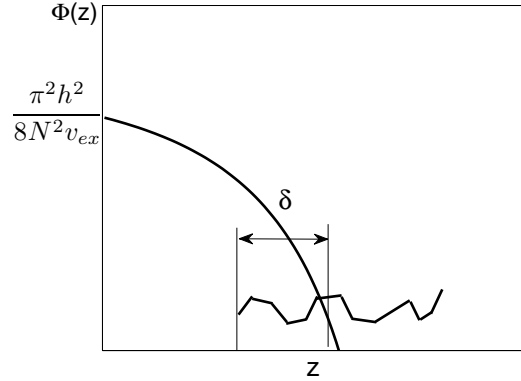
Figure 3.5: Density profile of MWC-brush penetrated by a segment of a single chain by a length δ.

In the simulation we observe that the chains start to stretch away from the surface to counterbalance the monomer-monomer repulsive interaction and the entropic elastic energy of the chains creating a parabolic density profile with an exponential tail at the free end [58]. Figure 3.2 shows the monomer density profile of a single brush stretching perpendicular from the surface reaching into the bulk of solvent molecules. For clarity the critical grafting density always referrers to the shortest chains ($N = 30$) simulated, e.g. $\rho_g = 1.1\rho_g^*$ where ρ_g^* is defined by Eq. (3.3). When the chain length is doubled, e.g. $N = 60$, the number of endgrafted chains is mottled keeping the brush monomer density constant and the critical density is referred to the one of the shortest chains, $N = 30$. When any theoretical expressions depending on chain lengths and grafting densities are shown, the legend will display the grafting densities in a simplified manner, ρ^* and not ρ_g^*. While systems with explicit solvent molecules are symbolized by filled symbols, systems without dimeres are shown with open symbols. The different wall distances are color-coded.

3.1.1 Milner-Witten-Cates brush

The single chains are attached by one end while the other end is freely reaching into the bulk. The monomers of the chain create a sequence of steps $z_i(N)$ (with i chains, $i = 1, \ldots, N_g$) along the chain's contour. Figure 3.4 shows the idea that a single chain conformation corresponds to a classical path of a particle in a potential $U(z)$. Following Ref. [17] the monomer positions represent a path starting at $z_i(0)$

and reaching in N monomers or "time" steps the grafted end point $z_i(N)$. At mechanical equilibrium the tension at the chain end becomes zero (for $N \to \infty$),

$$\frac{dz}{dn}(z_i(0), 0) = 0 \tag{3.4}$$

leading to a zero initial "velocity", when the monomer index n is identified as the time.

For each particle to reach the wall it takes N fixed steps or a fixed time, which is independent of the starting point. The simplest equal-time potential is given by a harmonic oscillator,

$$U(z) = Bz^2 - A . \tag{3.5}$$

The mean field assumption connects now the potential linearly with the density profile via the excluded volume parameter v_{ex},

$$\Phi(z) = -U(z)/v_{\mathrm{ex}} . \tag{3.6}$$

The constants A and B can now be calculated. The total number of monomers give

$$N\rho_{\mathrm{g}} = \int_0^h \Phi(z)dz . \tag{3.7}$$

With Eq. (3.5) and (3.6) we obtain

$$A = v_{\mathrm{ex}}\frac{N\rho_g}{h} + \frac{Bh^2}{3} , \tag{3.8}$$

where h represents the mean brush height. When the spring constant $2B$ is interpreted as an angular frequency $\sqrt[2]{2B} = 2\pi/T$ and the path of the particle corresponds to a quarter of the cycle $T = 4N$, one gets

$$B = \frac{\pi^2}{8N^2} . \tag{3.9}$$

The density becomes

$$\Phi(z) = \frac{\pi^2}{8N^2 v_{\mathrm{ex}}}(h^2 - z^2) . \tag{3.10}$$

3.2 Compressed brush bilayer

We may distinguish three regimes for the compressed bilayer. First, for the wall separations $D_z \gg 2h$ the brushes do not overlap and most of the liquid flows in the polymer free region, see Figure 3.2. When the system is now externally driven, hydrodynamic lubrication will dominate the system's properties. On the other hand, as already mention in Chapter 1 the system would not be stable under high loads extorting the solvent. Increasing the load compresses the bilayer until the separation becomes of the order of twice the free brush height $D_z \simeq 2h$, the brushes start to interpenetrate each other weakly because both profiles are just touching at the outer fringe. At high compression, when $D_z \ll 2h$ the profiles overlap strongly, see Figure 3.3. A third compression regime is given when the compression becomes of the order of the monomer size, $D_z \sim \mathcal{O}(a)$, strong oscillations occur in the density profile. The system is so strongly compressed that a highly symmetric ordering along the gap takes place, the liquid solidifies. For further discussion we stay in the regime of strong compression where $a \ll D_z \ll 2h$, both brushes strongly interpenetrate, and they create a uniform monomer profile

$$\Phi = \frac{N\rho_{\mathrm{g}}}{D_z}. \tag{3.11}$$

In the case of strong interpenetration both brushes overlap significantly and chains from one brush enter the other one. Figure 3.3 shows the density profiles of two brushes at different wall distances. The brushes from opposite surfaces start to interpenetrate at $D_z \approx 25$, where a small overlap is found. The interpenetration can quantified by the expression [37, 62]

$$I_{\mathrm{ov}} \sim \int_0^{D_{\mathrm{z}}} \Phi_1(z)\Phi_2(z)dz, \tag{3.12}$$

where $\Phi_j(z)$ represents the density profiles of brush $j(=1,2)$. The upper right plot in Figure 3.3 shows the overlap $\Phi_1(z)\Phi_2(z)$ for different wall distances. All overlap densities have a similar shape with a maximum at $D_z/2$. The sum of both monomer concentration profiles $\Phi_1(z) + \Phi_2(z)$ is shown in the upper left plot of Figure 3.3. The further the brushes are pressed into each other the more uniform the overall density becomes. For $N = 30$, $\rho_{\mathrm{g}} = 2.2\rho_{\mathrm{g}}^*$, and smallest simulated wall distance $D_z = 12$, shown in Figure 3.3, the monomer density becomes uniform along the gap and is defined as the strong compression regime.

We now want to calculate the width of the interfacial region. The overlap thickness can be derived from the work ΔF required to displace a segment of a chain by δ [63]

$$\frac{\Delta F}{k_{\mathrm{B}}T} \sim \left(-\frac{\delta^3}{a^2}\frac{\partial U(z)}{\partial z}\right)^{1/2} , \tag{3.13}$$

where the potential $U(z)$ may be of the classical parabolic form [Eq. 3.10]

$$U(z) = U_0 - \frac{1}{2}\left(\frac{\pi z}{2Na}\right)^2 , \tag{3.14}$$

with constant U_0 and a being the effective monomer size.

When the derivative of Eq. (3.13) at $z = h$ is taken, one finds

$$\frac{\Delta F}{k_{\mathrm{B}}T} \sim \left(\frac{\delta^3\pi^2}{8N^2a^4}h\right)^{1/2} . \tag{3.15}$$

The height of a brush in a strongly compressed bilayer is half the gap size, i.e. $h = D_z/2$, thus leads to

$$\frac{\Delta F}{k_{\mathrm{B}}T} \sim \left(\frac{\delta^3}{a^2}\frac{\pi^2}{N^2a^2}D_z\right)^{1/2} . \tag{3.16}$$

Assuming the overlap occurs due to thermal fluctuations, e.g. $\Delta F \sim k_{\mathrm{B}}T$, one gets for the interpenetration length of the *molten* brush bilayer

$$\delta_{\mathrm{melt}} \sim \left(\frac{N^2a^4}{D_z}\right)^{\frac{1}{3}} . \tag{3.17}$$

Apart from the melt condition, generally two regimes, depending on the concentration of the polymers, can be considered. In a good solvent condition a single polymer chain interacts only with itself. When the concentration increases the "coils" start to interact with each other, intermolecular contributions increase while intramolecular interactions are partially screened by the surrounding chains. The brush can then be regarded as dense melt of concentration blobs. The screening length ("blob" size), above which all excluded volume interactions are screened, depends on the density as [64]

$$\xi_{\mathrm{c}} \sim a\left(a^3\Phi\right)^{-\frac{\nu}{3\nu-1}} , \tag{3.18}$$

where $\nu = 0.588$ is the Flory exponent. We now rescale the effective monomer size by

$$a \to \xi_{\mathrm{c}} , \tag{3.19}$$

with the blob size or correlation length ξ_c. The number of monomers is rescaled via

$$N \rightarrow N/g_c \,, \tag{3.20}$$

where $g_c \sim (\xi_c/a)^{1/\nu}$ is the number of monomers inside a blob. The interface width δ_{semi} in the semi-dilute regime is given by transforming δ_{melt}, Eq. (3.17), with Eq. (3.19), (3.20), (3.18), and the uniform density concentration into

$$\delta_{\text{semi}} \sim a \left[N^{2\nu} \left(\rho_g a^2 \right)^{2(1-2\nu)} \left(\frac{a}{D_z} \right)^{1-\nu} \right]^{\frac{1}{3(3\nu-1)}} . \tag{3.21}$$

Another quantity will be used in the further discussion, the lateral extension of the chains, which in a melt follows Gaussian statistics,

$$R_{\text{g},x}(0) \sim a \ N^{1/2} . \tag{3.22}$$

After renormalization into blobs, one finds

$$R_{\text{g},x}(0) \sim a \left[N^\nu \left(\frac{D_z}{\rho_g a^3} \right)^{2\nu-1} \right]^{\frac{1}{2(3\nu-1)}} . \tag{3.23}$$

Figure 3.6 compares the measured overlap width δ of two brushes with Eq. (3.21). As long as both brushes are interpenetrating their interfacial width is estimated by the variance of a Gaussian fit of the overlap function $\Phi_1\Phi_2$. For large wall separation and low polymer density ($N = 30$, $\rho_g = 1.1\rho_g^*$) the blob size ξ_c grows towards the outer fringe of the brushes [65] and the theory breaks down, as can be seen from the lower data points in Figure 3.6. For long chains ($N = 120$) the overlap is dominated by density oscillations where the Gaussian fit underestimates the actual width, see upper data set in Figure 3.6. The lateral extension of the chains is compared to Eq. (3.23), shown in Figure 3.7. In both plots a line is added as a guide to the eye indicating that the observables are in good agreement with the scaling approach. The effective monomer size is set to 1. In section 3.3.2 the lateral chain extension is used to estimate a.
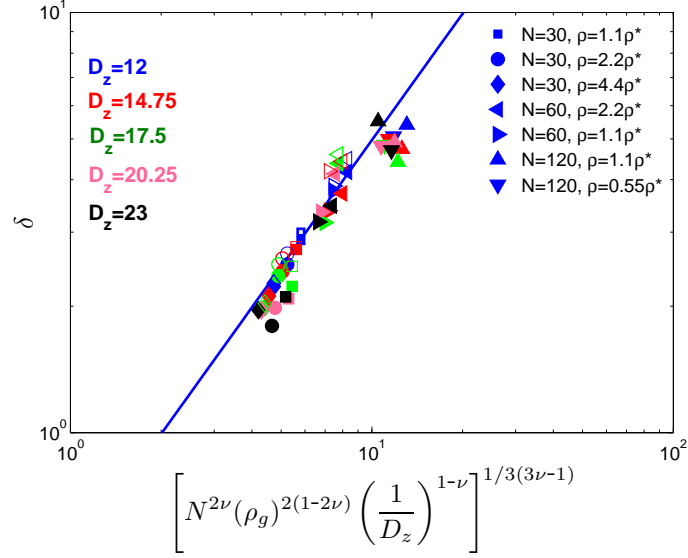
Figure 3.6: A log-log plot comparing the equilibrium interpenetration depth of all simulated systems.The filled symbols represent systems with explicit solvent while complementary systems with implicit solvent are shown with open symbols. The equilibrium overlap width δ is well described by Eq. (3.21).
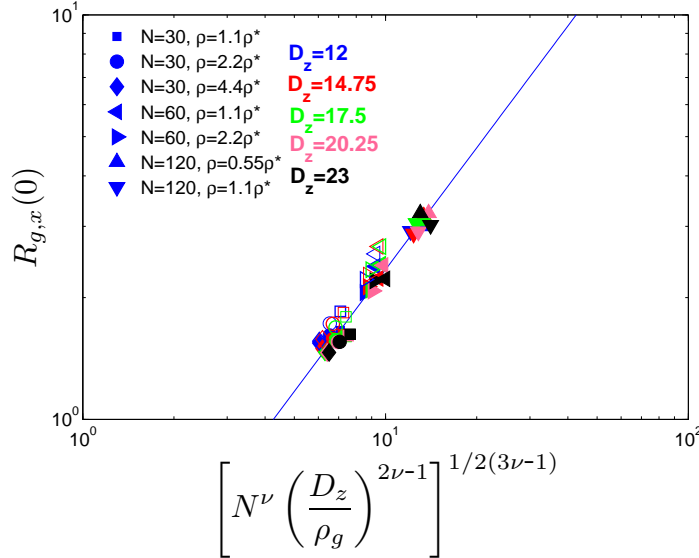
Figure 3.7: A double logarithmic plot comparing the lateral extension chains inside the compressed brush layer with Eq. (3.23). The color and symbol-coding follows Figure 3.6.

3.3 Other properties

3.3.1 Diffusion

Observables which are directly accessible in the numerical study are diffusion co-efficients of the chains and the solvent molecules. Since all molecules are constrained
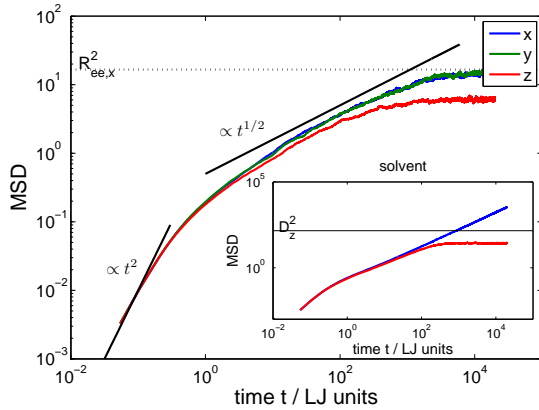
Figure 3.8: Evolution of the MSD of all monomers belonging to brushes in all 3 directions, starting in the ballistic regime, becoming subdiffusive and crossing over to a plateau that matches with a length scale of lateral the end-to-end vector. The inset shows the MSD of the solvent.
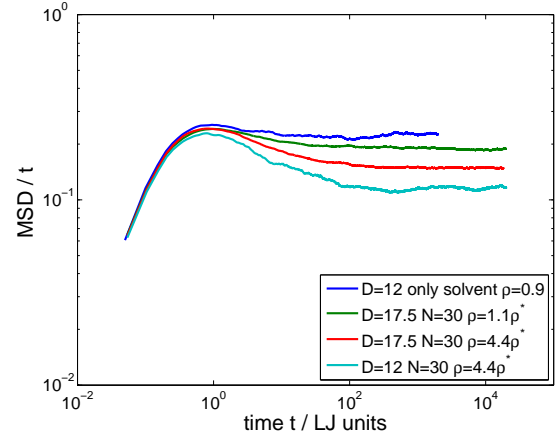
Figure 3.9: The MSD divided by time of all solvent molecules are shown, the plateau value is used to calculate D for different brush compositions.

inside a non-isotropic space, where the walls are breaking the symmetry of free diffusion in three dimensions, one expects at least for the solvent molecules in z-direction a saturation. For the brush monomers a stronger constraint applies and one expects the restriction in all three direction. The mean square displacement(MSD) is used to calculate the diffusion coefficient via

$$\langle (\vec{r}(t) - \vec{r}(0))^2 \rangle \overset{\lim}{\underset{t \to \infty}{=}} \frac{1}{6} Dt \; , \tag{3.24}$$

where $\vec{r}(0)$ is the starting point of a particle at time $t = 0$, $\vec{r}(t)$ its position at time t, and D being the diffusion coefficient. Figure 3.8 shows the diffusion of all monomers belonging to brushes starting from the ballistic regime $\sim t^2$, on intermediate times the MSD becomes subdiffusive $\sim t^{1/2}$, and in the limit of long times the monomers "feel" the constraint of being attached to the wall, the MSD becomes constant. The plateau value corresponds to a length scale of the brush, the squared end-to-end vector, given by

$$\vec{R}_{ee}^2 = \langle (\vec{r}_N - \vec{r}_1)^2 \rangle \; , \tag{3.25}$$

where $\langle \rangle$ denotes the average over all chains of the brushes.

A similar tracking of the trajectories can be done for the solvent molecules, which

can diffuse freely in x-, y-direction but are limited in z-direction, see inset Figure 3.8. The constant MSD in z-direction for the solvent does not reach the value for the geometric boundary, D_z^2, but saturates earlier. Following the arguments in Ref. [66], the perpendicular displacement cannot grow infinitely. In the long-time limit the probability of finding a particle inside the system of one type is given by its density distribution. When the brushes are strongly compressed the highest probability of finding a dimer is in the minimum of the brush-brush density. Towards the walls the solvent density decreases symmetrically, since brushes are occupying some volume and create a mesh in which the solvent has to diffuse through creating an effective boundary. When both densities become uniform in the strong compression regime the brushes must dominate the mobility of the solvent resulting in a smaller displacement.

Using the Stokes-Einstein relation [61] the solvent viscosity η_s can be found from

$$D = \frac{k_B T}{6\pi\eta_s r} \tag{3.26}$$

with r the radius of the spherical particle. The radius of gyration of the dimer, $r \approx 0.46$, is used. For the different compositions different diffusion coefficients are observed and therefore different solvent viscosities. The higher the compression and the denser the brushes become the slower the particles diffuse. In Figure 3.9 this effect is shown, where for the highest compression, $D_z = 12$, the highest grafting density $\rho_g = 4.4\rho_g^*$, and shortest chain length $N = 30$ the highest viscosity is observed. When now the wall separation grows more solvent molecules accumulate in between the brushes increasing the mobility of the solvent. Even changing the molecular parameters but keeping the brush monomer concentration constant, e.g. $\rho = 2.2\rho^*$ and $N = 60$, effects the mobility. For a test system without brushes the explicit solvent molecules move the fastest, see Figure 3.9, blue solid graph.

3.3.2 Effective monomer size

As the solvent viscosity also the effective monomer size a depends implicitly on the parameters N, ρ_g, and D_z. To estimate the effective monomer size a prefactor A is introduced such that

$$R_{g,x}(0) = Aa\left[N^\nu\left(\frac{D_z}{\rho_g a^3}\right)^{2\nu-1}\right]^{\frac{1}{2(3\nu-1)}} \tag{3.27}$$
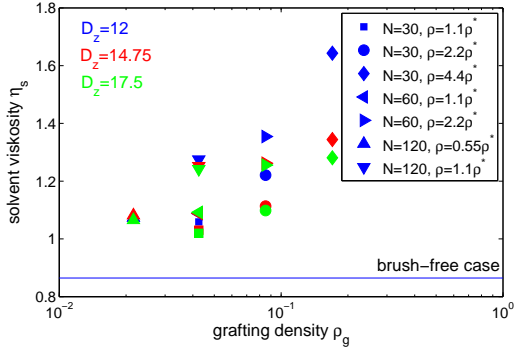
Figure 3.10: The solvent viscosity η_s for different compositions. The lower limit corresponds to the brush-free case.
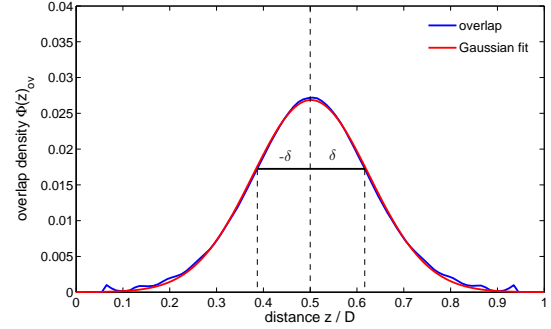
Figure 3.11: Overlap density $\Phi_{\mathrm{ov}}(z)$ with a Gaussian fit and width 2δ.

becomes equal to Eq. (3.23). When that prefactor A is determined its value is absorbed into a.

3.4 Summary

The problem of two polymer-brush bearing surfaces interdigitating at equilibrium was introduced. We started with a two single brushes which were so far apart that no interaction between them took place. The single brush is theoretically described by the mean field theory of Milner, Witten, and Cates [17]. As the brushes approach each other they start to penetrate each other by creating an interfacial zone. The overlap width was evaluated by applying the MWC-theory of molten brushes and transferred into the semi-dilute regime. Additionally, the lateral extension was rescaled in a similar fashion. Both equilibrium quantities were tested for the whole range of parameters sustaining the scaling approach. As long as the sum of the brush profiles is almost constant along the interpenetration region, the theory can be confirmed. For short chains and large wall separation, where the brushes just touch, the theory breaks down.

The relevant length scale δ_{semi} and the parallel chain extension $R_{\mathrm{g},x}(0)$ will be used in the next chapter for steady state sliding.

Chapter 4

Two opposing brushes in steady shear
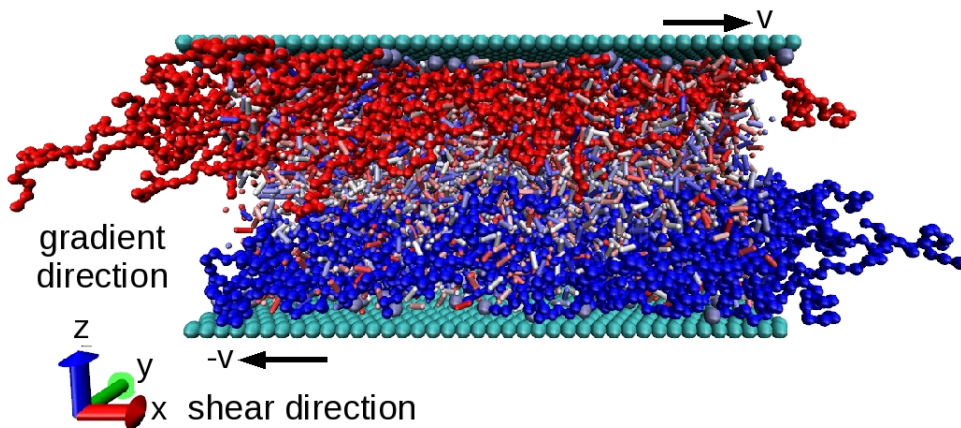
Figure 4.1: Snapshot of two polymer brushes with the same parameters as in Figure 3.1, but now at constant relative shear velocity. The shear rate, $\dot{\gamma} \equiv 2v_0/D_z$, corresponds to a Weissenberg number of $Wi \approx 13.5$, i.e. the system is well beyond linear response.

In this chapter the results of two opposing polymer brushes in steady Couette flows are presented, which is applied by shearing the substrates with a constant relative velocity of $2v_0$ at a fix wall distance D_z.
First, phenomenological observations of rheological responses are used explaining the responses of the complex fluid. Furthermore, an analytical concept is intro-
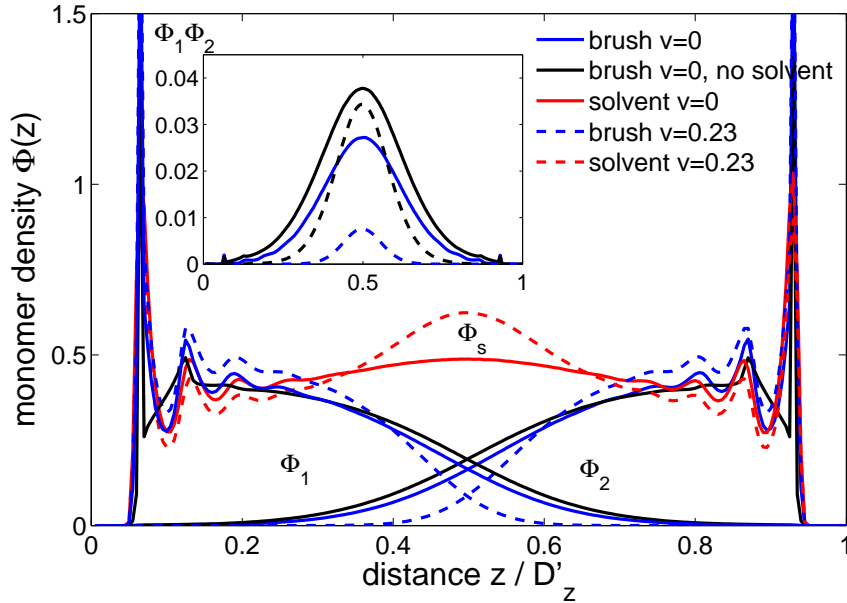
Figure 4.2: The density profiles at distance $D_z = 12$ for chain length $N = 30$ with solvent (red line). Solvent free brushes (black line) at equilibrium are compared to steady state motion at the largest shear velocity, $v = 0.23$ (dashed lines). The solvent free case in steady state is not shown, but the inset shows for both cases the overlap response.

duced using the interface width of chapter 3 [Eq. (3.21)] and connecting it to one relaxation time of the system. That relaxation time is used to predict a critical shear rate, which separates linear and non-linear behavior for a considered system. Microrheological observables, e.g. interpentration response or chains response, will be connected to macroscopic shear force responses.

4.1 Rheological observables

A snapshot of a typical configuration at constant shear velocity is depicted in Figure 4.1. In steady state, most of the chains incline along shear direction. On the other hand, due to fluctuations some chains tilt in the opposite direction.

4.1.1 Brush-Brush-Interpenetration

An analysis of the monomer and solvent densities, see Figure 4.2, reveals that solvent molecules accumulate at the substrates [67] and at the interface between
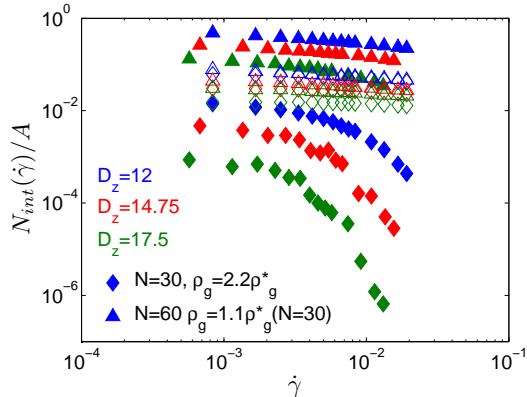
Figure 4.3: The number of binary inter-brush contacts per area as a function of the shear rate.
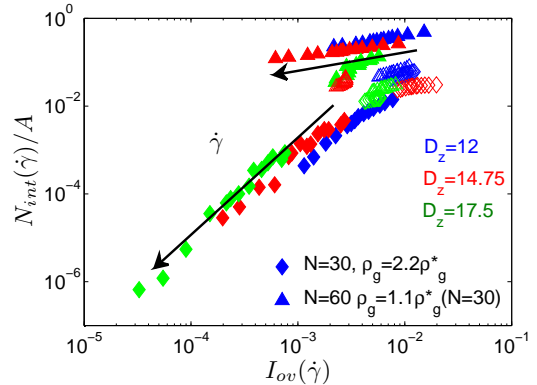
Figure 4.4: The number of binary contacts as a function of the overlap integral [Eq. (3.12)]. The arrow indicates the increasing shear rate.

the two brushes. Under shear the brushes become more dense and squeeze solvent molecules into the interfacial region between the brushes. The total density of the confined liquid remains almost constant. A further discussion can be found in Appendix C. Since only small density fluctuations are observed the systems keeps its low compressibility. The corresponding solvent-free case exhibits a larger brush thickness, both in static equilibrium and steady shear, which was already observed in Ref. [43]. The inset in Figure 4.2 demonstrates that the overlap between the brushes with explicit solvent is reduced compared to the solvent-free case. Furthermore, under sufficiently strong shear, in both cases the layer thickness decreases and leads to a reduced interpenetration between the brushes. Various numerical studies [37, 38, 40, 43, 62] have shown that the overlap between the grafted layers is linked to the macroscopic transport properties. In principle the overlap integral may be measurable experimentally. In the simulation the binary inter-brush interaction $N_{\text{int}}^{\text{bb}}$ is counted too, shown in Figure 4.4. The overlap is correlated with the number of binary contacts via [38]

$$N_{\text{int}}^{\text{bb}} \sim I_{\text{ov}} . \tag{4.1}$$

The number of binary contacts $N_{\text{int}}^{\text{bb}}$ varies over three orders of magnitude at equilibrium (not shown in Figure 4.3), but the solvent and solvent-free cases respond to the shear very differently. Interestingly, the cases with solvent respond stronger than their solvent free counterparts, which almost do not respond at all. Especially
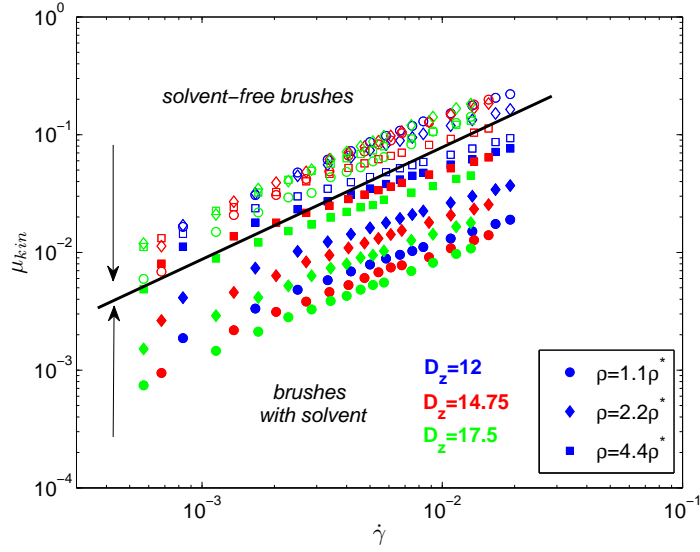
Figure 4.5: The kinetic friction coefficient as a function of shear rate $\dot{\gamma}$ for three wall separations ($D_z = 12$, 14.75, 17.5) all considered grafting densities and one chain length ($N = 30$). The solvent and solvent-free cases are separated by a line, for large grafting densities ρ_g the two cases must merge, which means that μ decreases with decreasing ρ_g (indicated by arrows) for the solvent systems, while it increases for solvent-free systems.

at large surface distances and small grafting densities solvent effects are important, when the brushes are dragged through the solvent, the chains will feel stronger forces than in the solvent-free case.

4.1.2 Kinetic friction coefficient

A qualitatively different behavior of solvent and solvent-free cases can be observed for the kinetic friction coefficient, μ_{kin}. The ratio between shear stress and normal stress defines μ_{kin} via

$$\mu_{\text{kin}}(\dot{\gamma}) = -\frac{\langle \sigma_{xz} \rangle}{\langle \sigma_{zz} \rangle} \, , \tag{4.2}$$

where $\langle \rangle$ denotes the time average of both stress components, the shear stress σ_{xz} and the normal stress σ_{zz}. The stresses are observed in steady state at constant velocity v and constant wall separation D_z. It was verified that the result is independent on weather the macroscopic response is measured by forces at the walls or by calculating elements of the stress tensor via the Irving-Kirkwood formula [60]. All systems keep their low compressibility even under strong shear. Therefore, f_z remains almost

independent of the shear rate $\dot{\gamma}$. For only one solvent-free system at the highest compression and highest grafting density a small increase is observed. While on the other hand, for all systems with explicit solvent the normal force increases slightly by approximately 5% at the highest wall velocity. The kinetic friction coefficient is shown in Figure 4.5 for the chain length $N = 30$ at three wall separations $D_z = 12, 14.75, 17.5$ and all three considered grafting densities. The solvent effects turn out to be important in polymer-brush lubrication and this observation is in agreement with the conclusions drawn in Ref. [68]. The presence of explicit solvent leads to smaller values of μ. In the solvent-free case the normal forces increase with increasing grafting densities and the ratio Eq. (4.2) decreases. Since both cases merge at larger values of ρ_g the kinetic friction coefficient has to increase with grafting density for systems with solvent. The arrows in Figure 4.5 indicate this behavior. However, both cases seem to change their behavior for larger shear rates. The friction coefficient grows not anymore linearly but has a steeper growth. Depending on their characteristic time scales, which determine the response of a given system to shear, see next section.

4.2   Zimm Dynamics

In chapter 3 the brushes were transferred into a dense melt of blobs of size ξ_c which are now dragged through a viscous medium η_s exhibiting friction. We assume Zimm dynamics inside the blob [64]. There are $\Phi\delta_{\text{semi}}/g_c$ blobs per unit area in the overlap region each having a friction coefficient $\eta_s\xi_c$ and with a steady state velocity $\dot{\gamma}D_z$, one can write

$$\frac{f_x}{A} \sim \frac{c\delta_{\text{semi}}}{g_c}\eta_s\xi_c\dot{\gamma}D_z \ . \tag{4.3}$$

With Eqs. (3.21) and (3.18) this leads to

$$f_x(\dot{\gamma}) \sim \left[N^{8\nu}\left(\rho_g a^2\right)^{2(1+\nu)}\left(\frac{a}{D_z}\right)^{4(1-\nu)}\right]^{1/3(3\nu-1)}\eta_s\dot{\gamma}A \tag{4.4}$$

in the linear response regime.

In linear response the transverse fluctuations of the free chain ends are equilibrium fluctuations. Defining the Weissenberg number Wi one may use the ratio of the work carried per chain to thermal fluctuations

$$Wi = \frac{f_x(\dot{\gamma})R_{g,x}(0)}{N_g k_B T} \ , \tag{4.5}$$

assuming all chains on average are stretched and inside the overlap sustaining the stress equally.

The Weissenberg number Wi for simple shear flow is defined as the shear rate times a relaxation time of the system

$$Wi = \dot{\gamma}\tau \ . \tag{4.6}$$

A typical relaxation time, which is used to define the Weissenberg number in single chain experiments, is the longest relaxation of the end-end distance, as done in Ref. [69], similarly used in section 6.8.2. It is questionable, whether it can also be used for a single brush in steady state shear, as done in Ref. [29]. Another lateral relaxation time relevant for single polymer brushes was introduced in Ref. [27] as $\tau \sim N^2$. The precise scale for Wi is arbitrary, because the brush has a broad spectrum of relaxation times, which may change when the brushes become compressed. It is not clear which of them is suited best.

In linear response the Weissenberg number is smaller than unity, while non-linear effects may take place for larger values. For further discussion the inverse of a relevant relaxation time of the bilayer is regarded as the critical shear rate, $\dot{\gamma}^* = 1/\tau$. To determine the critical shear rate we require $Wi = 1$, i.e.

$$Wi = \frac{\dot{\gamma}}{\dot{\gamma}^*} = \frac{f_x(\dot{\gamma})R_{\mathrm{g},x}(0)}{N_{\mathrm{g}}k_{\mathrm{B}}T} = 1 \ . \tag{4.7}$$

Using Eqs. (3.23) and (4.4) yields to

$$\dot{\gamma}^* \sim \frac{k_{\mathrm{B}}T}{\eta_{\mathrm{s}}a^3}\left[N^{-19\nu}(\rho_{\mathrm{g}}a^2)^{20\nu-13}\left(\frac{a}{D_z}\right)^{14\nu-11}\right]^{1/6(3\nu-1)} \ . \tag{4.8}$$

Now the critical shear rate is expressed by all control parameters (ρ_{g}, N, D_z), However, $\dot{\gamma}^*$ also depends on the prefactors η_{s} and a, which are depending implicitly on D_z, N, and ρ_{g}. Inserting Eq. (4.8) into Eq. (4.4) gives

$$f_x(\dot{\gamma}^*) \sim \frac{N_{\mathrm{g}}k_{\mathrm{B}}T}{a}\left[N^{-\nu}\left(\frac{\rho_{\mathrm{g}}a^3}{D_z}\right)^{2\nu-1}\right]^{1/2(3\nu-1)} \tag{4.9}$$

for the critical shear force. Both expressions Eqs. (4.8) and (4.9) define the transition between linear and non-linear response of the fluid.

4.2.1   Single chain segment inside the overlap

A more accurate approach takes fluctuations into account, where the stress is not carried by all chains inside the overlap, but the chains are now able to diffuse out
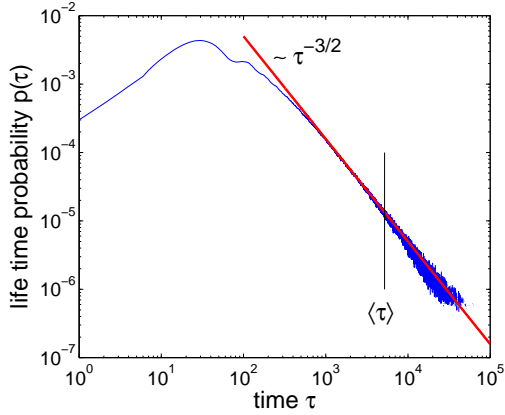
Figure 4.6: The log-log plot shows the life time distribution of the free end monomer that is able to move out of the overlap. The distribution is dominated by end-monomers diffusing in and out of the overlap for rather short times, for larger time the distribution reaches a maximum and decays with a power law $\sim \tau^{-3/2}$.

Figure 4.7: The relaxation time of the free end monomer inside the overlap for several system parameters. The theoretical expression [Eq. (4.12)] is represented by black dashed line. The red solid line indicates a guide to the eye for the acquired data.

of the interfacial zone. The characteristic time scale is given by the residence time of a chain's segment in the overlap region. This time is identified as the Rouse time of that segment, see Appendix D,

$$\tau_{\text{Rouse}} \sim N^2 \tau_0 \,, \tag{4.10}$$

where τ_0 is the time a monomer needs to diffuse over its own size. Now the Rouse time is transferred Zimm time

$$\tau_{\text{z}} \sim \left(\frac{N}{g_\Phi}\right)^2 \tau_\xi \,, \tag{4.11}$$

with $\tau_\xi \sim \eta_{\text{s}} \xi^3$ the relaxation time of a blob in a viscous medium η_{s}. With Eqs. (3.19), (3.20) and (3.18) the inverse diffusion time for a chain segment is given by

$$\frac{1}{\tau_{\text{z}}} \sim \frac{k_{\text{B}} T}{\eta_{\text{s}} a^3} \left[N^{-3\nu} \left(\frac{a^3 \rho_{\text{g}}}{D_z} \right)^{3\nu-2} \right]^{\frac{1}{(3\nu-1)}} . \tag{4.12}$$

The inverse relaxation time $1/\tau_{\text{z}}$ is defining a critical shear rate $1/\tau_{\text{z}} = \dot{\gamma}^*$, which will be derived later in section 4.2, where $\dot{\gamma}^*$ is the shear rate that separates the linear

response from the non-Newtonian behavior. The inverse relaxation time depends not only on the scaling variables but also on the prefactors η_s and a resulting from the discussion in section 3.3.1 and 3.3.2. In Figure 3.11 an example is shown, where the overlap is fitted by a Gaussian function yielding the width δ which is used to define a box, where in the simulation the life time of the free end is recorded. This is a mean first passage time problem. The life time distribution is plotted in Figure 4.6, where the distribution for short times is dominated by short life times of entering and immediately leaving free ends at the "absorbing" boundary. For intermediate times the distribution follows a scale free behavior with an exponent of approximately -1.5 until a noisy cut-off. The first moment giving the mean relaxation time of all considered systems is compared to Eq. (4.12) in Figure 4.7. Two strait lines are added to the plot in Figure 4.7 as a guide to the eye, the black dashed line represents the theoretical expression Eq. (4.12) and the red solid line implies a different exponent. The measurement assumes that each chain end contributes uniformly to the overlap, which is not fully true since the overlap is Gaussian and their contributions become position dependent.

4.3   Shear induced chain deformation

In previous studies microscopic responses of the chains were already reported, e.g. in Refs. [38, 45, 68]. In Figure 4.8 the extension of chains in shear direction, characterized by the radius of gyration, Eq. (3.2), is shown for a small selection of compressions and grafting densities for one chain length $N = 30$. All systems either tend to a power law (solvent free cases) others are already on it and tend for high shear rates to leave it again (high compressions and long chains). For small shear rates the brushes hardly respond to the shear. At large shear rates the chains stretch in shear direction, such that $R_{g,x}(\dot{\gamma}) \sim N$. With Eq. (3.23) we obtain

$$\frac{R_{\mathrm{g},x}^2(\dot{\gamma})}{R_{\mathrm{g},x}^2(0)} \sim N^{2-7\nu/2(1-3\nu)} \ . \tag{4.13}$$

On the other hand, we find Eq. (4.8)

$$Wi \sim \frac{1}{\dot{\gamma}^*} \sim N^{3(7\nu-2)/19\nu} \ , \tag{4.14}$$

such that for $Wi \gg 1$ we finally obtain

$$\frac{R_{\mathrm{g},x}^2(\dot{\gamma})}{R_{\mathrm{g},x}^2(0)} \sim Wi^{\beta} \ , \tag{4.15}$$

with $\beta \approx 0.5$. Since $\dot{\gamma}^*$ depends on the prefectors η_s and a calculating the critical shear rate with the known controlling parameters may be insufficient to generate a complete scaling picture. To set the scale for Wi an operational definition is used by plotting the raw data of Figure 4.8 as the ratio [left hand side of Eq. (4.15)] against the shear rate $\dot{\gamma}$ and shifting the data such that they superimpose onto the master curve given by Eq. (4.15). Such an approach sorts the raw data in a non-trivial scaling plot, see Figure 4.9, for all considered parameter combinations.

Additionally, the ratio of the stationary values in gradient (z) direction is added to Figure 4.9, showing a weak decrease for large Weissenberg numbers. A few systems exhibit a tendency to saturate for larger Wi due to their finite compressibility. The data used to create the plot is composed in tabular form in Appendix B. The table shows, how the systems align due to their intrinsic relaxation time $1/\dot{\gamma}^*$, e.g. the solvent free systems have a smaller relaxation time compared to systems with explicit solvent leaving linear response earlier due to additional monomer-solvent friction.

A similar observation can be made for the surface separation. The force that drives the system out of the linear response regime increases with compression, likewise observed in previous simulations [36] and experiments [26]. Furthermore, the universal behavior of the structural response in shear direction is independent of whether the solvent is explicitly included or not. This is attributed to the hydrodynamic correlations accounted for the DPD thermostat even for solvent-free systems.

4.4   Shear force and shear viscosity

For large shear rates, the chains stretch strongly, such that the shear force is proportional to the total number of monomers,

$$f_x(\dot{\gamma}) \sim N_g N \dot{\gamma} D_z \sim N \ . \tag{4.16}$$

Inserting Eq. (4.4) into Eq. (4.16) yields

$$\frac{f_x(\dot{\gamma})}{f_x(\dot{\gamma}^*)} \sim Wi^\alpha \ , \tag{4.17}$$

with $\nu = 0.588$ we obtain $\alpha = 3(7\nu - 2)/19\nu \approx 0.54$. The shear viscosity is given by [70]

$$\eta = \frac{\sigma_{xz}}{\dot{\gamma}} \ . \tag{4.18}$$

Another scaling plot may be obtained from
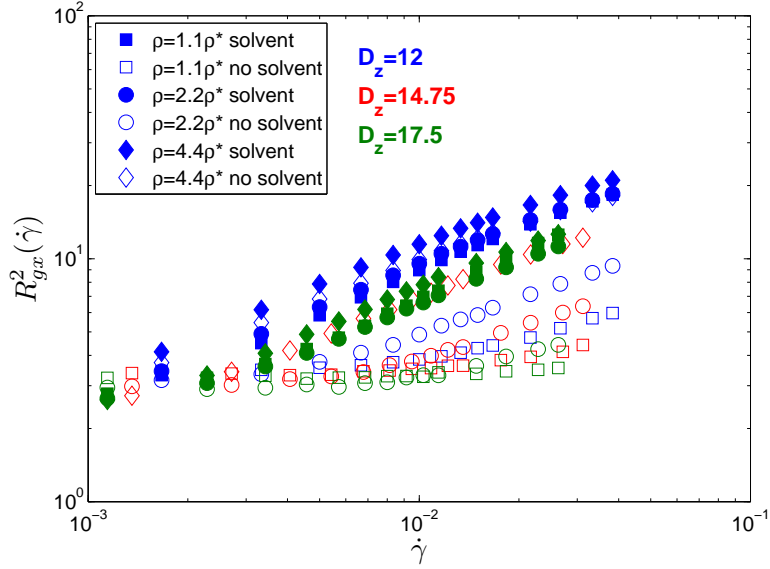
Figure 4.8: A log-log plot of the chain extension $R^2_{g,x}(\dot{\gamma})$ for selected systems ($N = 30$) lateral responding to shear. Systems without solvent respond less to the shear then systems with solvent.
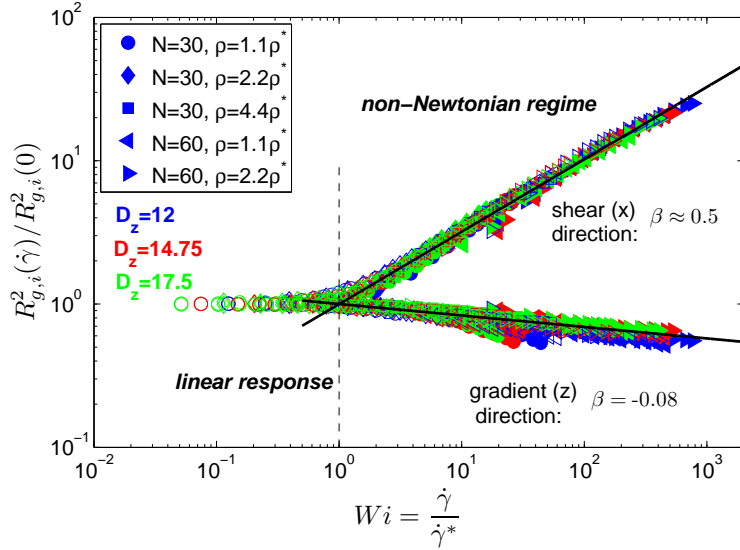
Figure 4.9: A double logarithmic scaling plot for the chain extension in shear (x) and gradient (z) directions as a function of the Weissenberg number. For $Wi \leq 1$ no chain deformation is observed. Upon increasing Wi, the grafted layers shrink slightly as indicated by the exponent $\beta = -0.08$. The chains stretch in shear direction, following the universal power law with $\beta \approx 0.5$. Solvent (filled symbols) and solvent-free (open symbols) are brought onto the same master curve.
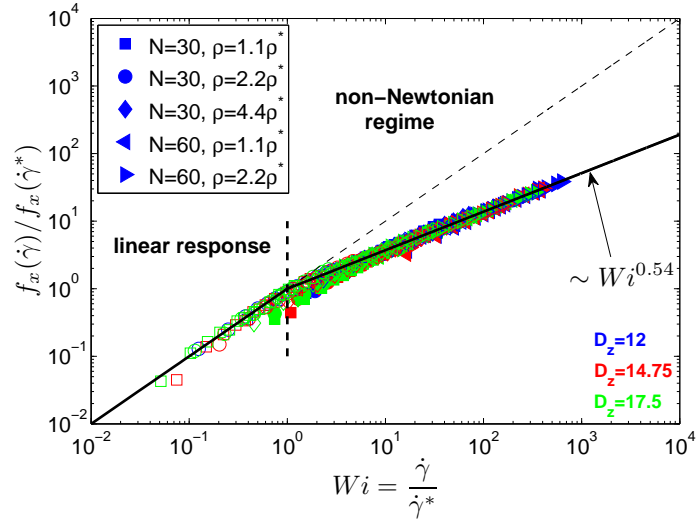
Figure 4.10: A log-log plot for the normalized shear force as a function of the Weissenberg number. Filled symbols represent systems with explicit solvent and empty symbols the solvent-free counterparts for all considered system parameters. For $Wi \ll 1$ the shear force is linear, while for $Wi \gg 1$ the response becomes non-Newtonian with $f_x(\dot{\gamma})/f_x(\dot{\gamma}^*) \sim Wi^{0.54}$.
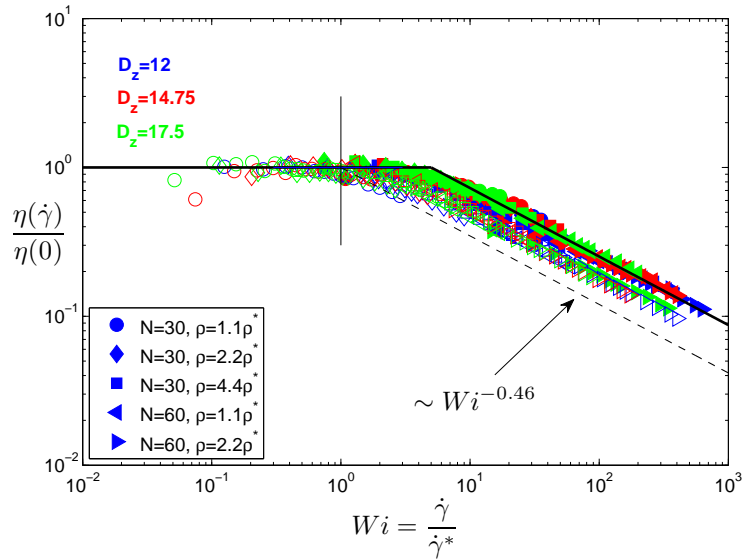
Figure 4.11: A double logarithmic plot of the normalized shear viscosity versus the Weissenberg number. The normalization constant $\eta(0)$ follows from shifting the data along the ordinate, such that the ratio $\eta(\dot{\gamma})/\eta(0) \to 1$ for $Wi \ll 1$. The solvent free systems start in the linear response regime, where $\eta(\dot{\gamma})$ remains constant. At $Wi \approx 1$ the transition occurs onto the power-law, where most systems with explicit solvent superimpose. The shift in the abscissa in the transition region occurs from very dilute solvent-free systems towards increasing grafting densities to almost all systems with solvent. In between the increased grafting density increases the shift towards larger Wi.
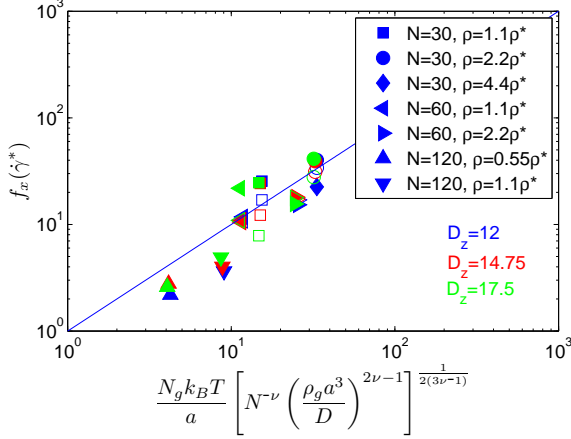
Figure 4.12: The critical shear rate is compared with Eq. (4.9), the blue line indicates a linear depends, which in good agreement with the simulation.
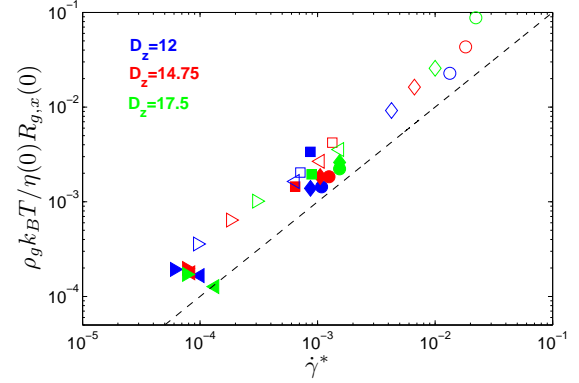
Figure 4.13: Each determined critical shear rate is compared to Eq. (4.21).

$$s = \frac{\eta(\dot{\gamma})}{\eta(0)} \; , \tag{4.19}$$

where the zero-shear viscosity $\eta(0)$ has to be examined for each system individually. Calculating the zero-shear viscosity is a task of its own and computing it is rather difficult due to the bad signal-to-noise ratio at small shear rates. In principal, $\eta(0)$ can be calculated if the Weissenberg number is expressed via Eq. (4.5) and the shear force being proportional to the shear rate. So one can find in linear response

$$\eta(0) = \frac{f_x(\dot{\gamma})}{A\dot{\gamma}} \tag{4.20}$$

leading with Eq. (4.5) to

$$\gamma^* \approx \frac{\rho_g k_B T}{\eta(0) R_{g,x}(0)}, \tag{4.21}$$

where $\rho_g = N_g/A$ has been used. From Eq. (4.21) it is possible to determine the critical shear rate if the zero-shear viscosity is known, additionally it emphasis the strong correlation between the chain deformation and the macroscopic response. The zero-shear viscosity is determined by plotting the viscosity as a function of the Weissenberg number and shifting the data along the ordinate for systems showing linear response in such that the ratio (4.19) becomes unity. Several systems reveal a transitional behavior from linear to non-linear response, especially those systems with no solvent and high grafting densities, see open symbols in Figure 4.11. The

data follow a power-law,

$$\frac{\eta(\dot{\gamma})}{\eta(0)} \sim Wi^{-0.46} \, . \tag{4.22}$$

A slight shift appears in the data for Weissenberg numbers larger than unity. Systems with explicit solvent mostly exhibit the power-law behavior, they do not display linear response well. The data are carefully shifted onto the data without explicit solvent, which reveal a transition from linear to non-linear response. However, when using the same values of $\dot{\gamma}^*$ as obtained from Figure 4.9, the transitional region does not occur at $Wi = 1$ but slightly later. On the other hand, very diluted solvent-free systems (lowest grafting density) change the regime exactly at $Wi = 1$ and follow the power law. If now the overall density is changed either increasing the grafting densities with similar wall separations or compressing the same number of chains, the transition shifts to larger Weissenberg numbers. The origin of the effect is unknown but is somehow related to the density inside the system.

Experimental observations done in microrheology with non-Newtonian fluids also exhibit similar shear thinning effects. In literature several phenomenological and empirical models have been proposed [71]. One possible fit function follows from the Carreau-Yasuda model, which describes a pseudoelastic flow

$$\eta(\dot{\gamma}) = \eta_\infty + (\eta_0 - \eta_\infty) \left[1 + \left(\frac{\dot{\gamma}}{\dot{\gamma}^*} \right)^q \right]^{\frac{n-1}{q}} \, , \tag{4.23}$$

with five parameters observed experimentally, asymptotic viscosity limits at zero-shear η_0 and infinite shear rate η_∞. The exponent $n-1$ is known from the scaling theory, one the other hand q represents the width of the transition region between η_0 and power-law region. The transition parameter depends an the scaling variables in a non-universal way,

$$q = q(\rho_g, N, D_{\mathrm{z}}) \, . \tag{4.24}$$

The scaling theory discussed earlier predicts only the behavior for small and for large Weissenberg numbers and no prediction is made for the transitional region. Experimental limitations prevent the exploration of equivalently large compressions and shear rates as they can be studied in simulations. However, some experimental data that reach the non-Newtonian regime have become available. Schorr *et al.* recently measured shear forces in bilayers of polystyrene brushes on mica in a SFA experiment [26]. In good solvent (toluene), the authors observe linear response over a wide range of compressions and shear rates. However, at large compression

($h \approx 220 \mathring{A}$ unperturbed brush height, $D_z = 95 \mathring{A}$) they find a sublinear increase of the shear force with sliding velocity. At the crossover between linear and non-linear behavior the critical shear rate $\dot{\gamma}^*$ and critical shear force $f_x(\dot{\gamma}^*)$ can be found by superimposing the data with the theoretically predicted curves. For comparison a solvent-free system, which is similar to the experimental one ($D = 14.75, N = 60$, and $\rho_g = 1.1 \rho_g^*$) with a corresponding compression of $2h/D \approx 4.1$ [58] is shown in Figure 4.14. Additionally, in the same study, Schorr *et. al.* performed Brownian dynamics simulations using a Brinkman type equation to describe the solvent flow. For their parameters they observe mostly linear behavior but also data following the scaling law beyond linear response. The simulation example is taken from Ref. [26] and added to Figure 4.14. A recent study by Goujon *et. al.* [44] investigated sheared polymer brushes using MD simulation with a DPD thermostat with larger intrinsic friction. They operate in the grand-canonical ensemble, allowing the particle number to fluctuate. That approach guarantees a constant normal pressure at all shear rates. In Ref. [72] the friction coefficient is given for one example of parameters. Since f_z is constant, the dependence of the friction coefficient and f_x on the Weissenberg number must be similar. The data is shown in Figure 4.14, where the experimental data and three independent studies follow the theoretical curves in rather good agreement.

4.5   Other regimes

In chapter 2 the interfacial region was derived from the MWC-brush approach by transferring the overlap melt into the semi-dilute regime $\delta_{\mathrm{melt}} \to \delta_{\mathrm{semi}}$. In section 4.2 hydrodynamic interaction were taken into account, Zimm dynamics inside the blob was assumed. That hydrodynamic interaction maybe fully screened and that the monomers obey Rouse dynamics instead of the Zimm dynamics. In this situation the chains are still swollen and therefore the Flory exponent $\nu = 0.588$ remains. On the other hand, one may continue with the melt regime where the excluded volume interactions are screened ($\nu = 1/2$), as well. The general Ansatz for the Stokes force changes where the number of monomer instead of the number of blobs inside the overlap region are exhibiting the friction [Eq. 4.3]. For the semi-dilute dynamics
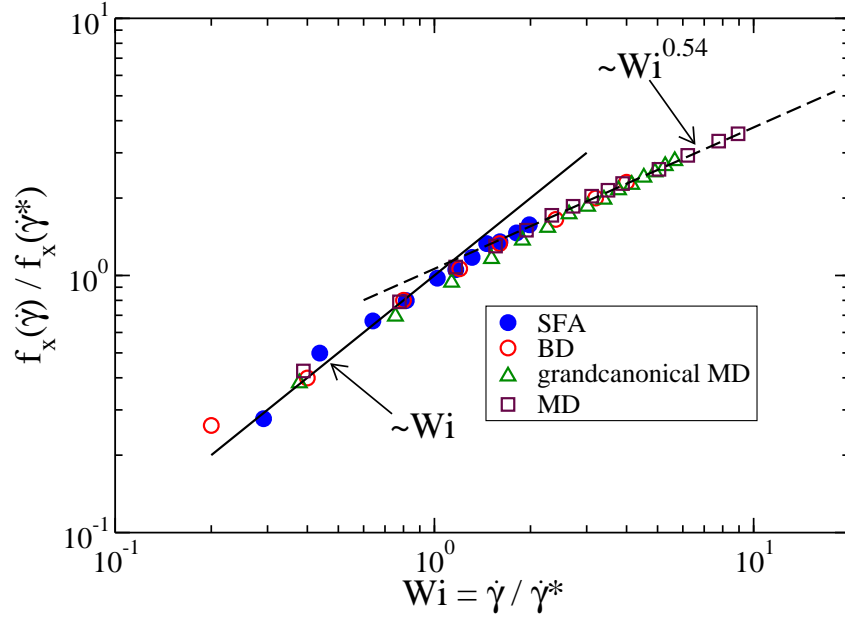
Figure 4.14: SFA data from PS/PVP [25/4] k in toluene, Brownian dynamics simulations, both taken from Ref. [26], and results of grand-canonical MD-simulations [72]. All data show linear behavior for $Wi \leq 1$ and a reasonable agreement to the power-law behavior beyond linear response.

without hydrodynamics the linear friction is given by

$$f_x(\dot{\gamma}) \sim c\delta_{\text{semi}}\psi\dot{\gamma}D_{\text{z}}A \tag{4.25}$$

and for the melt condition

$$f_x(\dot{\gamma}) \sim c\delta_{\text{melt}}\psi\dot{\gamma}D_{\text{z}}A \ , \tag{4.26}$$

where ψ is a friction coefficient.

We follow the same arguments as in section 4.2 and insert for each distinguished case the relevant overlap expressions. That leads to different values for the exponents α and β. An overview of all three cases is given in the following table 4.5

	semi-dilute with hydrodynamics $\nu = 0.588$	semi-dilute without hydrodynamics $\nu = 0.588$	melt $\nu = 0.5$
overlap width δ	$a\left[N^{2\nu}(\rho_g a^2)^{2(1-2\nu)}\left(\frac{a}{D_z}\right)^{1-\nu}\right]^{\frac{1}{3(3\nu-1)}}$	$a\left[N^{2\nu}(\rho_g a^2)^{2(1-2\nu)}\left(\frac{a}{D_z}\right)^{1-\nu}\right]^{\frac{1}{3(3\nu-1)}}$	$\left(\frac{N^2 a^4}{D_z}\right)^{\frac{1}{3}}$
lateral extension $R_{g,x}$	$a\left[N^\nu\left(\frac{D_z}{\rho_g a^3}\right)^{2\nu-1}\right]^{\frac{1}{2(3\nu-1)}}$	$a\left[N^\nu\left(\frac{D_z}{\rho_g a^3}\right)^{2\nu-1}\right]^{\frac{1}{2(3\nu-1)}}$	$a N^{1/2}$
Ansatz: Stokes friction per unit area $(Wi \leq 1)$	$f_x(\dot\gamma) \sim \frac{c\delta}{g_c}\eta_s \xi_c \dot\gamma D_z$	$f_x(\dot\gamma) \sim c\delta\psi\dot\gamma D_z$	$f_x(\dot\gamma) \sim c\delta\psi\dot\gamma D_z$
$\frac{f_x(\dot\gamma)}{A} \sim$	$\left[N^{8\nu}(\rho_g a^2)^{2(1+\nu)}\left(\frac{a}{D_z}\right)^{4(\nu-1)}\right]^{1/3(3\nu-1)}\eta_s\dot\gamma$	$\left[N^{11\nu-3}(\rho_g a^2)^{5\nu-1}\left(\frac{a}{D_z}\right)^{8\nu-2}\right]^{1/3(3\nu-1)}\psi\dot\gamma$	$N^{5/3}a\left(\frac{a}{D_z}\right)^{1/3}\rho_g\psi\gamma$
$\frac{\dot\gamma}{\dot\gamma^*} = \frac{f_x(\dot\gamma)R_{g,x}(0)}{N_g k_B T}$ $\dot\gamma^* \sim$	$\frac{k_B T}{\eta_s a^3}\left[N^{-19\nu}(\rho_g a^2)^{20\nu-13}\left(\frac{a}{D_z}\right)^{14\nu-11}\right]^{1/6(3\nu-1)}$	$\frac{k_B T}{\psi a^2}\left[N^{6-25\nu}(\rho_g a^2)^{7(2\nu-1)}\left(\frac{a}{D_z}\right)^{8\nu-5}\right]^{1/6(3\nu-1)}$	$\frac{k_B T}{\Psi a^2}\left(\frac{D_z}{a}\right)^{1/3}N^{-\frac{13}{6}}$
critical shear force $(Wi = 1)$ $f_x(\dot\gamma^*) = \frac{N_g k_B T}{R_{g,x}(0)}$	$\frac{N_g k_B T}{a}\left[N^{-\nu}\left(\frac{\rho_g^3 D_z}{a}\right)^{2\nu-1}\right]^{1/2(3\nu-1)}$	$\frac{N_g k_B T}{a}\left[N^{-\nu}\left(\frac{\rho_g^3 D_z}{a}\right)^{2\nu-1}\right]^{1/2(3\nu-1)}$	$\frac{N_g k_B T}{a N^{1/2}}$

non-linear response	semi-dilute with hydrodynamics	semi-dilute without hydrodynamics	melt
$R_{g,x}(\dot\gamma) \sim N$ $\frac{R_{g,x}^2(\dot\gamma)}{R_{g,x}^2(0)} \sim Wi^\alpha$	$\alpha = 6(5\nu - 2)/19\nu$	$\alpha = 6(5\nu - 2)/(25\nu - 6)$	$\alpha = 6/13$
$\nu \approx 0.588$	$\alpha \approx 0.5$	$\alpha \approx 0.65$	$\alpha \approx 0.46$
$f_x(\dot\gamma) \sim N$ $\frac{f_x(\dot\gamma)}{f_x(\dot\gamma^*)} \sim Wi^\beta$	$\beta = 3(7\nu - 2)/19\nu$	$\beta = 3(7\nu - 2)/(25\nu - 6)$	$\beta = 9/13$
	$\beta \approx 0.54$	$\beta \approx 0.73$	$\beta \approx 0.69$
$\frac{\eta(\dot\gamma)}{\eta(0)} \sim Wi^\zeta$ $\zeta = \beta - 1$	$\zeta = -2(3-\nu)/19\nu$	$\zeta = -4(\nu - 2)/(25\nu - 6)$	$\zeta = -4/13$
	$\zeta \approx -0.46$	$\zeta \approx -0.27$	$\zeta \approx -0.31$

Table 1: Overview of three theoretical regimes of polymer brushes in steady state sliding. The left column summarizes relevant observables needed for the scaling theory. The second column displays the swollen brushes quantities with hydrodynamics, the third column excludes the hydrodynamics, and the fourth column displays the quantities in the melt regime. The second half of the table shows depending on the regime how the exponents vary.
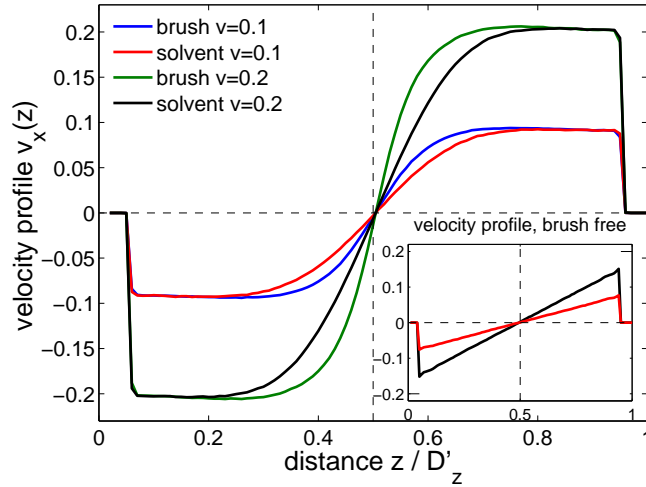
Figure 4.15: The velocity profiles of two opposing brushes and solvent at two different wall velocities. The inset shows the velocity profiles of pure solvent systems at the same velocities as the brushes. The solvent is not able to follow the wall velocities due to a slippage at the walls.

4.6 Velocity profile

The fluid components are driven by the boundaries, intrinsic interactions distribute the acting forces in such that a velocity profile is established reflecting the minimum rate of energy dissipation [73]. The velocity profiles of both fluid components are symmetric around $D_z/2$, where at the substrate a no-slip boundary condition is implied by the brushes. The solvent molecules are dragged with the brushes. In the middle of the channel both components establish a distinct linear Newtonian-like flow profile, see Figure 4.15. For the choice of parameters all hydrodynamic brush flow fields exhibit at the crossover from the wall to the linear profile a small region, where segments of a chain are faster than the driving velocity. The origin of this effect is a quasi-cyclic motion of individual chain end, as reported in Refs. [31, 74, 75]. Since the temperature profile is not constant, the slight cooling towards the walls may induce small convection amplifying this effect.

The inset in Figure 4.15 shows a flow profile when the attached polymer chains are removed, but the walls are driven with the same velocity. In this case, a linear profile along the whole channel is created. Due to the non attractive interaction of the dimers towards the walls a slip boundary is present, where the walls are moving slightly faster than the fluid. In chapter 6.8.2 this effect is discussed further.
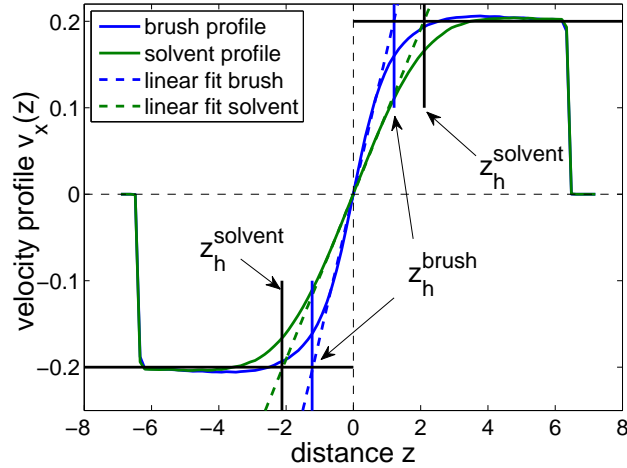
Figure 4.16: The velocity profiles of two opposing brushes and solvent. The linear slopes are extrapolated to the wall velocities defining the hydrodynamic boundary (dashed blue and green lines). Before the crossover to the linear profile the brushs' velocity profile reveals a faster flow due to the cyclic tumbling motion of the grafted molecules in shear flow, see Ref. [76].

The friction depends on the interface between the two brushes, the local interaction and the "slip" of both substrates. In order to incorporate microscopic friction in a continuum description, the Navier-Stokes equation can be used employing the Navier boundary condition [77]

$$\eta \left. \frac{\partial v_x(z)}{\partial z} \right|_{z=z_\mathrm{h}} = \frac{\eta}{b} v_x(z = z_\mathrm{h}) , \tag{4.27}$$

based on the equality of the viscous stress $\sigma_\mathrm{viscous} = \eta \partial v_x(z)/\partial z$ and the frictional stress $\sigma_\mathrm{friction} = \eta/b v_x(z)$ at the boundary, $v_x(z)$ denotes the flow velocity in x-direction along z of the liquid parallel to the walls, η the bulk viscosity in linear response. The boundary condition depends on two parameters b and the position z_h, which are not known a priori. To extract both parameters b and z_h Müller and Pastorino [76] discuss two qualitatively different types of flows, planar shear flow (Couette flow) and pressure-driven flow (Poiseuille flow). They find that both flow types have to be studied in order to reveal a consistent determination. Since the Poiseuille flow along the gap is not studied the slip length cannot be determined and the discussion will concentrate on the hydrodynamic boundaries for the Couette flow.

At the center of the channel, the flow is described by the Navier-Stokes equation
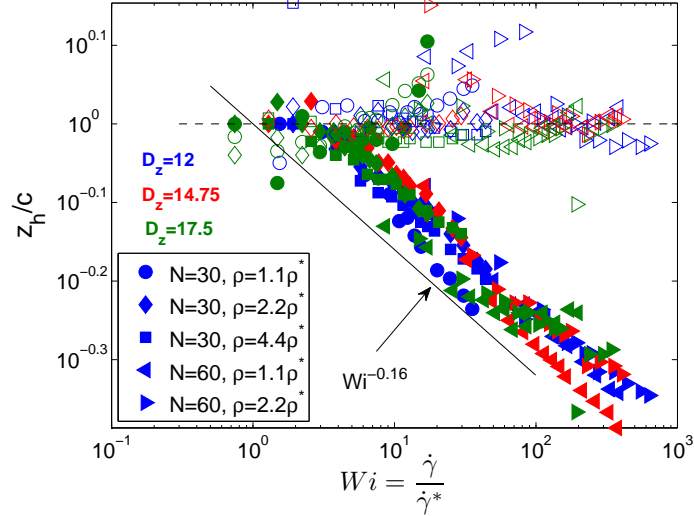
Figure 4.17: Hydrodynamic boundaries $z_\mathrm{h}^\mathrm{brush}$ (filled symbols) and $z_\mathrm{h}^\mathrm{solvent}$ (open symbols) as a function of the Weissenberg number. The measured $z_\mathrm{h}^\mathrm{brush}$ are normalized by an arbitrary constant c and follow a phenomenological power law $z_\mathrm{h}^\mathrm{brush} \sim Wi^{-0.16}$. On the other hand, the boundary condition for the solvent does not change with shear rate.

yielding a linear velocity profile

$$v_x^\mathrm{lin}(z) = \dot\gamma(z \pm z_\mathrm{c}) \ , \tag{4.28}$$

where $z_\mathrm{c} = D_z/2$ is the position of the linear profile extrapolates to zero, at the middle of the gap. The linear profile is extrapolated to the wall velocities and the intersection point of wall velocity defines the hydrodynamics boundary z_h. For each system that is driven into steady state with different wall velocities such a profile is recorded. Since the explicit molecules are only dragged with the brushes, they establish a slightly different velocity profile and therefore their own hydrodynamic boundary. The dependence of the hydrodynamic boundary on the shear rate is shown in Figure 4.17. All measured z_h are scaled such that the data assemble on a master curve. With increasing shear rate the brushes tilt further, the layer thickness decreases and this influences $z_\mathrm{h}^\mathrm{brush}$ reducing the effective gap size. On the other hand, the hydrodynamic boundary of the solvent molecules is not effected by the shear, $z_\mathrm{h}^\mathrm{solvent}$ remains almost constant.

The velocity profiles can be fitted with sigmoidal shaped functions, like hyperbolic

tangent [47] or Gaussian error functions (erf)

$$\phi(z) = \frac{1}{\sqrt{2\pi}} \int_{\infty}^{z} e^{-\frac{z'^2}{2}} dz' \ . \tag{4.29}$$

To determine the interpenetration length of both brushes at equilibrium a Gaussian fit function was used, see Figure 3.11. In steady state the general shape of the overlap does not change and remains fittable with a Gaussian function. Since the brushes respond by inclining in shear direction reducing the brush thickness for large Weissenberg numbers, the overlap becomes a function of the shear rate as well. If one fits the overlap profile in steady state via a Gaussian function and integrate it using Eq. (4.29) the resulting sigmodial shaped error function can be used to fit the resulting brush velocity profiles in steady state for the different shear rates. In Figure 4.18 three velocity profiles (blue curve corresponds to brush profiles and green curve correspond to solvent profile) for different wall velocities are fitted with their corresponding integrated overlap fit. The error functional fit was normalized and shifted on the ordinate axis. Hypothetically, a shift factor can be introduced shifting the function on the abscissa to fit the corresponding solvent profile, as well. The inset shows the slopes of the linear parts for the all velocity profiles [brushes (blue) and solvent (green)) and the integrated overlap fit (red). We find a strong correlation between overlap and velocity profiles of the brushes. In the work of F. Goujon, et. al. [47] a not further specified sigmoidal function, and in the PhD-thesis of Goujon [72] a hyperbolic tangent function are used to fit the velocity profiles of both components. A microscopic reasonable motivation for those fits is not given. To describe the flow field inside the brush one often uses the Brinkman equation [19, 24]

$$\eta_{\mathrm{s}} \nabla^2 \vec{v} = \frac{\eta_{\mathrm{s}}}{\xi^2(\rho)} \vec{v} + \nabla \vec{P} \ . \tag{4.30}$$

Here, η_{s} is the solvent viscosity, the screening length ξ may depend on the local density. The left hand side of the equation is the viscous force due to dissipation within the flowing liquid, which is balanced by the friction term arising from flow past the polymer segments and a pressure gradient. For simple shear flow, the pressure is constant and the gradient (z) component of the velocity satisfies

$$\frac{\partial^2 v(z)}{\partial z^2} = \frac{v(z)}{\xi^2(z)}. \tag{4.31}$$

50
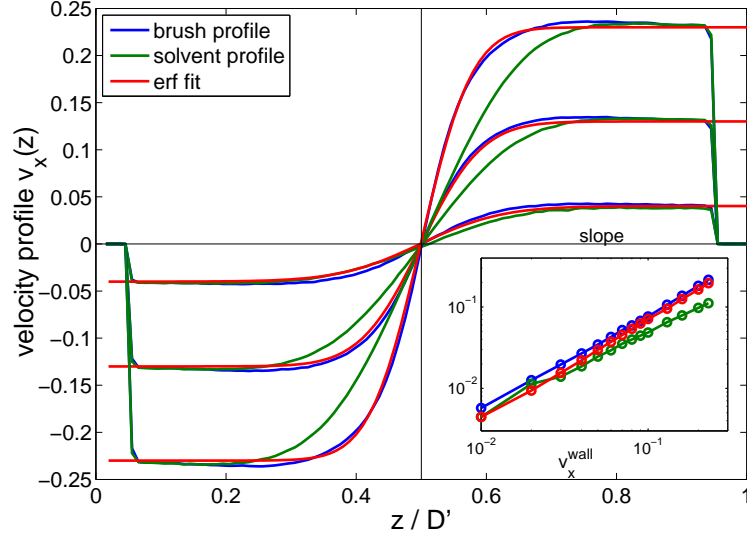
Figure 4.18: For three different wall velocities the brush (blue curves) and solvent (green curves) velocity profiles and the corresponding erf-fits (red curves) [Eq. (4.29)] in steady state are shown. The erf-fits are in very good agreement with the original brush velocity profiles. The inset compares the slopes of the linear part of the profiles as a function of the wall velocity [Eq. (4.28)].

Solving Eq. (4.31) by assuming $\xi(z) = \xi$ is constant along the z-direction and the boundary condition

$$v(-D/2) = v_0 \quad \text{and} \quad v(0) = 0 \tag{4.32}$$

gives

$$v_x(z) = \frac{v_0}{\sinh\left(\frac{D}{2\xi}\right)} \sinh\left(\frac{z}{\xi}\right) \quad \text{for} \quad -D/2 < z < 0 . \tag{4.33}$$

The hyperbolic sinus function is a basic solution that satisfies the Brinkman equation, which deviates strongly from the functional dependence indicated in Figure 4.18.

In the work of Clement [78] a linear combination of Airy-functions solves the Brinkman equation for the flow field of a solvent interpenetrating a single brush near the θ-point, similar to Ref. [24]. The porosity $\xi(z)$ of the single brush follows the parabolic of mean field density profile, Eq. (3.15).

In the work of Urbakh, et al. [73] the velocity profile of a confined liquid originates from minimizing Ginzburg-Landau-type free-energy functional resulting in a Brinkman-type of equation, which is solved for independently acting walls. A linear

combination of modified Bessel and Hankel functions can be fitted to the velocity profiles.

Their theoretical studies and the numerical findings may be useful to understand theoretically the established steady state velocity profiles of both components.

4.7   Summary

The chapter presented the lubrication of two opposing polymer brushes with rather short chains extending the equilibrium scaling theory of chapter 2. The response of two opposing brush covered surfaces to stationary Couette flow of different shear rates was measured. We varied the compression of the confined fluid, molecular parameters, grafting density, and chain length. Solvent-free systems have been compared to systems that included explicit solvent molecules.

Very different responses to shear are observed, depending on the considered parameter combinations. For small grafting densities, systems with explicit solvent leave the linear response regime earlier than their solvent-free counterparts and the kinetic friction coefficient is significantly smaller, a fluid layer between the brushes is formed helping to lubricate.

The regime of linear response is left earlier with increasing compression, grafting densities or chain length. Generally, the non-Newtonian behavior sets in at smaller shear rates when the density of the system is increased. Several previous computer studies confirm the small change of the brush thickness, and the stretching of the polymer chains along the shear direction, which goes along with a non-Newtonian response of a macroscopic observable, which grows sublinearly with sliding velocity. The data indicate a swelling of chains in the shear direction that can be described by a universal power-law increase of chain extension with the Weissenberg number. Using the shear-induced deformation of chains, one can demonstrate how to estimate the critical shear rate. This allows to superimpose the data of all considered parameter combinations, revealing a strong relation between the chain deformation and the macroscopic response. Despite their distinct differences, solvent and solvent-free cases can be described consistently.

The developed scaling theory allows not only to explain the conformational change of the bilayer but also the macroscopic response to shear. Furthermore, recent experimental data and results of very different simulation models are reproduced by

the analytical approach.

The flow of solvent molecules past the compressed bilayer remains open. Usually, the semi-empirical Brinkman equation is used and the single brush profile describes the porosity of the brush. When the bilayer becomes compressed the overall density becomes constant implying a constant mesh size. The solution for constant mesh size does not fit to the solvent velocity profile. The frictional properties along the gap result in the components' velocity distributions. While in the middle a Couette flow is established with larger effective shear rate, the effective gap size given by the hydrodynamic boundaries of the brushes becomes smaller. Their position inside the fluid changes with shear rate and is somehow related to the bilayer thickness. Since, a major frictional contribution is given by the interfacial zone, the integrated overlap width of the brushes match well the observed velocity profiles of the brushes. Slight deviation from the fit appear due to the quasi-cyclic motion of the chain ends in the flow.

Chapter 5

Two opposing brushes in non-stationary shear

Finite substrate sizes in real life and fluctuating driving strengths cause the complex fluid to respond to non-stationary motion in a mechanical stable manner, otherwise instabilities may generate fatigue or failure of the fluid. This chapter deals with the response to non-stationary conditions, the onset and inversion of motion. At first the transition from equilibrium to stationary sliding is discussed. The change of the direction of movement of the walls by changing the pre-sign of the velocity is considered here as the inversion regime. In terms of large amplitude oscillatory shear the rapid inversion of the confining substrates offers a unique experimental setup for testing mechanical stability of the considered material by varying strength and period of the external perturbation. Other transient regimes like stress relaxation after cessation of steady flow or sudden shear displacement are not considered. A scaling theory is developed where the transition time of the brush bilayer is determined.

5.1 Scaling the time series

Depending on the molecular parameters defining the critical shear rate and therefore a critical time scale the brushes respond differently to the shear. For the linear regime ($Wi \ll 1$) the chains do not respond, while for the non-Newtonian regime ($Wi \gg 1$) the chains swell in shear direction. In this driving regime the relaxation towards the non-equilibrium state is dominated by the driving shear rate, diffusion

54
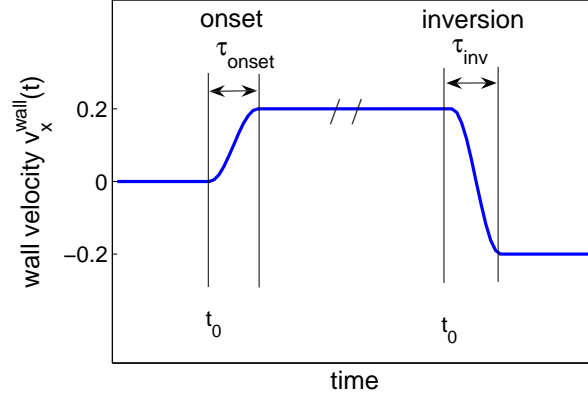
Figure 5.1: Starting from equilibrium, where the walls are at rest, at t_0 the walls are set in motion, and in a short time τ_{onset} the walls reach their designated velocity v_x^{wall}. During the inversion the velocity continuously goes from $v_x = -v_x$ in a short time τ_{inv}.

is not relevant. One may argue that the chain extension in steady state is given by

$$R_{\text{g},x}(\dot{\gamma}) \sim \dot{\gamma} D_z \tau_{\text{bilayer}} \, , \tag{5.1}$$

where τ_{bilayer} is the relaxation time to reach the steady state and $\dot{\gamma} D_z$ the wall velocity. Therefore, during the transition the chain extension becomes a function of time, $R_{\text{g},x}(\dot{\gamma}, t)$. If the shear rate is large enough one can assume that inertia is negligible and the transition is dominated by the walls driving

$$R_{\text{g},x}(\dot{\gamma}, t) \sim \dot{\gamma} D_z t \, . \tag{5.2}$$

In steady state the chains are strongly stretched for $Wi \gg 1$, while during the inversion the extension undergoes a minimum, whereas for the onset of motion the minimal extension of the chain is given by the equilibrium lateral extension, $R_{\text{g},x}(0)$. To describe the transition one can find the Ansatz

$$R_{\text{g},x}(\dot{\gamma}, t)/R_{\text{g},x}(\dot{\gamma}) \sim 1 - \dot{\gamma} D_z t/R_{\text{g},x}(\dot{\gamma}) \, . \tag{5.3}$$

Inserting Eq. (5.1) into the right side of Eq. (5.3) yields

$$R_{\text{g},x}(\dot{\gamma}, t)/R_{\text{g},x}(\dot{\gamma}) \sim 1 - t/\tau_{\text{bilayer}} \, . \tag{5.4}$$

In steady state the chain extension is given as a function of the Weissenberg number Wi [Eq. (4.15)]

$$\frac{R_{\text{g},x}^2(\dot{\gamma})}{R_{\text{g},x}^2(0)} \sim \left(\frac{\dot{\gamma}}{\dot{\gamma}^*} \right)^{\beta} \tag{5.5}$$

with $\beta \approx 0.5$, yielding the transition time

$$\tau_{\text{bilayer}} \sim \frac{R_{\text{g},x}(0)}{D_z} \dot{\gamma}^{*-\frac{\beta}{2}} \dot{\gamma}^{\frac{\beta}{2}-1} \, , \tag{5.6}$$

where $R_{\text{g},x}^2(0)$ is the squared lateral chain extension in equilibrium. The transition time becomes shear-rate dependent. For each individual system (given by the control parameters N, ρ_{g}, D_z) a bilayer relaxation time τ_{bilayer} exists that superimposes the transition related time series.

5.2   Onset of motion

Following the shear protocol of Figure 5.1 the walls accelerate in a small time τ_{onset}, where the brushes are unable to relax. In Figure 5.2 the transition from equilibrium towards steady state for the chain extension described by the end-to-end vector component $R_{\text{ee},x}(t)$, normalized by the steady state value $R_{\text{ee},x}(\dot{\gamma})$, is shown for a variety of systems. The shear rate $\dot{\gamma}$ and the transition time $\tau_{\text{onset}} = 2500\Delta t$ are the same for all systems. Depending on N and ρ_{g} the chains need their intrinsic time to reach steady state. The brushes with chain length $N = 120$ take the longest time. The inset in Figure 5.2 shows the transition depending on the shear rate for one selected system, where the transition depends on the wall velocity. The fastest transition is observed for the fastest driving ($v = 0.2$).

Analog to the transition of the end-to-end vector, the normalized shear stress shown in Figure 5.3 exhibits the same pathway towards steady state. Interestingly, during the evolution, σ_{xz} does not reach steady state first, but overshoots slightly, when the systems are driving fast enough. Moreover, for larger chains ($N = 60$, $N = 120$) the normalized shear stress oscillates ones after the overshoot and then becomes unity. That behavior is not observed in chain specific observables and therefore this effect may be attributed to the solvent.

Since all control parameters, including the critical shear rate, are known, a rescaling of the time series is performed. First, the evolution of the end-to-end vector of Figure 5.2 is rescaled, as shown in Figure 5.4. For a short time all $R_{\text{ee},x}(t)$ match perfectly on the master curve [Eq. (5.4)] until they crossover to steady state. For the different driving strengths, all end-to-end vectors superimpose (inset Figure 5.4), except for the smallest wall velocity, where Eq. (5.4) is not valid. They match nicely the master curve before they branch to unity.

Complementary, the rescaling of times for the shear stress in Figure 5.5 yields for a short period a master curve, whereas the overshoots become more separated. Interestingly, for different wall velocities all shear stresses superimpose, which seems to be a coincidence (inset in Figure 5.5).
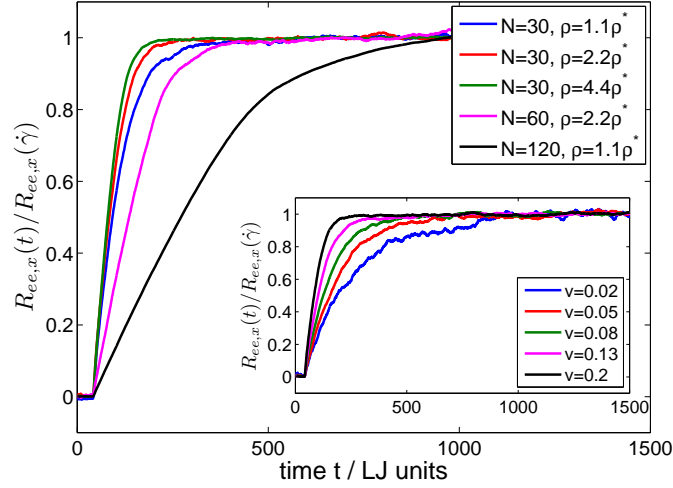
Figure 5.2: Normalized end-to-end vector of the brushes for selected systems at constant wall distance $D_z = 17.5$, different grafting densities, and chain lengths for the wall velocity $v = 0.2$. The inset shows for one system with $\rho = 2.2\rho^*$ and $N = 30$ the transition to different velocities.
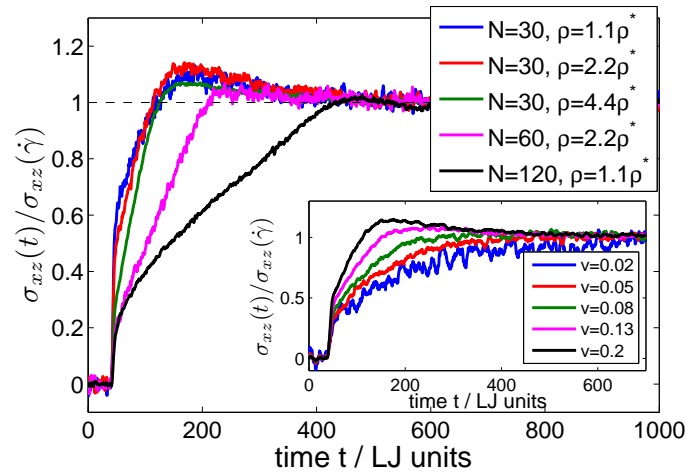
Figure 5.3: Normalized shear stress of the fluid for selected systems at constant wall distance $D_z = 17.5$, different grafting densities, and chain lengths for the wall velocity $v = 0.2$. The inset shows for one system with $\rho = 2.2\rho^*$ and $N = 30$ the transition to different wall velocities. For large wall velocities the shear stress exhibits an overshoot.
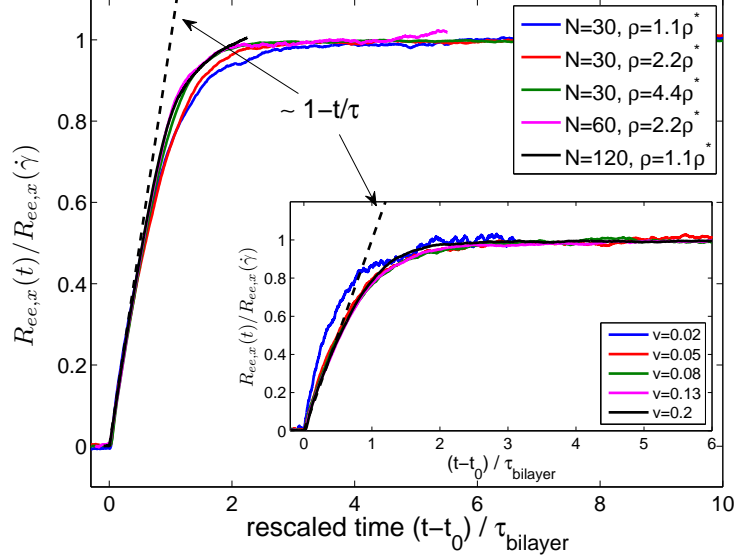
Figure 5.4: Normalized end-to-end vector of the brushes for selected systems at constant wall distance $D_z = 17.5$, different grafting densities, and chain lengths for the wall velocity $v = 0.2$. The inset shows for one system with $\rho = 2.2\rho^*$ and $N = 30$ the transition to different velocities. For both plots the evolution time is rescaled by the intrinsic transition time τ. A master curve [Eq. 5.4] is indicated by the dashed line in both plots.
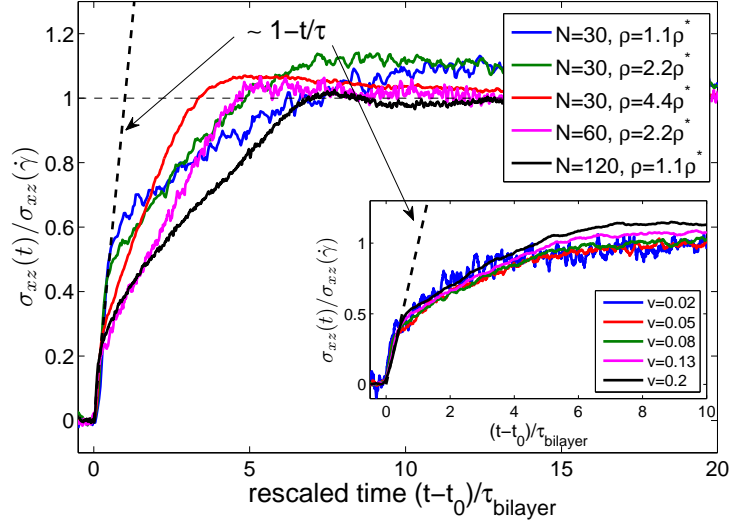
Figure 5.5: Normalized shear stress of the fluid for selected systems at constant wall distance $D_z = 17.5$, different grafting densities, and chain lengths for the wall velocity $v = 0.2$. The inset shows for one system with $\rho = 2.2\rho^*$ and $N = 30$ the transition to different wall velocities. For large wall velocities the shear stress exhibits an overshoot. While the shear stress of different systems match the master curve [Eq. 5.4], the overshoots are separated.

5.2.1 Velocity profile

To analyze how the non-stationary shear effects the fluid during the onset of motion, the layer resolved velocity profile is examined. While the walls are set in motion the fluid (the fluid includes both ingredients) remains still for a very short time. After that short time the drag of the walls is transmitted to the chains attached to each wall inducing the current velocities of the walls. Since the chains are not infinitely stiff and exhibit inertia, the shear profile propagates slowly into the system. Figure 5.6 shows several snapshots of the velocity profile in time (t_i). When the walls almost reached their designated velocities (t_1), a few layers above the substrate are set in motion, while the liquid in the middle of the gap remains still. At t_3 the momentum is distributed such that for a small time a linear velocity profile is observed. Then the velocity crosses over to the steady state velocity profile as discussed in section 4.6. Each snapshot in time is connected to an additional plot (inset), where the shear stress as a function of the strain $\gamma(t)$ is shown. After a ballistic behavior $[\sigma_{xz}(t) \sim \gamma^2(t)]$, related to the acceleration of the wall and a rapid propagation of momentum into the system, the shear stress grows sublinearly with the displacement $[\sigma_{xz} \sim \gamma^{1/2}]$ indicating viscoelastic behavior [71]. Interestingly, the stress grows further, even when the steady state profile is already established (t_5).
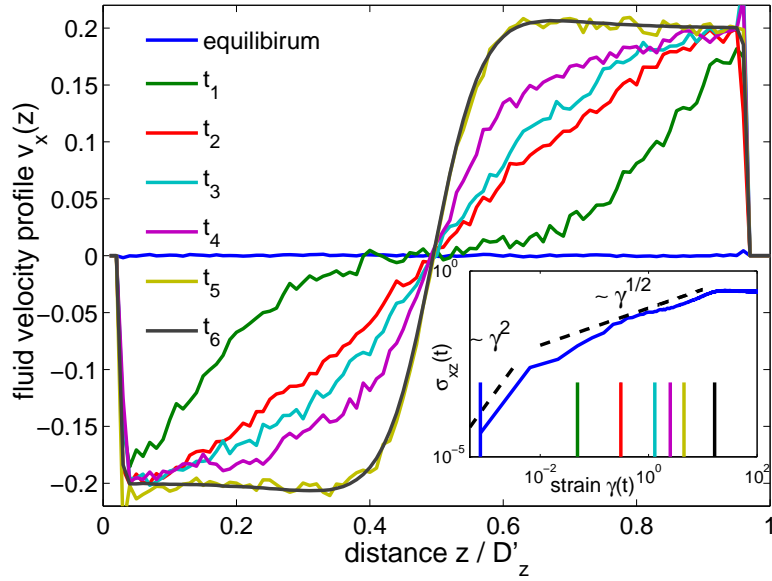
Figure 5.6: A series of fluid velocity profiles (sum of both components) in time. At t_0 the fluid is at rest, while at t_5 the profile reaches its steady state. In between the wall velocities propagate into the system. The inset shows the growth of the shear stress as a function of the strain. For a small strain growth the shear stress increase superlinearly $\sigma_{xz} \sim \gamma^2$, with significant wall displacement the stress grows sublinearly, $\sigma_{xz} \sim \gamma^{1/2}$. The parameters for the chosen system are $N = 30$, $\rho_{\mathrm{g}} = 4.4\rho_{\mathrm{g}}^*$, and $D_z = 17.5$.

5.3   Inversion of motion

In this section the second part of the wall protocol (Figure 5.1) is followed. The surface transits continuously from $v_0 = -v_0$ in a very short time $\tau_{\mathrm{inv}} = 2500\Delta t$.
For the lateral chain extension, now given by the radius of gyration [Eq. 3.2], undergoes a minimum during the inversion as shown in Figure 5.7. The inversion is shown for two different chain lengths, two grafting densities, and three wall velocities. The short chains ($N = 30$) transit the fastest, moreover, for small velocities the transition takes longer than for larger velocities. With rescaling the time, see Figure 5.8, all time series superimpose for a short time on a master curve, except for the short chains with the slowest wall velocities ($v = 0.02$). In this case Eq. (5.4) is expected to fail. The lateral extensions crossover to minima, which are not aligning. Secondary processes like diffusion are now dominating. At some point the driving dominates again and the normalized radius of gyration returns to steady state.
The same observation can be made for the corresponding shear stresses. Similar to Figure 5.7 in Figure 5.9 the shear stresses of those systems are shown. In Figure 5.9 all shear stresses superimpose on a master curve when the time is rescaled. For larger times the stress crosses over to unity. For the shortest chains and smallest velocity, the scaling fails as expected for the radius of gyration, (Figure 5.8). For this particular wall velocity ($v = 0.02$) the system ($N = 30$, $\rho = 4.4\rho^*$, $D_z = 17.5$) responses linearly, therefore, Eq. (5.4) must fail.
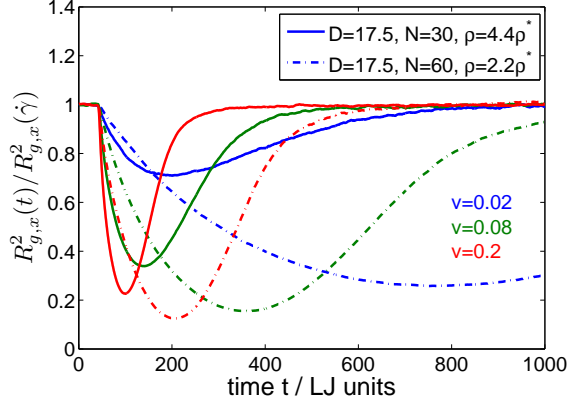
Figure 5.7: For two selected systems with explicit solvent molecules the evolution of the normalized radius of gyration in shear direction is shown for three different wall velocities. Depending on their molecular parameters, they reach steady state at different times.

Figure 5.8: The normalized radius of gyration vs. rescaled time. All time series follow a master curve [Eq. (5.4)] (black line) and leave it at some point, reaching a minimum and returning to steady state.

Figure 5.9: The shear stress of the same two systems as in Figure 5.7 is shown.
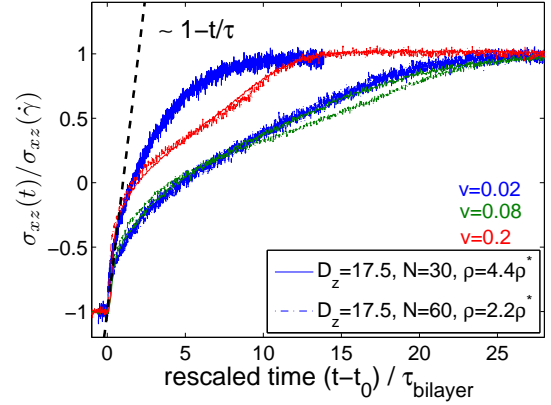
Figure 5.10: When rescaling the time the shear stress follows for short times a master curve leaving it at some point crossing at different times over to steady state.

5.4 Normal force response
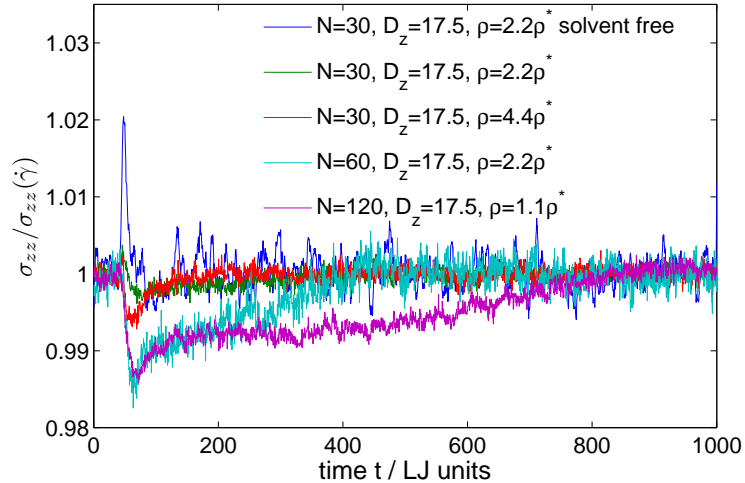
Figure 5.11: Normal stress response during inversion for solvent and solvent-free systems. All presented systems respond non-linearly in steady state ($Wi \gg 1$). All systems without solvent show a rapid increase of the normal force in this regime, whereas for more dilute systems ($Wi \ll 1$) the response vanishes (not shown). On the other hand, the complementary systems with solvent indicate a small overshoot at the beginning of the inversion, but turn rapidly into decrease of pressure passing a minimum and returning to steady state. The time to return back to steady state depends only on the brush parameters, neither on the inversion time nor the wall velocity.

During the non-stationary shear the response of the fluid perpendicular to the wall shows a response as well. Systematic studies distinguish between systems with and without solvent. Generally, systems without solvent show a small and rapid overshoot in the normal stress. The normal pressure jump decays very quickly in time. For systems that respond linearly in steady state the positive response vanishes. On the other hand, the normal component drops for systems with solvent during the inversion. First, for a short period of time the systems respond similarly to the complementary systems without solvent with a small increase in normal pressure. The normal pressure drops rapidly below the steady state value passing a minimum and returning back to its steady state value. The minimum pressure value of each response stays above the equilibrium pressure. When the turn time τ_{inv} is decreased, the overshoot grows slightly and vice versa vanishes with increasing

τ_{inv}. The decay time depends only on the brush parameters, N and ρ_{g}, not on the shear rate and therefore a rescaling as proposed in section 5.1 does not give satisfying results. The presence of the explicit solvent molecules compensates the rapid jump of the normal pressure. The pressure drop increases for larger chain length, e.g. $N = 60$ compared to $N = 30$. For the longest simulated chain length $N = 120$ the normal pressure does not decrease anymore.

The effect of pressure reduction must therefore increase if solvent molecules with larger inertia are used. In the next section the velocity and flow profiles are discussed, where local rearrangements take place.

5.5 Velocity and flow profile during inversion
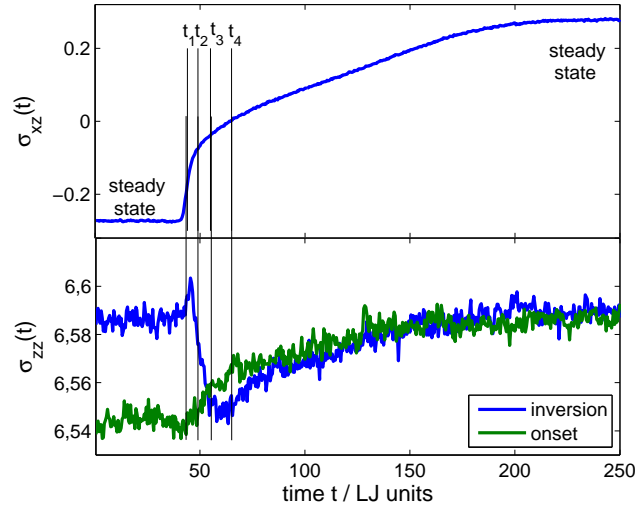
Figure 5.12: Both stress components during the inversion of motion. The upper plot shows the shear stress transiting from the negative steady state value to its positive value via a rapid jump from $-\sigma_{xz}(\dot{\gamma})$ to zero and slowly crosses over to $\sigma_{xz}(\dot{\gamma})$. In the lower plot the normal stress components are shown during the inversion (blue line) and the onset (green line) of motion. During the inversion a slight overshoot is observed, which quickly drops almost to its equilibrium value, shown by the onset of motion. The lines at t_i $(i = 1, \ldots, 4)$ connect the stress responses in time with the velocity and flow profiles in Figure 5.13.

Similar to the observation of the velocity profile during the onset of motion, the flow of the fluid is analyzed during the inversion. While the velocity profile is ob-

served layer resolved perpendicular to the walls, the flow profile is observed parallel to the plates along the shear (x) and gradient (z) directions. In Figure 5.12 the stress components are shown for a system with $N = 30$, $\rho_g = 4.4\rho_g$, and $D_z = 17.5$. The parallel lines are connecting the stresses with the velocity profiles of the components and flow profiles of the solvent in Figure 5.13.

Before the inversion the velocity profiles of both components are in steady state, see Figure 5.13(a), as discussed in section 4.6. The flow profile, lower plot in Figure 5.13(a), exhibits small vortices in the middle of the gap indicating a rotational motion of the solvent. During the inversion at time t_2, when both walls pass zero velocity (Figure 5.13(b)), the particles in the middle of the interface maintain their flow, while the monomers close to the walls stick to the wall velocity. At that point strong reorientations occur in the flow, the solvent molecules establish micro-turbulences with no specific direction of rotation (vorticity). The walls continue to drag the chains at t_3, Figure 5.13(c), pushing the turbulences into the middle and orient the flow again. At time t_4, Figure 5.13(d), when a linear velocity profile is established along the whole gap, the turbulences died out except for those in the middle, the vortices switched their rotational direction.

The normal stress response is directly connected to the occurrence of the micro-turbulences. In steady state the normal pressure is slightly larger than at equilibrium, due to extra kinetic contributions to the stress tensor. When the driving stops during the inversion, the additional kinetic contributions carried by the solvent particles is dissipated into heat and transported out of the system by the thermostat.

66

(a) t_1

(b) t_2

(c) t_3

(d) t_4
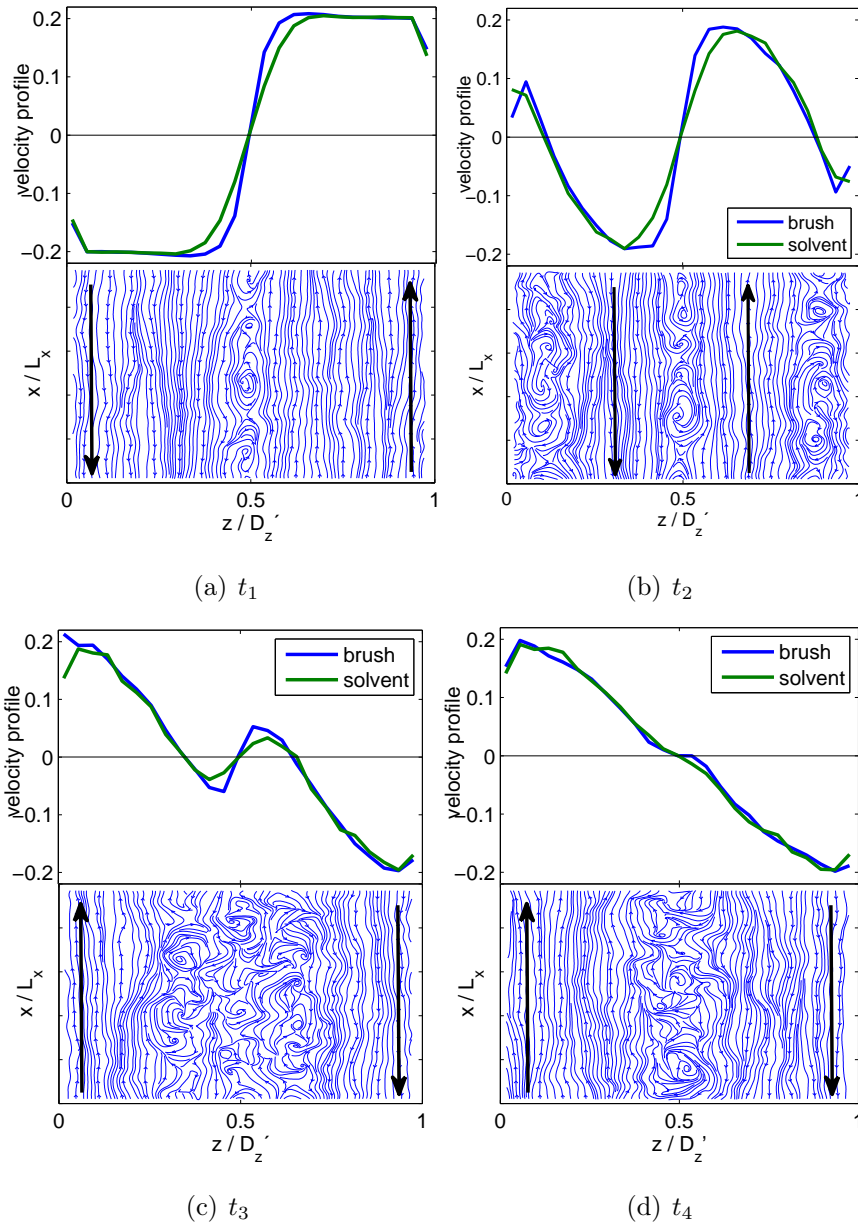
Figure 5.13: A series of snap shots of velocity (upper subplots) and flow profiles (lower subplots) are show, each one corresponds to a certain time t_i in Figure 5.12. (a) Upper plot: Steady state velocity profiles, (a) Lower plot: the solvent flow profile with circulating flow in the middle of the gap. During the inversion the velocity profile follows the wall movement with a slight delay [(b) upper plot], where at the walls micro-turbulences occur propagating into the middle, see (b) and (c), lower plots. When a linear shear profile is established again [(d) upper plot], the turbulences die out, the normal pressure passed its minimum and the shear stress grows towards its steady state value, Figure 5.12

.

5.6 Summary

This chapter discussed the transition from equilibrium to steady state, the onset of motion. Additionally, the transition when the wall movement is inverted smoothly from v_0 to $-v_0$ and faster than the relaxation time of the bilayer $\tau_{\text{imv}} \ll \tau_{\text{bilayer}}$, was introduced. A scaling relation for the lateral chain extension was derived, where the transition time for each system is shear rate dependent. The scaling approach is only valid for systems which respond non-linearly to shear, e.g. $Wi \gg 1$. For each system such a τ_{bilayer} could be found, such that the evolution of microscopic and macroscopic observables are superimposed for short times.

Furthermore, a normal pressure response was observed. During the transition systems with and without explicit solvent exhibit for short times an overshoot in the normal pressure. A shock wave travelling through the system during that time may be the origin of that effect. The overshoot vanishes when the inversion time becomes broader. On the other hand, the fluid may become unstable if the transition time becomes delta-like, increasing the overshoot in normal pressure. While the solvent-free case immediately drops back to its steady state value, the system with dimers reveal a pressure decrease going back to the equilibrium pressure and rising to the steady state value again. The decrease in pressure is linked to the solvent flow, where during the inversion the solvent particles exhibit fast reorientations. In this turbulent behavior local kinetic contributions to the stress tensor cancel, therefore, the overall pressure must decrease until the system is reorganized and transits back to steady state. The extra inertia of the added matter influences strongly the non-stationary response.

Chapter 6

Two opposing brushes in the oscillatory regime

This chapter will discuss the fluid response to a sinusoidal perturbation, where strain is imposed and the stress monitored to determine the rheological properties of the material, e.g. the dynamic shear modulus. Additionally, microscopic observables will be monitored. Not much is known about the dynamics during an oscillatory experiment of polymer brushes, but it is essential to understand how the complex fluid behaves. SFA experiments set certain geometrical limits, e.g. finite substrate size, compression and sensitivity to force responses. The first section will introduce the parameters used in the simulations, perturbation amplitudes, and frequencies. The second section will discuss the viscoelastic properties and, to some extent, the linear response approximation in terms of the perturbation strength. Generally, systems with explicit solvent (dimers) at large Weissenberg numbers ($Wi \gg 1$) are considered, because they exhibit a better signal-to-noise ratio experienced in the previous studies. Utilizing standard rheology like analysis will reveal a characteristic relaxation time which is related to microscopic and macroscopic responses. A comprehensive overview about the rheology of non-Newtonian liquids is given in the book of Ferry [71].

6.1   Sinusoidal wall protocol

In our simulations we apply a sinusoidal shear protocol

$$v(\omega, t) = v_0 \cos \omega t \; , \tag{6.1}$$
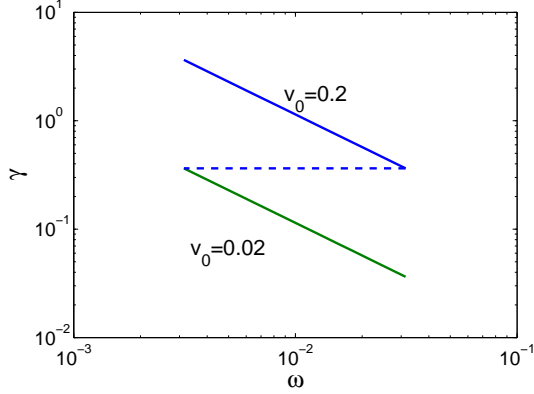
Figure 6.1: Strain as a function of frequency. The solid lines define the parameter space in terms of the wall velocity. The dashed line represents the strain being independent of ω.
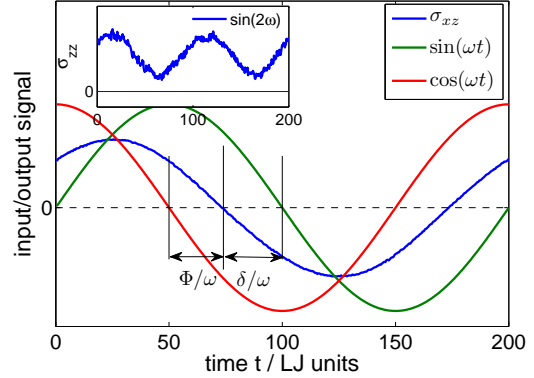
Figure 6.2: Phase of the output signal shear stress (blue) compared to the input signal wall displacement (green) and wall velocity (red). The inset shows the normal stress component oscillating above the equilibrium value with 2ω.

with the amplitude of the wall velocity v_0 and a fixed frequency ω to both substrates. In this situation, the strain becomes a function of ω

$$\gamma(\omega) = \int_0^{\frac{\pi}{4}} \dot{\gamma} dt = \int_0^{\frac{\pi}{4}} \frac{v_0}{D_z} \cos(\omega t) dt = \frac{v_0}{D_z \omega} \ . \tag{6.2}$$

Complementary, in the experiment often the strain amplitude γ_0 is fixed and defined via

$$\gamma = \frac{\Delta x}{D_z} \ , \tag{6.3}$$

with Δx being the wall displacement. We now apply the harmonic driving, where γ becomes time-dependent

$$\gamma(t) = \gamma_0 \sin(\omega t) \tag{6.4}$$

with a frequency dependent shear rate

$$\dot{\gamma}(t) = \gamma_0 \omega \cos(\omega t) \ . \tag{6.5}$$

In Figure 6.1 expressions (6.2) and (6.5) are shown: for two examples the wall velocity is fixed (solid lines) and for one example an arbitrarily constant wall displacement is chosen, where the velocity becomes a function of the frequency (dashed line). As discussed in chapter 2 the wall velocity can only cover one order of magnitude of velocities without heating up the fluid too much and that limits the explorable

frequency space for a fixed γ_0. The problem of a constant strain is not further investigated.

6.2 Viscoelastic observables

Viscoelasticity is studied using dynamic mechanical analysis. For Newtonian fluids the shear stress σ_{xz} is in phase with the shear rate $\dot{\gamma}$, so the response of one caused by the other is immediate, and there are no normal stress responses. For our polymer brushes a representative example how the considered stress components evolve in time is shown in Figure 6.2. The shear stress oscillates with the frequency ω (blue solid line), but it is not in phase with neither the shear strain (green solid line), nor the shear rate (red solid line). The inset in Figure 6.2 shows the normal stress response oscillating with twice the frequency 2ω around a above the equilibrium pressure. For the shear stress one can measure the amplitude and phase shift as a function of the frequency ω. If we assume that the strain amplitude γ_0 is sufficiently small so that the shear stress is linear in strain, one can write [71]

$$\sigma_{xz} = -A(\omega)\gamma_0 \sin(\omega t + \delta) - B(\omega)\dot{\gamma}_0 \cos(\omega t - \phi) \ . \tag{6.6}$$

The shear stress now can be identified as a superposition of in-phase and out-of-phase components. The amplitudes are equivalent to two linear viscoelastic material functions, G' and G'':

$$\sigma_{xz} = -\gamma_0 \left[G'(\omega) \sin(\omega t) + G''(\omega) \cos(\omega t) \right] \ , \tag{6.7}$$

where G' and G'' add together to the complex shear modulus

$$A(\omega) = \sqrt{G'^2 + G''^2} = |G^*| \ . \tag{6.8}$$

The amplitude $B(\omega)$ and the phase shift ϕ in Eq. (6.6) are related to the complex viscosity, η' and η'' by

$$B(\omega) = \sqrt{\eta'^2 + \eta''^2} = |\eta^*| \ . \tag{6.9}$$

The * imply the complex functions including real and imaginary parts. When real and imaginary parts of either the complex shear modulus or the complex viscosity are known, the phase shifts can be calculated via

$$\tan \delta = G''/G' \quad \text{and} \tag{6.10}$$

$$\tan \Phi = \eta''/\eta' \ . \tag{6.11}$$

The phase angle δ between strain and shear stress is normally defined by the loss tangent, $\tan \delta$. The phase angle ϕ between shear rate and shear stress is then found as $\phi = \pi/2 - \delta$.

6.2.1 Complex shear modulus and complex viscosity

The complex shear modulus determining the shear stress that is linear in strain is a linear viscoelastic property. Such observables are important to characterize the material's behavior under small strain deformation. $G' = \eta'' \omega$ is called the storage modulus and gives information about the elastic character of the fluid or the energy storage taking place during the deformation.

On the other hand, $G'' = \eta' \omega$ is known as the loss modulus and tells about the viscous character of the fluid, or the energy dissipation that occurs in flow.

In the situation of an ideal fluid the shear modulus G' reacts like a perfectly elastic solid, $G' = G$ and $G'' = 0$, whereas for Newtonian fluids, η' is equal to the viscosity η, and η'' is zero.

Oscillatory shear and dielectric relaxation are often described and discussed in the same context due to the similar structure of the underlying equations [79]. A link can be established between the electromagnetic and rheological susceptibility. Non-linear responses are well known for the electromagnetic case, much higher optical frequencies may occur with increasing optical intensity [80].

6.2.2 Non-linear response

With decreasing frequency the strain grows, see Eq. (6.2), the response may become non-linear [79]. To quantify the non-linearity the power spectral density (PSD) is used. With the help of Fourier analysis higher frequency components can be identified hidden inside the original signal. The PSD is defined as

$$S(\tilde{\omega}) = \widetilde{X}(\tilde{\omega}) \times \widetilde{X}^*(\tilde{\omega}) \, , \tag{6.12}$$

where $\widetilde{X}(\tilde{\omega})$ represents the Fourier transformed time-dependent observable, e.g. $\sigma_{xy}(t)$, and $\widetilde{X}^*(\tilde{\omega})$ its complex conjugated. $\tilde{\omega}$ is given by the numbers of observation time steps. The signal must contain at least one frequency, the fundamental driving frequency ω of the walls. Depending on the strength of the driving, higher harmonic

frequencies may appear

$$\omega_n = n\omega \quad \text{with} \quad n = 2, 3, \ldots \tag{6.13}$$

Since the stress response depends on the strain applied to the system deforming the material, the linear response assumption may not hold. The stress can be expressed as a sum of higher Taylor polynomials

$$\frac{\sigma_{xz}}{\gamma_0} = \sum_k G'(\omega_k) \sin(k\omega_k t) + G''(\omega_k) \cos(k\omega_k t) \tag{6.14}$$

with $k = 1, 3, 5 \ldots$ being the number of higher frequencies and there related amplitudes $G'(\omega_k)$ and $G''(\omega_k)$. Two examples of Fourier transformed response signals are shown in Figure 6.3 for the highest and smallest external driving frequencies applied to our polymer brushes. While for $\omega \gg \omega_1$ (inset) only one frequency peak appears in the PSD, the situation changes for the smallest frequency, where higher odd harmonics $k\omega$ for $k = 1, 3, 5, 7$ are hidden in the stress' PSD. Only odd harmonics appear which is given by the fact that for one, the viscosity is described by a power-law and independent of the shear direction $\eta(\dot{\gamma}) = \eta(-\dot{\gamma}) = \eta(|\dot{\gamma}|)$, section 4.4, and for small shear rates η can be expanded in terms of the absolute shear rate

$$\eta = \eta_0 + a|\dot{\gamma}| + b|\dot{\gamma}^2| + \ldots \ . \tag{6.15}$$

Secondly, the Fourier analysis allows to express the time dependence of $\dot{\gamma}$ as a sum of higher even harmonic contributions

$$|\dot{\gamma}| \propto a + b\cos(2\omega_1 t) + c\cos(4\omega_1 t) \ldots \ , \tag{6.16}$$

which in the case of oscillatory driving with one odd harmonic leads to a mixture of higher even harmonics [Eq. (6.16)] and therefore via the trigonometric addition theorems the multiplication of Eq. (6.16) with Eq. (6.15) results exclusively in a sum of odd harmonics. To estimate the influence of the higher frequencies the amplitude can be calculated from the PSD, as well. In general, for all recorded signals, the third amplitude at 3ω for each shear modulus component is less than 10% of the driving one [$S(\omega)$] and therefore negligible. The linear response assumption holds in terms of the strain. In the work of Chen, see Ref. [81], the PSD of the response for sheared zwitterionic brushes is published, which reveals higher harmonics indicating a strong non-linear response with respect to the displacement.
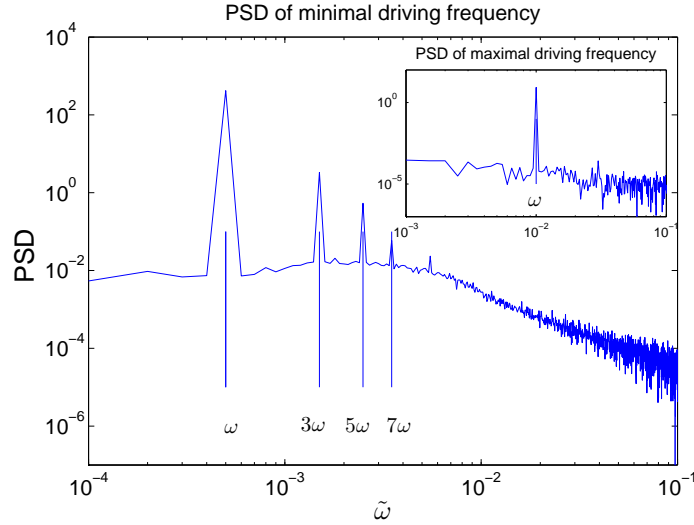
Figure 6.3: Power spectral density of the smallest and (inset) largest frequency driven stress response.

6.3 Viscoelastic response

In the last section the non-linear response was discussed and a Fourier analysis indicated that linear response analysis holds, since higher harmonics are negligible. Figure 6.4 shows the first Fourier amplitudes as a function of the frequency for one system with a chain length of $N = 60$, grafting density $\rho = 2.2\rho^*$, and $D_z = 17.5$. One may distinguish three main regions. In the terminal region for small frequencies G'' is linear in frequency and $G' \propto \omega^2$. When those properties are extrapolated to higher frequencies, thus intersect at some point defining a resonance frequency ω_0 of the fluid [82]. Beyond ω_0 both components cross-over to the plateau regime, where the shear modulus is almost independent of the frequency expressing nearly elastic behavior, like two sliding solids. Usually, in this regime the loss modulus is larger than its elastic counterpart. The chains cannot fully relax and this contributes to the pseudo-elastic response at intermediate frequencies [83]. The regime $\omega \gg \omega_0$ is referred to as the plateau regime, where the shear moduli transit via a power-law to the glassy regime [71, 82]. In Figure 6.4 a function $G \sim \omega^{0.75}$ is added as a guide to the eye. Several experiments studied polymer solutions [71] close to the glassy regime and they report about an intersection of both viscoelastic components, which is not explored here. The strain is already so small that the motion of the walls is of the order of the monomer size, see inset in Figure 6.4.
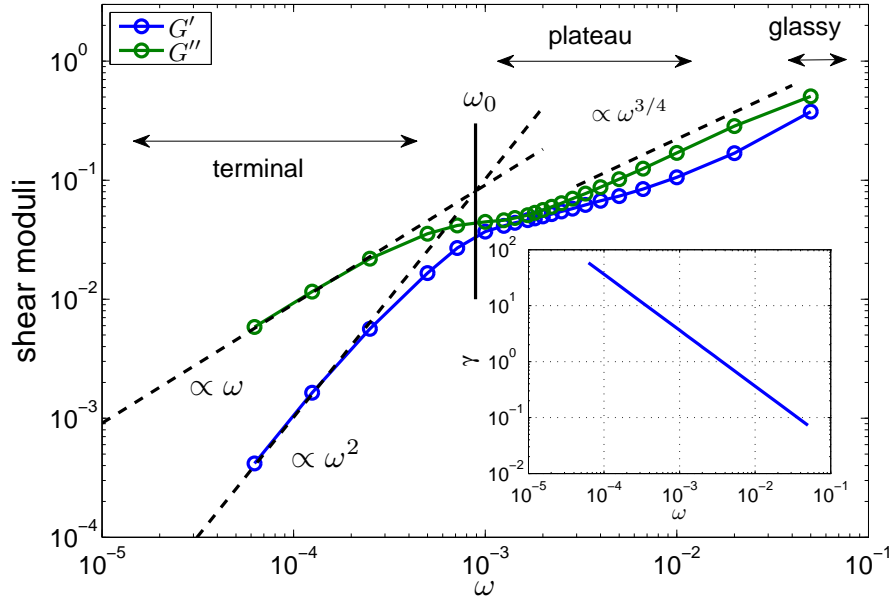
Figure 6.4: The shear moduli as a function of ω. The linear extrapolations in the terminal regime (black dashed lines) intersect and define a resonance frequency (solid black line). The complex shear modulus grows beyond the plateau regime with a power-law $\omega^{0.75}$ (dashed line) towards the glassy regime. The inset shows the strain γ as a function of ω.

In Figure 6.5 the control parameters are changed in order to study the effect of compression, various brush parameters, and the Weissenberg number. Under high compression a clear plateau regime appears, compare Figure 6.4 with 6.5(a). When the brushes become more diluted, see Figure 6.5(b) and 6.5(c), the explicit solvent dominates the fluid response and recovers the Newtonian fluid properties, as indicated by the black dashed line in Figure 6.5(c). One system is tested in the linear response regime in terms of the Weissenberg number, see Figure 6.5(d). In this case, the brushes are able to relax for all strains. Whereas for $Wi \gg 1$ the loss modulus is always larger than the storage modulus, for $Wi \ll 1$ in the plateau regime G' exceeds G''. All systems maintain in both frequency limits with its observed power-laws as seen in Figure 6.4. The complex shear modulus is transformed into its time-domain transient counterpart, the relaxation modulus, via a fast Fourier transform (FFT), $G(\omega) \overset{\text{FFT}}{\to} G(t)$, [performed with MATLAB (2009a, The MathWorks)]. When a sequence of small step-strain deformations is considered the superposition of shear

(a) $D_z = 12$, $\rho = 4.4\rho^*$, $N = 30$

(b) $D_z = 23$, $\rho = 4.4\rho^*$, $N = 30$

(c) $D_z = 17.5$, $\rho = 1.1\rho^*$, $N = 30$

(d) $D_z = 17.5$, $\rho = 4.4\rho^*$, $N = 30$, $Wi \ll 1$
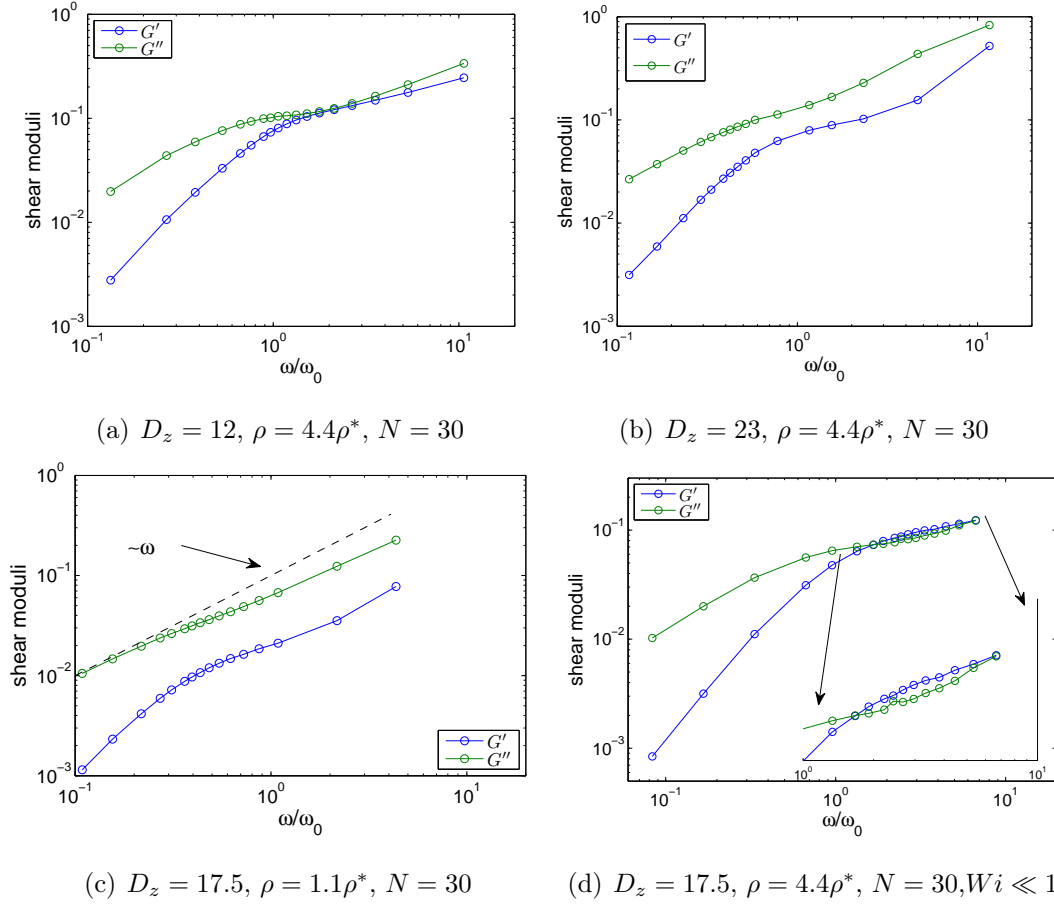
Figure 6.5: Four log-log plots show the complex shear moduli for different parameter combinations, as indicated in the captions. In general, all shear moduli maintain for high and small frequencies the same properties as discussed in Figure 6.4.

Figure 6.5(a): The system is strongly compressed and at intermediate frequencies a smaller pseudo-solid regime is observed than in Figure 6.4

Figure 6.5(b): The wall distance is larger while the brushes still slightly interpenetrate, but both shear moduli are further seperated.

A similar observation is made in Figure 6.5(c), where the brushes are more dilute, the response is dominated by the explicit solvent where G'' is one order of magnitude smaller than G'. The polymeric time scales, which are susceptible to the harmonic driving, deviate from the ideal curve (black dashed line). With diluting the system the properties of a Newtonian fluid are recovered.

In Figure 6.5(d) the response changes. At intermediate times the real part of the shear modulus becomes larger than the imaginary part, usually the opposite is observed. For small Weissenberg numbers the brushes are able to relax since the driving is small almost preserving the equilibrium overlap width. The intersection point is sometimes taken as resonance frequency, but ω_0 determined by extrapolations of the small frequency limit is of the same order.
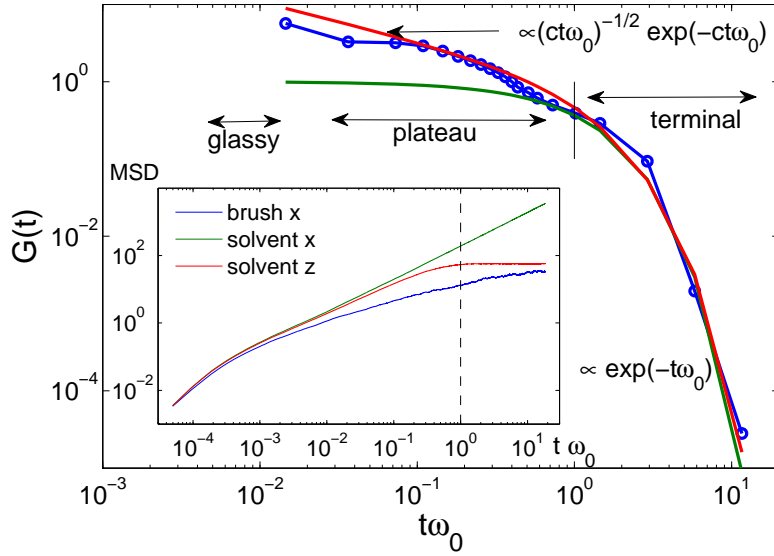
Figure 6.6: The stress relaxation in time, after the relaxation time $1/\omega_0$ the stress relaxes exponentially. The green line represents a simple Maxwell fluid element, while the red line represent the Rouse approximation [61]. The parameter c is close to unity. Before the stress relaxes it remains almost constant, for very short times in the glassy region a jump may occur [82]. The inset shows the mean square displacement for that system at equilibrium as a function of $\omega_0 t$. The brushes are not yet relaxed in terms of the MSD, but the stress has reached its fluid behavior.

responses (Boltzmann Superposition Principle) in a continuous function is given by

$$\sigma_{xz}(t) = \int_{-\infty}^{t} G(t - t')\dot{\gamma}(t')dt' , \qquad (6.17)$$

where $G(t - t')$ represents the shear relaxation modulus, which depends on the past. The derivative defines the memory function [82]

$$m(t) = -\frac{dG}{dt} . \qquad (6.18)$$

Figure 6.6 displays the relaxation modulus for the acquired data in Figure 6.4. If the fluid can be described as a Maxwell fluid by the superposition of one purely elastic and one purely viscous element, $G(t)$ for $t \ll 2\pi/\omega_0$ would follow the green line where a single relaxation time dominates the response, $\tau_0 = 2\pi/\omega_0$, such that

$$G(t) = g_0 \exp(-t/\tau_0) . \qquad (6.19)$$

There, g_0 represents the relaxation modulus for a simple Maxwell element. Since $G(t) \neq g_0$ for $t \ll 1/\omega_0$ the single Maxwell element does not describe the fluid.

As a first approximation the observed stress relaxation modulus is fitted with the Rouse model [61]

$$G(t) = (ct\omega_0)^{-\frac{1}{2}} \exp(-ct\omega_0) \, , \qquad (6.20)$$

where c is a free parameter. Equation (6.20) is added to Figure 6.6 (red line), which works surprisingly well. A second fit given by Zimm dynamics corrects the Eq. (6.20) by a slightly different power law [61]

$$G(t) = (ct\omega_0)^{-\frac{1}{3\nu}} \exp(-ct\omega_0) \, . \qquad (6.21)$$

Much more data points need to be acquired in frequency space to gain better statistics in the time domain and therefore better distinguishable fits. The response be-
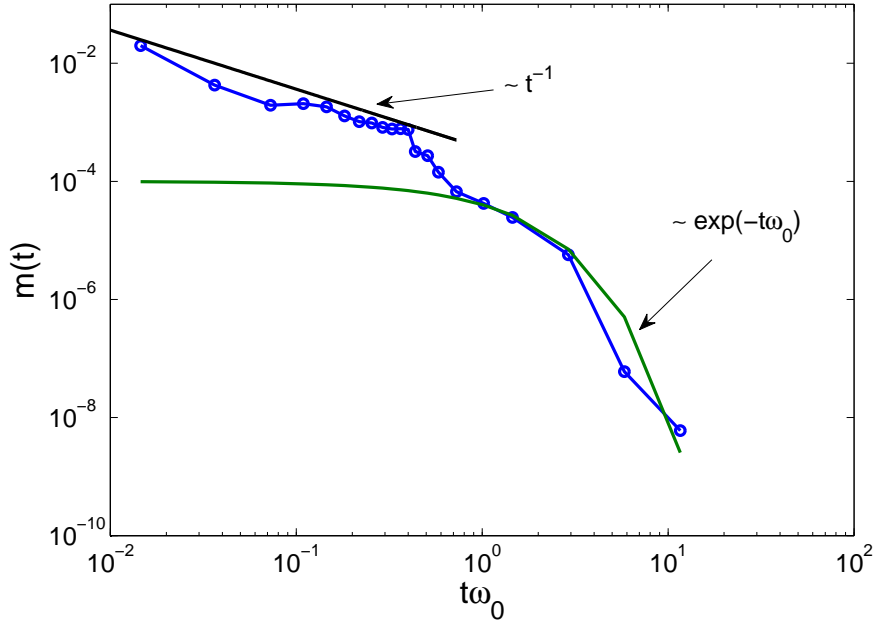
Figure 6.7: A double logarithmic plot of the memory function given by Eq. (6.18). Since the relaxation modulus in Figure 6.6 decays exponentially, that property is maintained given by the exponential fit (green line). For short times a long time behavior is exhibited. The power law indicated with the black solid line is added a guide to the eye.

comes liquid-like at large times with a fading memory, which decays exponentially, as indicated by the green line. The inset shows the MSD of the two ingredients inside the system, one brush displacement component (x-direction) and two solvent components (x- and z-direction). Recalling from section 3.3.1 the brushes' MSD

saturates at large time while the solvent shows free diffusive behavior in the lateral (x) direction. After the transition from the ballistic regime a subdiffusive behavior is observed supporting the observation that the relaxation modulus cannot completely decay. However, when the relaxation modulus enters the terminal region, the MSD has not yet reached its final plateau.

The memory function displays similar properties as the stress relaxation modulus, see Figure 6.3. At short times a rather slow decay with a power law behavior is observed. A power-law is added to the plot as a guide to the eye. Since the stress relaxation modulus and the memory function for short times are not represented by one fluid specific relaxation time τ_0, other approaches are needed to model the observed deformation history. For further reference the book of Ferry [71] provides a comprehensive starting point.

Furthermore, the viscous character of that system is determined by dividing the shear moduli by the frequency, shown in Figure 6.8. The real part η' exhibits a frequency independent plateau for small frequencies and is decreasing continuously towards higher frequencies. The linear response theory identifies the plateau value as the zero shear viscosity. As shown in section 3, $\eta(0)$ is determined by scaling the dynamic viscosity onto a power law. In the harmonically driven system the zero shear viscosity in linear response is measurable when $\omega \to 0$, the storage modulus related viscosity yields

$$\lim_{\omega \to 0} \eta'(\omega) = \eta(0) \ . \tag{6.22}$$

The linear response analysis holds for decomposing the stress signal but not for the response in terms of the Weissenberg number Wi. For the designated set of parameters ($N = 60$, $\rho = 2.2\rho^*$, $D_z = 17.5$, $Wi \gg 1$) the steady state viscosity is found on the non-Newtonian branch, therefore the real part becomes

$$\lim_{\omega \to 0} \eta'(\omega) = \eta(\dot{\gamma}) \ . \tag{6.23}$$

The imaginary part of the complex viscosity exhibits a maximum around the resonance frequency ω_0, determined from the extrapolation of both shear moduli. If the explored terminal regime does not allow an extrapolation of the shear moduli to extract the resonance frequency the observed maximum in η'' can be used, too.
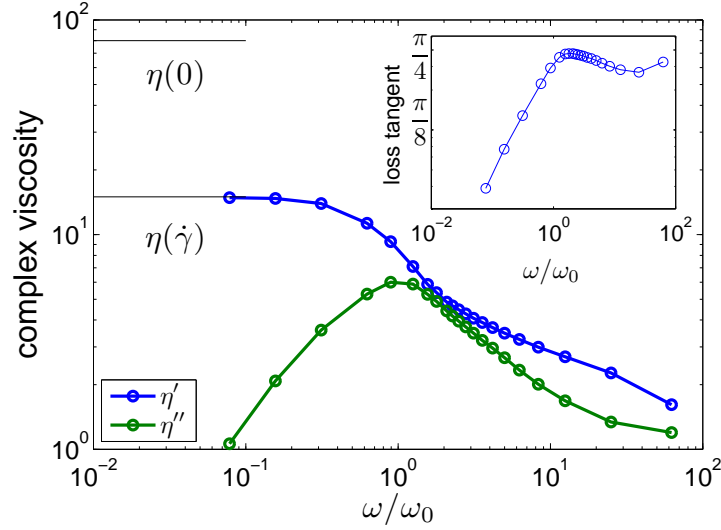
Figure 6.8: The complex viscosity as a function of the normalized frequency. In the limit of $\omega \to 0$ the real part of the viscosity does not reach the zero shear viscosity, but the steady state viscosity in the power-law region, discussed in section 4.4. The inset shows the loss tangent with its maximum around the resonance frequency.

6.3.1 Steady state limit

The response depends on the strain leading usually to a non-linear behavior inducing higher odd harmonics to the shear stress changing the shape from a simple sinusoidal curve to a superposition of sinus functions, similar to Eq. (6.14). In Figure 6.9 the shear stress is plotted versus the wall displacement Δx. A system is chosen where linear and non-linear shear force responses are observable depending on Wi. For both cases, when $\omega \gg \omega_0$, the stress follows an ellipsoidal shaped curve where the major axis is inclined (phase δ). With decreasing frequency below the resonance frequency and growing strain the ellipsoid becomes stretched turning slowly into trapezoidal shaped curve where the stress becomes constant implying that the shear stress saturates while the strain increases further. Analogous to the oscillatory driven systems, where the wall velocity changes smoothly and continuously in a sinusodial fashion, the inversion of motion in the last chapter may also be seen as a cyclic movement but with almost zero turn times creating a triangular shaped wall movement in time. In that case the frequency and the frequency-independent strain are large. In the literature the expression "large amplitude oscillatory shear" (LAOS) is generally used [84]. For $Wi \ll 1$, Figure 6.9(a), and for $Wi \gg 1$, Figure 6.9(b),
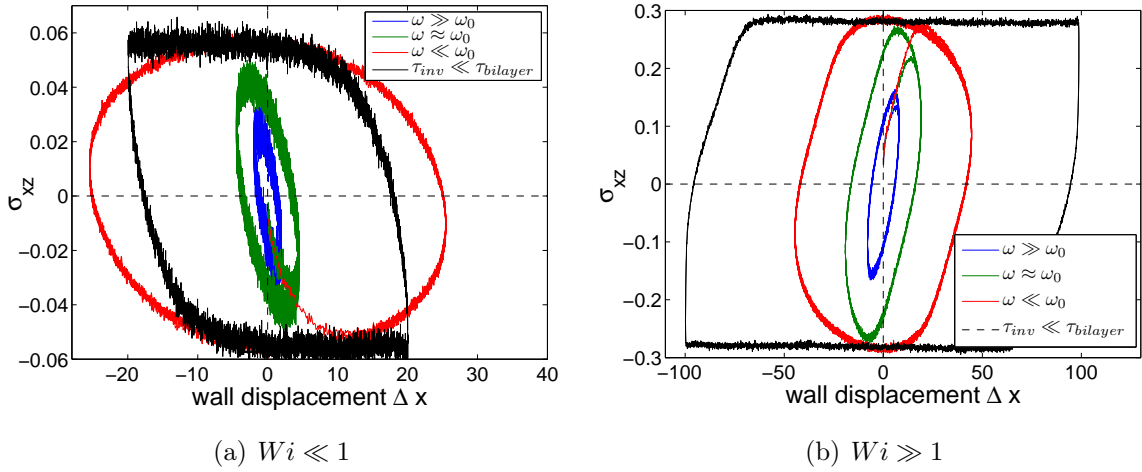
(a) $Wi \ll 1$ (b) $Wi \gg 1$

Figure 6.9: Two Lissajous figures are shown for the shear stress vs. the wall displacement [Eq. 2.23]. A single system ($N = 30$, $\rho = 4.4\rho^*$, $D_z = 17.5$) in linear response ($Wi \ll 1$) (a) and beyond ($Wi \gg 1$) (b) with three frequencies are shown. Additionally, for both regimes the response to almost instantaneous inversion of shear direction is added to the purely oscillatory shear. Above ω_0 the shear stress follows an ellipsoidal curve, below the shape changes and higher odd harmonics contribute to the curve. When the wall movement passes the equilibrium position the stress becomes almost constant and saturates at the steady state value. At approximately ω_0 the stress is still below the steady state limit.

the responses during the inversion are added and show sharp more trapezoidal like transitions. In both cases, when the strain becomes large enough, the shear stress reaches its maximum value. For analyzing experiments one assumes that steady state is reached. Therefore, the interpretation of early experiments in Ref. [9], where the regime of LAOS could not be reached, should be critically reviewed [85].

6.3.2   Shear hysteresis of polymers

Similar to the Lissajous figures in Figure 6.9 now the wall velocity is taken on the abscissa, see Figure 6.10. For $\omega \gg \omega_0$ the curve is ellipsoidal which turns for decreasing frequency into a hysteresis shaped curve. At the outer fringe, when the wall velocity reaches its maximum value, the loop closes. The imaginary part of the dynamic susceptibility is usually interpreted as the dissipation term, which is well known in spectroscopy. The energy ϵ dissipated per unit volume and cycle of input
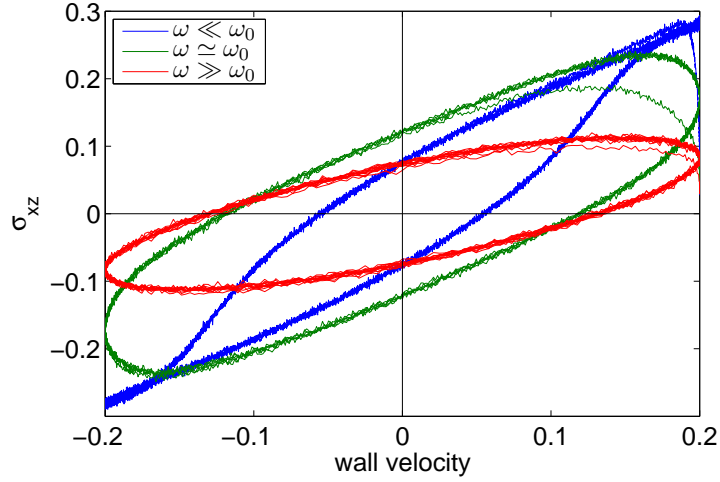
Figure 6.10: The shear stress plotted against the wall velocity shows a hysteresis. The curves flatten for systems that reach steady state, e.g. $\omega \ll \omega_0$.

oscillation is given by [86]

$$\epsilon = \int_0^{2\pi/\omega} \sigma_{xz}(t)\dot{\gamma}(t)dt \ . \tag{6.24}$$

When Eq. (6.2) and the first Fourier amplitudes of the complex shear modulus are inserted into Eq. (6.24), the dissipated energy per cycle becomes [87]

$$\epsilon = \frac{\pi\gamma_0}{\omega}G''(\omega) \ . \tag{6.25}$$

Both equations are compared in Figure 6.11, where the measured values of $\sigma_{xz}(t)$ and $G''(\omega)$ are used. For small turning cycles (large ω) a lot of energy is dissipated per cycle, while for large turning cycles (small ω) the heat production is strongly reduced. The origin of this observation is discussed in the section 6.6. The prefactor in Eq. (6.25) does not match with the calculated ϵ. An arbitrary prefactor is used to scale Eq. (6.25) downwards to obtain a qualitative agreement with the observed data.
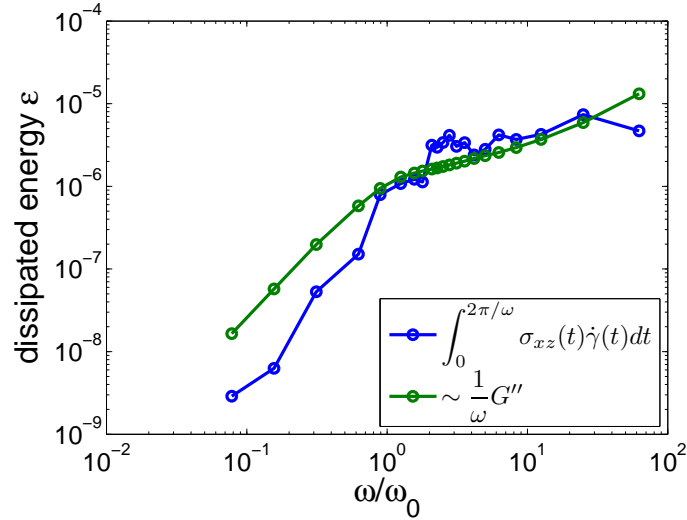
Figure 6.11: The energy dissipation per cycle as a function of the frequency is shown. At large frequencies $\omega \gg \omega_0$ the dissipated energy is dominated by the reorientation of the fluid. When crossing over to lower frequencies, the relaxation of the brush dominates, where less energy is dissipated.

6.4 Friction coefficient

The (stationary) friction coefficient defined in section 4.1.2 [Eq. 4.2] as the ratio of shear over normal stress can also be defined as a time dependent friction coefficient. Figure 6.12 shows how (also in the experiment) the responses look like and how the coefficient of friction is determined. The stresses must reach steady state to provide almost constant frames allowing to obtain a time-independent friction coefficient. For large frequencies the shear stress exhibits a certain delay to the driving of the walls and circles on a deformed ellipsoidal loop when plotted against the wall displacement. When the driving frequency is set below ω_0 the shear component of the stress tensor saturates and becomes almost constant. Figure 6.13 shows an example how the friction coefficient changes with frequency. The inset displays the response of the normal stress. When steady state is observed the z-component increases slightly as already mentioned in chapter 4. For smaller turning periods the normal pressure component remains constant at the equilibrium value.
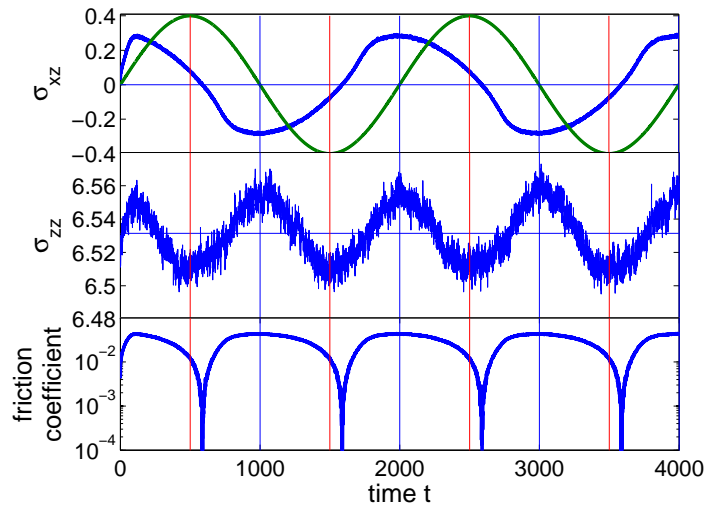
Figure 6.12: The fluidic responses during oscillation. Upper plot: shear stress and how it follows the wall displacement (green: sinus function). Middle plot: normal stress. Lower plot: the ratio of both time series displaying the time-dependent friction coefficient.
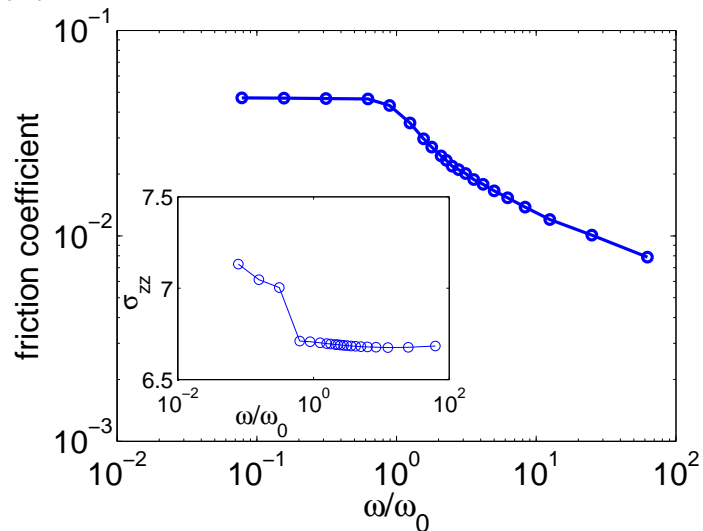
Figure 6.13: The friction coefficient as a function of ω. The inset shows the normal stress component as a function of ω. For $\omega \ll \omega_0$ the normal stress component grows up to 6% while for $\omega \geq \omega_0$ the equilibrium pressure is attained.

6.5 Microscopic response

The macroscopic response is connected to the chain response. As it is discussed in chapter 3 the chains respond to the wall movement via inclining, elongating in shear
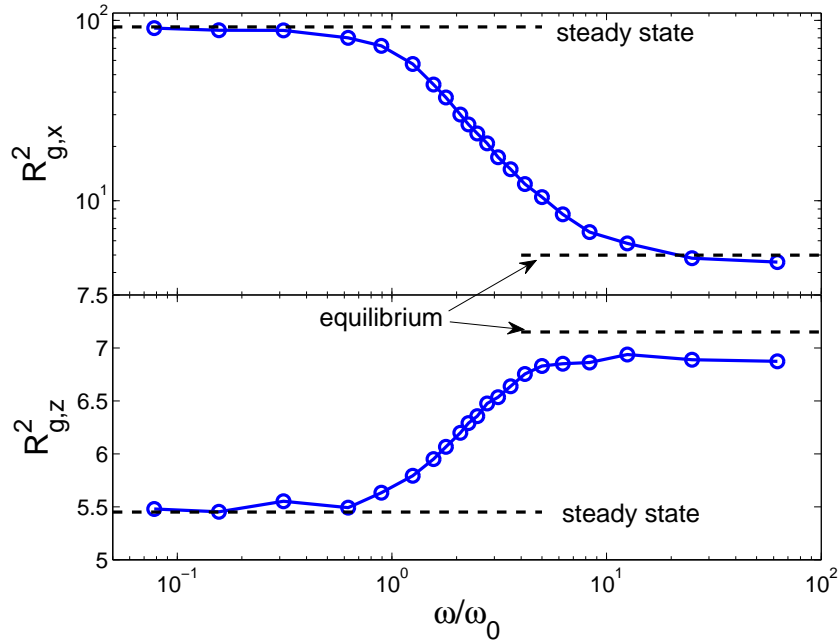
Figure 6.14: The lateral ($R_{g,x}^2$, upper plot) and orthogonal ($R_{g,z}^2$, lower plot) extensions of the chains as a function of ω are shown and compared to the equilibrium and steady state shear values (black dashed lines). The equilibrium value is observed after one system in the oscillatory regime ($\omega \gg \omega_0$) was stopped.

direction, and reducing the brush height. In Figure 6.14 lateral (x) and gradient (z) components of R_g^2 are shown as a function of ω. For high frequencies the brushes do not respond in shear direction, since the strain is very small compared to the typical lateral extension in equilibrium. Interestingly, the chains shrink orthogonal to the substrate. On the other hand, for large turning times the chain extensions reach their steady state value.

6.6 Velocity profiles

For a system driven above its resonance frequency the relaxation cannot take place. The wall movement is propagating into the flow, displacing first only the material accumulated at the walls. The momentum propagates quickly into the system establishing a linear profile. During half a cycle the wall velocity goes sigmoidally from $v_0 = -v_0$, the velocity profile remains almost linear. Small retardation effects only occur close to the walls, see Figure 6.15(a). With decreasing driving frequency

(a) $\omega \gg \omega_0$

(b) $\omega \lesssim \omega_0$

(c) $\omega \ll \omega_0$
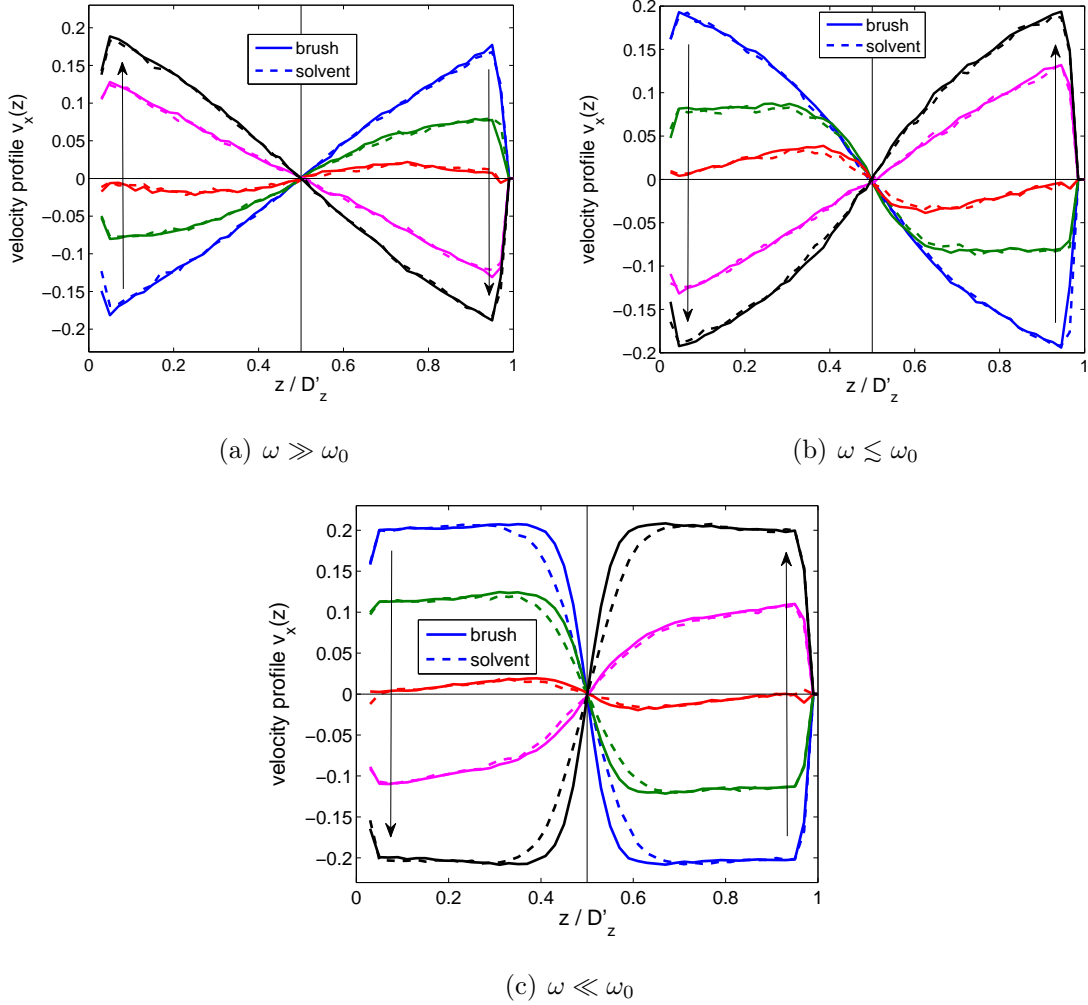
Figure 6.15: For three different frequencies a series of velocity profiles during half a cycle is shown. The arrows indicate the shear directions of the walls. The solid lines represent the brush profiles, the dashed lines the explicit solvent.

approaching ω_0 the situation does not change significantly, a linear profile is observed always for $\omega \geq \omega_0$. Below ω_0 a linear profile is still observable. When the linear profile within the small interpenetration layer between the brushes is extrapolated to the wall velocity, the hydrodynamic boundary z_z^{brush} is not found at the walls but inside the system. For $\omega \ll \omega_0$ the effective gap width $D_z/2 \pm z_z^{\text{brush}}(\dot{\gamma})$ is established and throughout the cycle the effective gap size does not change significantly. In Figure 6.15(b), where $\omega \leq \omega_0$ the brushes start to relax indicated by a steepening linear profile. In Figure 6.15(c) the linear profile is even steeper and the effective gap width has reached steady state, as discussed in section 4.6. When the brushes

pass the equilibrium velocity, retardation is observed. The particles further inside the channel are still moving. In this case, mass is displaced and retardation effects arise from inertia. Figure 6.15(c) displays the case for large wall amplitudes and the smallest tested frequency. Here, the displacement rate is so small the brushes may relax and an steady state shear profile is observed. During the zero crossing of the wall velocities the shear rate is the large enough that th hamper the relaxation process. In all three plots the velocity profiles of the solvent has been added. The arrows in the plots show the direction of the wall movement for half a cycle.

As discussed in section 5.5, during the oscillation the flow profile of the solvent along the xz-direction is analyzed, but not shown. As long as the linear profile is established, strong micro-turbulences are observed, which do not vanish until the brushes are able to relax into steady state. For large frequencies those turbulences dissipate more energy per cycle than for small frequencies, which is sustained by Figure 6.11. Only when the brushes reach steady state sliding the kinetic energy is distributed homogeneously along the gap increasing the normal pressure, as shown in the inset of Figure 6.13.

6.7   Characteristic time scale
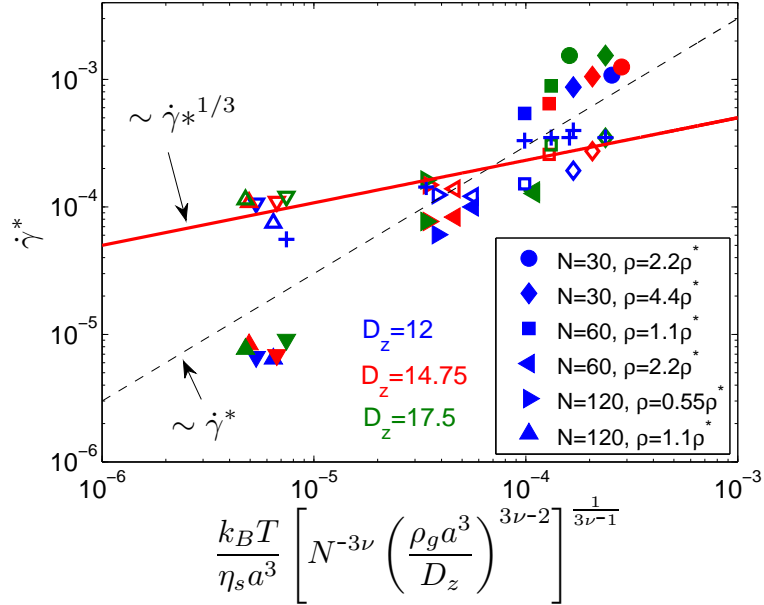
Figure 6.16: All critical shear rates for systems with explicit solvent obtained in steady state (filled symbols), the resonance frequencies ("+" symbols) and the chain segment relaxation times are compared to Eq. (4.12). Interestingly, the oscillatory time and the relaxation time of the Kramers problem match quite well, indicated by the red solid line, which, on the other hand, indicates a slightly different dependence on the control parameters.

The characteristic material-dependent time $1/\omega_0$ for strongly compressed brushes classifies two regimes, terminal or flow region and the pseudo-solid response region, where the brushes are unable to relax completely.

All measured critical shear rates, the inverse relaxation of an endmonomer of one chain inside the overlap (section 4.2.1), the critical shear rate (section 4.2), and the resonance frequencies are compared to Eq. (4.12), are shown in Figure 6.16. Three major clusters are observed indicating that the chain length N has the strongest impact, weak deviations occur with different grafting density and compression. The critical shear rates follow nicely the found theoretical expression (Eq. (4.12) dashed black line). The deviations from the theoretical prediction may originate from the prefactors η_s and the effective monomer size a. For chain length $N = 30$ and $N = 60$ (right and middle cluster in Figure 6.16) the determined inverse relaxation time

(open symbols) and resonance frequencies ("+" symbols) sustain nicely to the theory. The strongest deviations are observed for the longest simulated chains $N = 120$. The inverse relaxation time indicates an acceleration of the relaxation at equilibrium compared to the lateral relaxation in steady state. Here it is suggested that not the diffusion of the end-monomer but the diffusion of a free end-segment of the chain inside the overlap may increase the relaxation time. The resonance frequency is given by the linear extrapolations of the shear moduli in the small frequency limit, their slopes represent neither the zero-shear viscosity nor zero-compliance but their corresponding values at large Weissenberg numbers. The Weissenberg number determined for the tested system ($N = 120$, $\rho = 1.1$, $D_z = 17.5$) at $v = 0.2$ is $Wi \approx 10^3$, therefore far from linear response.

6.8 Single chain in simple oscillatory flow

While a significant contribution towards the understanding of systems with multiple tethered polymer chains (polymer brushes) is given in this context, single tethered polymer chain dynamics still remain challenging. The ability to visualize single polymers via fluorescent staining has revealed many nontrivial individual chain dynamics providing rich dynamics when exposed to shear. Several studies examined single tethered DNA-chains in stationary shear flow experimentally [74] and numerically [69, 88]. Numerical investigations of chains in oscillatory flow are rare [89]. The long-time dynamics of a single end-grafted chain under steady and oscillatory Couette flows is studied. The next section will discuss the simulation details and how the oscillatory driven dynamics are explored. In the second section the chain will be treated in a mathematical model as an over-damped harmonic oscillator dragged through a fluid. The results of the investigation congregate in the last section.

6.8.1 Simulation details

In our simulation, twenty chains with $N = 30$ are grafted regularly onto the substrate. The distance between two neighbouring chains is chosen such that the chains do not interdigitate. Figure 6.17 shows a simulation snapshot of 20 chains at equilibrium. For clarity, the solvent dimers and the upper boundary wall have been removed.

In equilibrium, the longest relaxation time τ is determined from the exponential decay of the autocorrelation function of the lateral position of the center of mass

$$C(t) = \frac{\langle R_{i,\mathrm{cm}}(0)R_{i,\mathrm{cm}}(t)\rangle}{\langle R_{i,cm}^2(0)\rangle} \sim \exp(-t/\tau) \quad \text{for} \quad i = x, y \,. \tag{6.26}$$

For $N = 30$ a relaxation time of $\tau \approx 350\tau_{\mathrm{LJ}}$ was measured.

The monomer distribution for that simulation model with explicit solvent can be compared with the study of Kreer *et. al.* [58], where single endgrafted chains at equilibrium were studied. Figure 6.18 shows the monomer distribution $\Phi(z)$ along the gap normalized by $\Phi(z = R_{\mathrm{g}})$ versus z/R_{g}. Starting from the grafting point $(z \ll R_{\mathrm{g}})$ the distribution grows with a power law and decays exponentially for $(z \gg R_{\mathrm{g}})$. The exponential fit in Ref. [58] is qualitatively close to the observed density profile. The origin of the deviation is the upper substrate, chains would be able to stretch slightly further than the wall distance is set. Due to computational
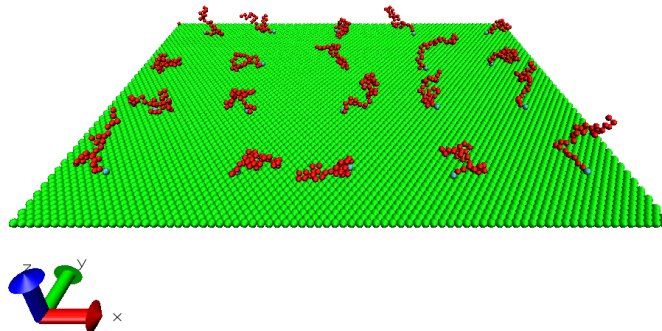
Figure 6.17: Snapshot of regularly end-grafted chains without overlap onto the lower substrate. For clarity the upper wall and explicit solvent dimers have been removed.
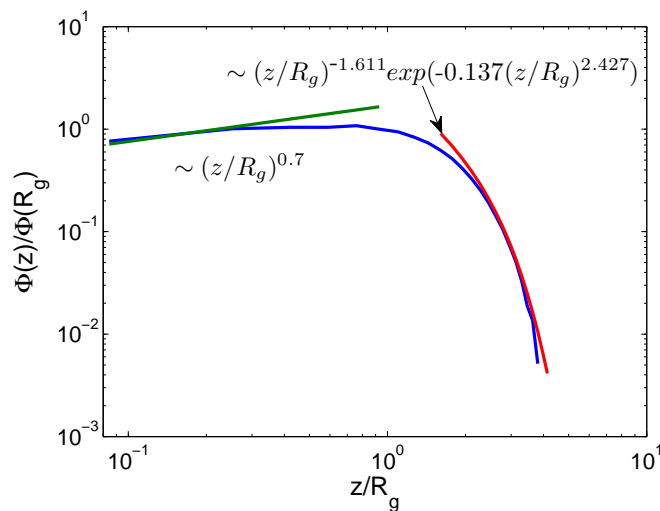
Figure 6.18: Log-log plot of the normalized monomer density profile $\Phi(z)/\Phi(R_g)$ vs. reduced distance z/R_g in the mushroom regime. The theoretical expectations according to Ref. [38] for $z \ll R_g$ and for $z \gg R_g$ are indicated by the green and red lines.
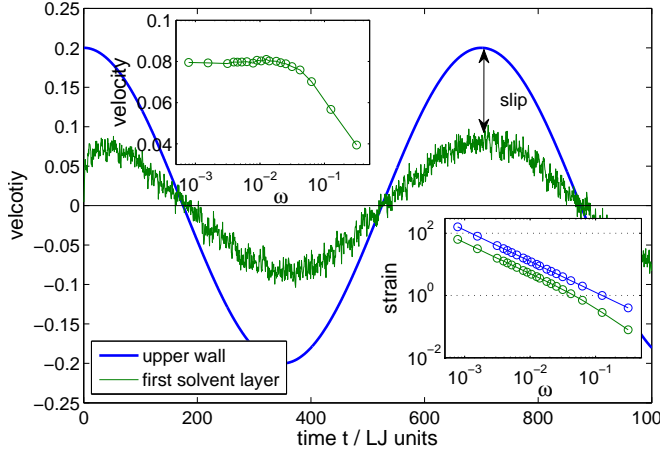
Figure 6.19: The wall is driven with a fixed velocity and the first solvent layer follows with a smaller velocity. The upper inset shows the velocity of the first solvent layer vs. the frequency. At large frequencies the inertia of the solvent weakens the susceptibility. The lower inset shows the strain of the wall and the first solvent layer.
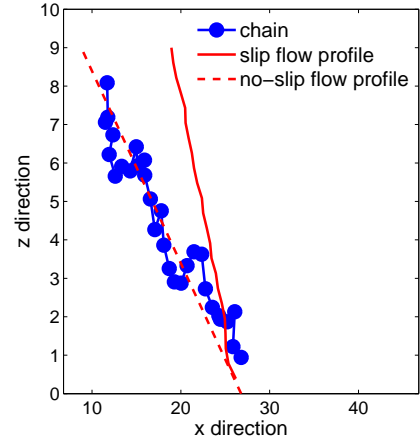
Figure 6.20: A snapshot of a single polymer chain during shear. The red dashed line represents the actual velocity profile, the red solid line the velocity profile for the no-slip boundary condition.

time the substrates' distance is chosen at $D_z = 10$ limiting the volume for the dimers to occupy, and hence the number of solvent molecules that have to be simulated at a given total density, $\rho = 0.9$. However, the deviations are small and can be neglected for the further discussion.

6.8.2 Oscillatory wall movement

To the upper wall an oscillatory velocity protocol is applied, see Figure 6.19,

$$v(\omega, t) = v_0 \cos(\omega t) . \tag{6.27}$$

Similar to the discussion in section 6.1, the strain becomes a function of the driving frequency ω, Eq. (6.2),

$$\gamma_{\text{eff}} = \frac{v_{\text{eff}}}{D_z \omega} . \tag{6.28}$$

All particles are interacting via the purely repulsive part of the LJ-potential [Eq. (2.1)], which means the solvent does not stick at the wall. Hence, a slip on both walls is expected. The velocity profile is carefully observed to ensure a linear shear profile

along the gap despite the slip. In Figure 6.20 the situation is shown, where the wall induces a steep shear profile (red solid line), while the solvent (dashed red line) does not follow the wall movement entirely. Figure 6.19 shows the velocity of the wall and the first solvent layer at the wall, where a slip occurs. The upper inset shows that the slip is rather constant over a wide frequency range, the slip increases with higher frequencies, the fluid's susceptibility to follow the driving decreases. That limits the exploration of the high frequency regime of the single chains. To overcome this problem, one may define another boundary interaction, e.g. the upper substrate could be covered with short end-grafted chains creating a mesh or an attractive LJ-potential for the fluid-wall interaction could be introduced, which creates a no-slip boundary condition. None of these ideas were implemented here. Therefore, the wall induces an effective strain γ_{eff}, which is related to the first layer velocity. The lower inset in Figure 6.19 shows the effective strain of the first layer (green line) compared to the walls strain (blue line). The first solvent layer induces a linear profile towards the lower substrate, a small slip occurs there, too, but it is negligible. This may be attributed to the fact that the grafted chains hamper the slip.

6.8.3 Over-damped harmonic oscillator in shear flow
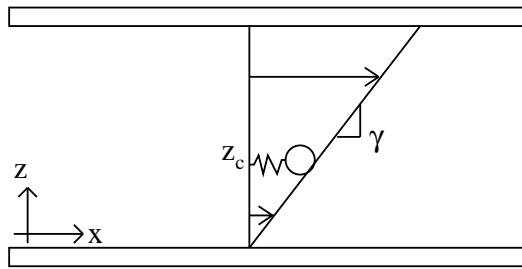
Figure 6.21: A sketch of a two-dimensional harmonic oscillator in simple shear flow. The inclining line represents the strain γ of the flow, which moves the bead attached at $(0, z_{\mathrm{c}})$ in x and z direction.

To develop a theoretical model the center-of-mass of a single chain is projected onto a single bead, which is attached at a certain distance z_c above the surface, see Figure 6.21. When now the upper wall induces the Couette flow in x-direction, the driven medium drags the bead out of its equilibrium position. A spring counterbalances the viscous force pulling the bead back to its anchoring point. The bead has

also another degree of freedom allowing it to transit along the z-axis in and out of high velocity gradients. The equations of motion for the bead are given by

$$\zeta_{\text{fluid}} \left(\frac{dx}{dt} - \dot{\gamma}z \right) = -kx \tag{6.29}$$

and

$$\zeta_{\text{fluid}} \left(\frac{dz}{dt} \right) = -k(z - z_{\text{c}}) , \tag{6.30}$$

where ζ_{fluid} represents the damping constant of the fluid and k the spring constant, which mimicks an elastic response of the polymer. Both equations of motion may additionally include a stochastic term, which vanishes after averaging. The coupled differential equations can be solved by solving first Eq. (6.30)

$$z(t) = z_{\text{c}} + (z_0 - z_{\text{c}})e^{-\frac{t}{\tau}} \tag{6.31}$$

with $\tau = \zeta_{\text{fluid}}/k$ the relaxation time of the spring and z_{c} the starting height of the bead above the lower substrate. Now Eq. (6.29) can be expressed as

$$\begin{aligned} x(t) &= x_0 e^{-\frac{t}{\tau}} \\ &+ \int_0^t dt' \dot{\gamma}(t') e^{-\frac{t-t'}{\tau}} \left[z_{\text{c}} + (z_0 - z_{\text{c}})e^{-\frac{t'}{\tau}} \right] . \end{aligned} \tag{6.32}$$

For constant shear, Eq. (6.32) is solved,

$$x(t) = x_0 e^{-\frac{t}{\tau}} + \tau \dot{\gamma} z_{\text{c}} (1 - e^{-\frac{t}{\tau}}) + t\dot{\gamma}(z_0 - z_{\text{c}})e^{-\frac{t}{\tau}} . \tag{6.33}$$

In the limit $t \to \infty$ the stretching of the spring in the flow becomes

$$x(t \to \infty) = z_{\text{c}} \tau \dot{\gamma} . \tag{6.34}$$

Equation (6.33) can be solved for an oscillatory flow

$$\dot{\gamma} = \gamma \omega \cos(\omega t) \tag{6.35}$$

to

$$\begin{aligned} x(t) &= x_0 e^{-\frac{t}{\tau}} + (z_0 - z_{\text{c}})\gamma e^{-\frac{t}{\tau}} \sin(\omega t) \\ &+ \frac{z_{\text{c}}\gamma\omega\tau}{1 + (\omega\tau)^2} \left[\cos(\omega t) + \omega\tau \sin(\omega t) - e^{-\frac{t}{\tau}} \right] . \end{aligned} \tag{6.36}$$

In the limit of $t \to \infty$ the beads movement becomes

$$x(t \to \infty) = \frac{z_{\text{c}}\gamma\omega\tau}{1 + (\omega\tau)^2} \left[\cos(\omega t) + \omega\tau \sin(\omega t) \right] . \tag{6.37}$$
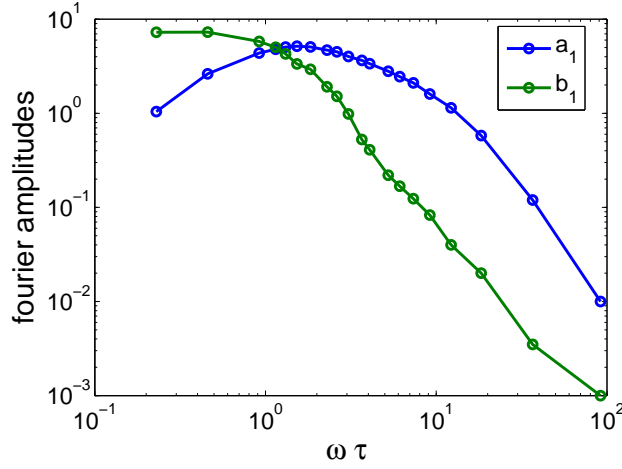
Figure 6.22: A double logarithmic plot of both first Fourier amplitudes vs. the normalized frequency. The intersection of both amplitudes indicate a resonance frequency of $\omega_0 \approx 1/\tau$.

With an addition theorem for trigonometrical functions, Eq. (6.37) yields

$$x(t) = \frac{z_c \gamma \omega \tau}{\sqrt{1 + (\omega \tau)^2}} \sin(\omega t + \Phi) \qquad (6.38)$$

with the phase shift

$$\Phi = \cot^{-1}(\omega t) . \qquad (6.39)$$

Equation (6.38) can be decomposed into two limits

$$x(t) = z_c \gamma \sin(\omega t), \qquad \text{for} \quad \omega \tau \gg 1 \qquad (6.40)$$

$$x(t) = z_c \gamma \omega \tau \cos(\omega t), \quad \text{for} \quad \omega \tau \ll 1 . \qquad (6.41)$$

6.8.4 Single chain response

During the simulation the center of mass is recorded. The response of the chain is decomposed with Fourier analysis into the two leadings terms. One can find both first Fourier amplitudes via

$$a_1 = \frac{2}{M} \sum_{i=1}^{M} R_{cm,x}(t_i) \cos(\omega t_i) , \qquad (6.42)$$

$$b_1 = \frac{2}{M} \sum_{i=1}^{M} R_{cm,x}(t_i) \sin(\omega t_i) . \qquad (6.43)$$

$R_{\mathrm{cm},x}(t_i)$ is the center of mass at t_i with $i = 1 \ldots M$ observation steps. Figure 6.22 shows both Fourier components as a function of the normalized frequency $\omega\tau$. For lower frequencies the cosine-component of the flow dominates the chains response. It is emphasized that the intersection point of $a_1(\omega)$ and $b_1(\omega)$ represents a resonance frequency $\omega_0 \approx 1/\tau$. Another quantity extracted from the center of mass movement is the standard deviation around the grafting point of each chain

$$\Delta R(t)_{\mathrm{cm},x} = \sqrt{\langle (x(t) - x_0)^2 \rangle} \,, \tag{6.44}$$

where $\langle\rangle$ denotes the average over all chains for a given frequency, $x(t)$ the position of the center of mass in time relative to the grafting point x_0. The difference between extracting the Fourier amplitudes and the standard deviation is given by the weight how each point in time contributes to the average quantity. The Fourier amplitudes weight the center of mass in time depending on the phase of the trigonometrical functions. On the other hand, in Eq. (6.44) each point in time contributes equally to the deviation around the grafting point. Due to different weight functions of the same observable different results are expected. In Figure 6.23 the chain responses according to Eq. (6.44) and the sum of both Fourier amplitudes as a function of ω are compared to the expression in Eq. (6.38). For both methods the strain was identified as the effective strain, Eq. (6.28). Both observables follow for small frequencies the prediction of the bead model nicely and grow linearly with ω. In the crossover region $\omega\tau \approx 1$ a plateau is reached. For higher frequencies both quantities deviate, the Fourier amplitudes decrease and the standard deviation grows linearly with ω. In contrast, the bead model stays constant for higher frequencies. The model does not take into account that the chains are made of N monomers with finite inertia. In the high frequency limit the model therefore breaks down. The inset of Figure 6.23 shows the center of mass parallel to the surface including both limits, steady state ($\omega\tau \to 0$) and equilibrium ($\omega\tau \to \infty$), representing the average position of the massless bead z_{c}. When the Fourier amplitudes are corrected by this average z-position, $\sqrt{(a_1^2 + b_1^2)}/\gamma_{\mathrm{eff}}R_{\mathrm{cm},z}$, the theory is still off by a factor of 2.

On the other hand, the phase is in rather good agreement with the solution of the simplistic model. One can derive the phase from the Fourier amplitudes, yielding

$$\phi(\omega) = \tan^{-1}\frac{b_1(\omega)}{a_1(\omega)} \,. \tag{6.45}$$

The phase ϕ is compared with Eq. (6.39) in Figure 6.24. In the free drain limit quasi
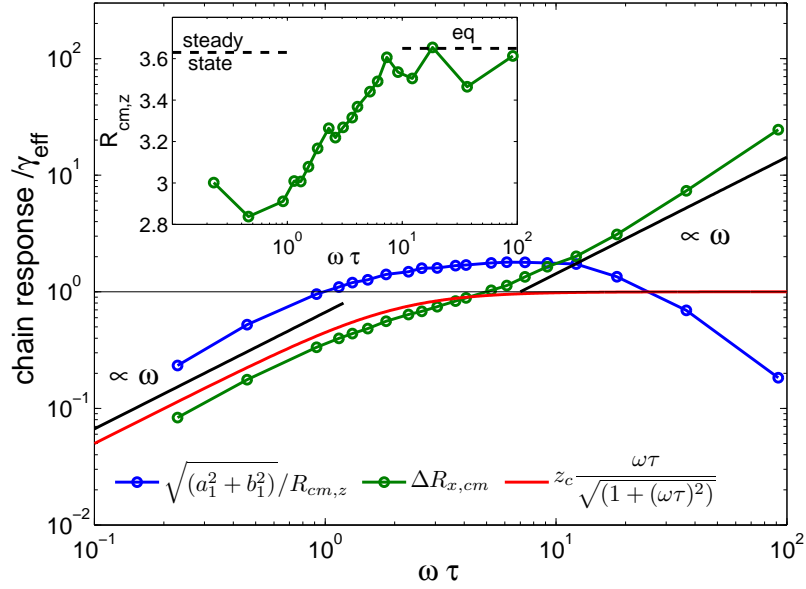
Figure 6.23: Log-log plot of the chain's response. The blue line shows the sum of first Fourier components a_1 and b_1, which is compared to the center of mass of $R_{cm,x}$ (green line). The center of mass responds at high and low frequencies linearly with ω, but the Fourier components saturate and decrease with high ω. Noise is dominating the center of mass movement in the high frequency regime. The inset shows the recorded z-position of the center of mass, including both limits, steady state ($\omega\tau \to 0$) and equilibrium ($\omega\tau \to \infty$) values.
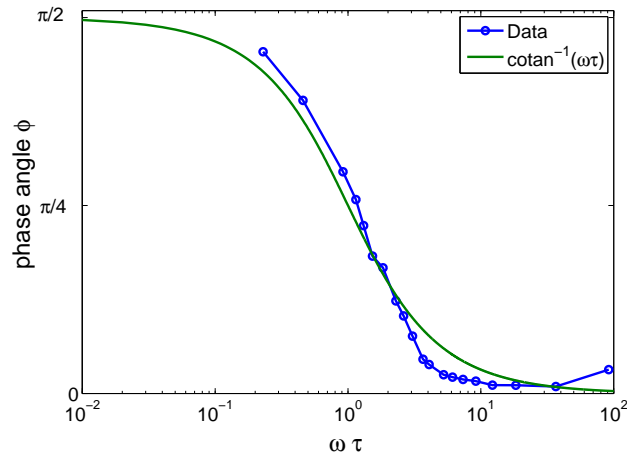
Figure 6.24: Semi-log plot of the phase. The red line indicates the solution given by Eq. (6.38) compared to the phase shift observed in the simulation.

cyclic dynamics are observed. Similar to the experimental observation in Ref. [74], the PSD does not reveal any specific frequency but single frame analysis of the trajectory indicate tumbling motion.

6.9 Summary

This chapter dealt with oscillatory shear of confined liquids. The last section dealt with the problem of a single chain at equilibrium and in an externally oscillatory driven flow. The observed density profile in equilibrium was compared to a study of the same simulation model with implicit instead of explicit solvent. Slight deviations occur when the system is limited by two walls to confine the added explicit solvent molecules. Otherwise the observed profile is close to the theoretical description, the dimer solvent seems to have a marginal effect on the universal stretching of the single end-grafted chains.

The system was driven by a time-dependent strain, $\gamma(t) = \gamma_{\text{eff}} \sin(\omega t)$, where γ_{eff} represents the effective strain due to slip at the walls. The first solvent layer and not the upper wall's displacement defines the effective strain. The numerical observations with changing driving frequency ω were compared to an overdamped single bead-spring model, where the polymer chain is projected onto one bead. The model is in good agreement with the simulation data. The investigation can be seen as a starting point for further investigations, where hydrodynamic interactions between the end-grafted chains may be studied. The mathematical model may be extended to two coupled chains exhibiting phase-locking or mode coupling.

The first part of this chapter dealt with two compressed brushes, similar to the SFA geometry. The observed shear stress was decomposed into the first two Fourier amplitudes, representing the complex shear modulus. Higher odd contributions in terms of non-linearity were discussed and further on neglected. The complex shear modulus $G^*(\omega)$ and its time-domain counterpart, the relaxation modulus $G(t)$ of the fluid, exhibit two major regimes, the flow regime and the plateau regime. Both regimes are separated by the material's characteristic relaxation time or resonance frequency.

The resonance frequency was compared to the earlier found characteristic relaxation times and critical shear rates separating linear from non-linear response with respect to the Weissenberg number. The resonance frequency seems to be related to the residence time of a chain segment inside the overlap region, where dissipation takes place.

Chapter 7

Fluctuations in the interface

The theory for equilibrium brushes starts with the discussion of the mean field theory of MWC where local fluctuations are neglected in the limit of strong stretching, $N\rho_{\mathrm{g}} \to \infty$. More realistic is finite chain stretching which leads to different density profiles. In both free brushes and compressed brushes the density profiles drop exponentially towards the free ends. In the equilibrium study the overlap was introduced characterizing the brush-brush interface, depending on the system's parameters N, ρ_{g} and D_z. The width of that interface with its microscopic details dominate the frictional response to shear. The continuum description in chapter 4 (section 4.6) introduces the slip. According to Refs. [90–92] when all the parameters, slip length b and the hydrodynamic boundary z_h are known, the viscosity can be extract from a Green-Kubo relation

$$\frac{\eta}{b} = \frac{1}{Ak_{\mathrm{B}}T} \int_0^\infty dt \langle F_\parallel(0)F_\parallel(t) \rangle \;, \tag{7.1}$$

where $F_\parallel(t)$ denotes the parallel force between the substrate and the flow at time t, and A is the area of the substrate. This relation suggest that the slip length depends on the interaction, $V_{\mathrm{wall}}(z)$, between wall and fluid like [92]

$$b \approx \frac{(k_{\mathrm{B}}T)^2}{S_\parallel(q_{\mathrm{wall}})\hat{\sigma} \int_0^\infty dz \Phi(z) V_{\mathrm{wall}}(z)} \;, \tag{7.2}$$

where $S_\parallel(q_{\mathrm{wall}})$ is the structure factor of the liquid at the wave vector, q_{wall}, that describes the corrugation of the substrate, $\hat{\sigma}$ is the particle size, and $\Phi(z)$ the local density. It is pointed out that the theory implies a flow past an ideal interface with slip. In section 6.6 such a slip occurred along the upper surface. For a flow past a brush coated surface the Navier slip boundary cannot be formulated consistently

for both conditions, z_h and δ as discussed in Refs. [75, 93]. More interesting appears the flow of one brush past another one, where both are in contact. Equations (7.1) and (7.2) are discussed in this context.

In the first section a phenomenological description of local brush height is used to define a surface of a brush coated surface. The projection method is further deployed to the compressed brush to define $S_\parallel(q)$ in Eq. (7.2). In the second section a discussion of the autocorrelation function in Eq. (7.1) is carried out, where the fluctuations inside to overlap are considered.

7.1 Local structure of a free brush and a compressed bilayer
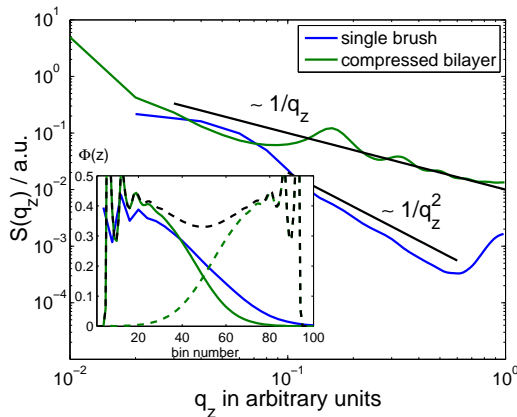
Figure 7.1: A log-log plot of the structure factor in z direction of compressed and uncompressed polymer brushes. The inset shows the density profiles. There is no brush specific length scale introduced, therefore the scattering vector is arbitrary units.
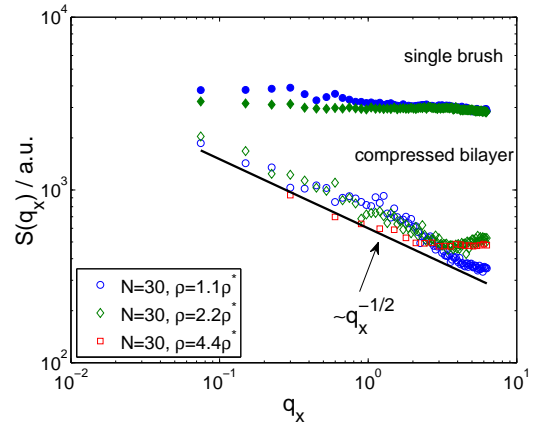
Figure 7.2: A log-log plot of the planar static structure factor of the single brush and the compressed bi-layer surface. For the uncompressed brush the spectrum is nearly flat, while for the compressed case a scale free behavior above several monomer radii is observed.

With the help of neutron scattering the brush profile is known for a single polymer brush. To extract the spatial fluctuation spectrum we performed a Fourier analysis in reciprocal space, similar to Eq. (6.12) yielding

$$S(q_i) = \langle \widetilde{X}(q_i) \times \widetilde{X}^*(q_i) \rangle , \tag{7.3}$$

where $\langle\rangle$ denotes the average, $\widetilde{X}(q_i)$ the Fourier transformed of the real space observable, $\widetilde{X}(q_i)$ its complex conjugate, q_i the reciprocal wave vector, and i the spacial direction. In Figure 7.1 the structure factor for both profiles are shown, single brush and uncompressed bilayer. In agreement with the study [94, 95] the single compressed profile shows structure factor $S(q_z) \sim (q_z)^{-\beta}$ with $\beta = 2$. When the brushes are compressed, the structure factor given by one of two brushes decays with an exponent $\beta = 1$. To our knowledge no experimental measurements of the structure factor of a single profile in compressed bi-layers are available. A more sophisticated experimental setup, where the monomers of one brush are differently chemically labeled, is needed, such that a single compressed profile can be measured. On the other hand, it can be shown, that the structure factor of the total monomer profiles, which is experimentally available, decays even more slowly (with $\beta < 1$) as long as the overall profile is not uniform. The inset in Figure 7.1 shows the monomer densities of both cases, the green solid line represents the lower brush and green dashed line the corresponding upper brush. The black dashed line represents the sum of both profiles, the related Fourier spectrum is not shown. The reciprocal lattice vector in Figure 7.1 is given by $q_z = 2\pi n/n_{\mathrm{bins}}$ with $n = 1 \ldots n_{\mathrm{bins}}$ the number of bins perpendicular to the walls, which was chosen arbitrary, therefor q_z is in arbitrary units. The abscissa scales with the size of the bins since no brush specific length scale was introduced.

A projection method is introduced to visualize the local lateral structure created by a single brush. The surface in the xy-plane is subdivided into a lattice using the smallest length scale in the system, the monomer size $\sigma = 1$. Each monomer belonging to one brush is projected into a bin of the lattice depending on its xy-position above the substrate. The number of monomers stacked in one bin is proportional to the local height defining a local polymer layer height. A visualization of such a "carpet" is shown in Figure 7.3. The color bar encodes the local number of monomers above the substrate. When the position of the monomers are projected in z-direction, the density profile with its exponential tail of the inset in Figure 7.1 is recovered. When now the static structure factor is calculated via Fourier transformation of the "carpet"-like structure, the observed structure factor $S(q_x)$ for

$$\frac{2\pi}{\hat{L}_x} \leq q_x \leq \frac{2\pi}{\sigma} \,, \tag{7.4}$$

where $\hat{L}_x = 4L_x$, mentioned in chapter 2, to obtain a broader wave spectrum. Each
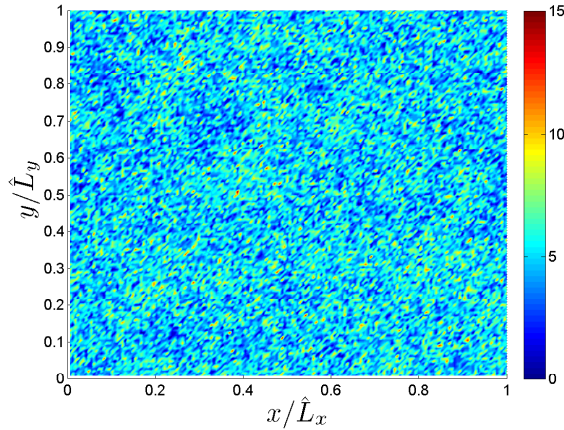
Figure 7.3: A view on top of a single polymer brush. The color-bar on the left indicates the amount of monomers stacked above the substrate. A rather homogeneous and smooth surface is observed.
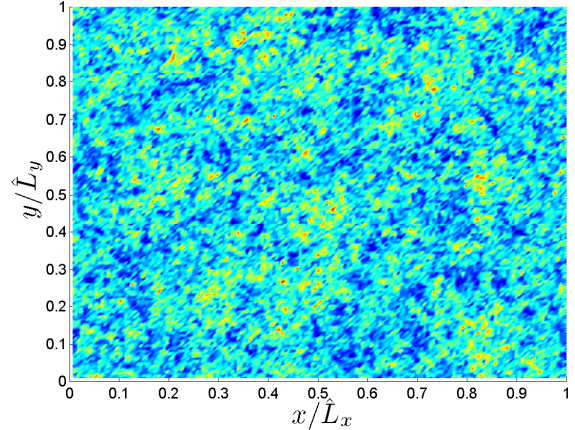
Figure 7.4: A top view of a compressed bilayer onto the lower brush and its monomer distribution above the lower surface is shown. Irregularities in the local distribution appear, clusters of high (red/yellow) and low (blue) monomer concentrations. The color-coding follows the color-bar in Figure 7.3.

scattering vector q_x is equally distributed indicating local uncorrelated statistics. A recent experiment investigated the surface morphology of single polystyrene brushes via atomic force microscopy (AFM) and X-ray diffusive scattering [96]. Their structure factor is in qualitative agreement with the data shown in Figure 7.2. For smaller q_x their spectrum is flat, but decreasing faster towards larger wave vectors by approximately one order of magnitude of intensity [96]. Such a strong decay is not observed here. The origin of this different behavior is unknown. A different picture can be drawn for the interfacial zone of a compressed bilayer. The same projection method is applied, where we distinguish between the monomers of upper and lower brush. Simply speaking the upper brush penetrates the lower brush by moving the monomers of the lower brush to the side. Since the overall density is uniform, islands of larger and smaller monomer concentrations appear. Inside of the lower brush valleys appear in the "surface", see Figure 7.4 color-coded in blue, and they must be compensated by peaks pressing into the upper brush, color-coded in red in Figure 7.4. Due to thermal fluctuations the picture is not stationary but alternating in time by turning peaks into valleys and vice versa. An analysis similar to the

discussion of the single brush surface, the fluctuation spectrum of the compressed bilayer height profile reveals a power law $S(q_x) \sim q_x^{-1/2}$, see Figure 7.2. That in turn implies long-range height fluctuations.

Due to the system size a variation of the grafting density, chain length, and including explicit solvent molecules is quit demanding in terms computational power, therefore, the discussion will concentrated on system with implicit solvent and short chains ($N = 30$). The observed power law in the lateral fluctuation spectrum for the compressed bilayer may exhibit for small scattering vectors a cut-off, revealing a length scale inside the system.

Contrary to the theoretical studies by Frederickson [97] where for the static fluctuation spectrum was defined as

$$S(q_\parallel) \simeq k_{\mathrm{B}}T / \left[\hat{\gamma} q_\parallel^2 + 2G q_\parallel + 3G/(q_\parallel^2 h^3) \right] \ , \tag{7.5}$$

where $q_\parallel$ is the in-plane scattering wave vector, $\hat{\gamma}$ is the surface tension, G the frequency independent shear modulus, and h is the film thickness. Regarding to Eq. (7.5), in the large wave vector limit the fluctuation spectrum must decay with a power law, $S(q_z) \sim q_z^{-2}$, which is not observed, neither for a single brush nor for the compressed bilayer. The deviating observations in Figure 7.2 from Eq. (7.5) are unknown and may motivate further studies. The lateral structure factor of the contact surface rises the question which wave vector suits best for Eq. (7.2), when for the fluctuation spectrum over a wide range a power-law is observed. In the high compression regime the brushes interpentrate each other building an interface, where at equilibrium a compromise between the osmotic pressure and the entropy of each brush is established. The pressure of each brush can be measured in terms of the overall binary contacts between them. In this case the forces exerted on one brush by the other can be measure as well, and used in Eq. (7.1). As mentioned in Ref. [92], the autocorrelation function is usually evaluated numerically, since no analytic function is known describing the overall interaction. Instead of evaluating the autocorrelation function the power spectrum can be used, given by the Wiener-Khinchin theorem, where the autocorrelation function of a stationary process is the Fourier transform of the PSD.

An unexpected universal behavior is observed when transforming the binary contact number $N_{\mathrm{int}}^{\mathrm{bb}}(t)$ into Fourier space. Other observables related to the number of contacts are examined as well, i.e. $F_x(t)$ between the brushes and the overlap
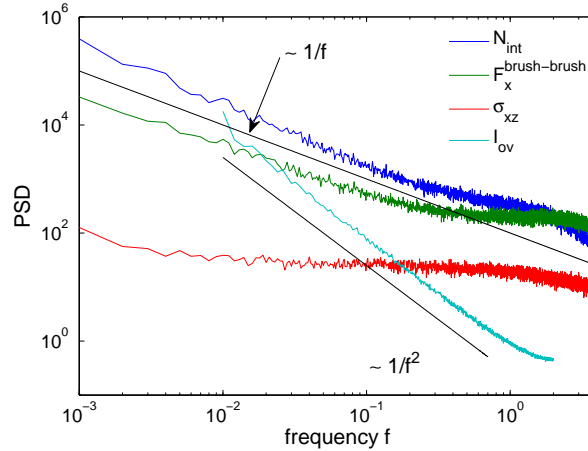
Figure 7.5: A double logarithmic plot for the power spectral density of several observables.

in time $I_{ov}(t)$. In Figure 7.5 several PSDs are plotted in frequency space. Interestingly the integrated overlap [Eq. (4.1)] does reveal Brownian type of noise instead of pink. The overall shear stress component $(\sigma_{xz}(t))$ for a system with explicit solvent exhibits a frequency independent fluctuation spectrum. For all time series exhibiting colored noise, the observation times are not long enough to reach the transition to an uncorrelated white noise, but for all observables a flat spectrum for $t \rightarrow \infty$ is expected. Referring back to Eq. (7.1), the integration of the autocorrelation function may become time consuming due to the long time correlation inside the interface. Generally, for a times series which is driven by white noise one would expect a constant plateau for the fluctuation spectrum. For intermediate times a shoulder frequency may occur, where a transition to Brownian noise $(1/f^2)$ or an exponentially decaying correlation function is present. For large frequencies (short times) a transition to white noise may occur again, due to the uncorrelated thermal noise imposed by the stochastic thermostat. If such transitions are present that turn white noise into colored noises, the complex system acts as a band pass filter [98].

7.2 Discussion of the 1-over-f noise

Fluctuations, which have spectral densities varying approximately as $1/f$ over a large range of frequencies, have been observed in tremendous variety of different

physical systems from physics, geophysics, astrophysics sociology and biology. A wide collection of publications dealing with that phenomenon and their classified appearance in different fields of science can be found in [99].

The first observation of 1-over-f noise was reported by Johnson [100], where the release of single electrons from the cathode in a vacuum tube creates a single current peak. The single spike event in time is described by an exponential relaxing process

$$N(t) = N_0 \exp(-\frac{t}{\tau}) \, , \tag{7.6}$$

where each single relaxation process exhibits a Lorentzian power spectrum

$$S(f) \sim \frac{N_0}{\tau^2 + f^2} \, , \tag{7.7}$$

with τ a single relaxation time. When a train of spikes with a uniform multiple relaxation time spectrum $p(\tau)$ between τ_1 and τ_2 is superimposed [101],

$$S(f) \sim \int_{\tau_1}^{\tau_2} \frac{\tau p(\tau)}{\tau^2 + f^2} dt \tag{7.8}$$

one finds

$$S(f) \sim \begin{cases} c & \text{for} \quad 0 \ll f \ll 1/\tau_1 \ll 1/\tau_2 \\ \frac{c}{f(1/\tau_2 - 1/\tau_1)} & \text{for} \quad 1/\tau_1 \ll f \ll 1/\tau_2 \\ \frac{c}{f^2} & \text{for} \quad 1/\tau_2 \ll f \end{cases} \tag{7.9}$$

with the two shoulder frequencies $1/\tau_1$ and $1/\tau_2$ limiting the pink noise spectrum. Many single relaxation processes contribute to a single response. This ubiquitous noise is present in many electronic devices like resistors and metal-oxide-semiconductor-field-effect transistors (MOSFET). In the number fluctuation model introduced by McWhorter [102], it is known that the noise is caused by random trapping and detrapping of the mobile carriers. Each single trapping and detrapping causes a signal with a Lorentzian or generation-recombination spectrum. Superpositioning a large number of these signals with the proper time constant results in a $1/f$-noise spectrum. Transferring these arguments to the fluctuations inside the brush-brush interface one possible explanation may start with a single end-monomer diffusing in a confined surrounding. One might expect a Lorentzian type spectrum for a monomer moving along a high dimensional energy landscape inside the interface becoming trapped and detrapped. It is not known, how the mobility and therefore the life time of single monomers are behaving. Not only the binary inter-brush contacts indicate long correlations but also intra-brush contacts behave

similarly. On the other hand, when the problem of local contacts is explored for a single uncompressed brush, the intra-brush contacts exhibit a Brownian type of power spectral density. The system changes completely the filter properties.

After the appearance of power laws in the theory of critical phenomena many scientist believe in a hidden mechanism behind the ubiquitous noise and the existence of an analogy to the universality exponents in critical phenomena. Other explanations have been discussed for the universal behavior, which was observed in quasi one-dimensional sand piles or snow fields exhibiting power law distributed avalanches abrogating repetitively a critical state of minimal stability and driving itself back - "Self-organized criticality" [103]. Such abrupt occurrence of extreme values (avalanches, earthquakes, landslides) is not observed in $N_{\text{int}}^{\text{bb}}(t)$.

7.3   Summary

The unexpected observation of long time correlations inside the brush-brush interface remains challenging. Several models are approaching the problem by superpositioning Lorentzian type of spectra with broadly distributed single relaxation times originating from local interactions and trapping or clustering mechanisms.

The filter properties of a single uncompressed brush tuning uncorrelated thermal fluctuations into $S(f) \sim 1/f^2$ power spectrum seem rather unspectacular. Additionally, the structure factor of single uncompressed brush, given by the density profile, exhibits a Brownian spacial noise ($S(q_z) \sim q_z^2$) and a flat uncorrelated brush height fluctuation spectrum.

Significant changes occur when brushes are compressed. The single brush profile inside the bilayer exhibit $S(q_z) \sim q_z$, while the fluctuation spectrum of the surface morphology reveals a power law $S(q_x) \sim q_x^{1/2}$. Furthermore, the local fluctuation observed in the inter-brush binary contacts and with it connected observables a pink noise ($S(f) \sim 1/f$), revealing long time correlation, where an upper time limit is not found. That in return implies that the integration of the autocorrelation function in Eq. (7.1) does not converge. On the other hand, if a slip between the brushes occurs and the approximation given by Eq. (7.2) is justified, what wave vector q_x suits best for the surface structure. The self-affine surface morphology may be approximated by a geometrical surface area eliminating the problem. These questions

remain open.

110

Chapter 8

Summary

In this work, a complex nano fluid exhibiting unique viscoelastic properties is studied via Molecular Dynamics simulations. The liquid is composed of classical coarse-grained polymers in good solvent attached to two opposing substrates. We varied the compression of the confined layers and their molecular parameters, grafting density and chain length. Solvent-free systems have been compared to systems that included explicit solvent molecules (dimers). The lubrication properties, rheological and mechanical responses, and the susceptibility to different shear rates were studied. As it was suggested by Joanny [25] and others, a separation of time scales occurs changing the fluidic response to shear, as it is known for complex non-Newtonian fluids [71].

Static Equilibrium

At static equilibrium the endgrafted chains stretch away from the substrate. With decreasing wall separation the brushes interpenetrate and establish an interfacial zone with a certain width δ. The characterization of the overlap width was determined by utilizing the Milner-Witten-Cates mean field potential, which is interpenetrated by an opposing chain segment at the outer fringe. A scaling theory was introduced which transferred the melt condition into the semi-dilute regime of the brushes leading to a theoretical description of the interfacial zone. The considered semi-dilute quantities, e.g. interpenetration depth and lateral extension, are in good agreement with the simulation results sustaining the scaling approach.

Chain segments carrying the stress exhibit a residence time inside the overlap. In the simulation "absorbing" boundaries were introduced, which were defined by the

interpenetration width δ. The approach is similar to the Kramers problem. The lifetime distribution found is dominated for short times by endmonomers entering and immediately leaving the zone, for large times a scale-free behavior decaying with a power-law exponent of -1.5 was observed. In order to understand the origin of the exponent a different approach in terms of a mean first passage time may be useful giving rise for further theoretical and numerical studies. The mean residence time of the chain segment inside the overlap introduces a critical time scale, which separates the linear from the non-Newtonian response to shear. In chapter 7 the static equilibrium of single brushes and strongly compressed bilayers were revisited. Comparing both cases, significant changes of the statistics of local fluctuations were observed. Not only the fluctuations but also the perpendicular static structure factor experimentally used to measure the monomer density profile differ significantly. The spectrum for an uncompressed brush changes from $S(q_z) \sim 1/q_z^2$ to $S(q_z) \sim 1/q_z$ in the case of a compressed bilayers, due to a non-trivial coupling between the two brushes. Furthermore, the local contact number changes the statistical properties. Long time correlations were identified in the power spectral density changing from Brownian type of noise for the uncompressed brushes to pink noise for the compressed bilayer. The local interactions are linked to the overall forces exerted from one brush to the other, those forces also exhibit pink noise. The long time correlations cannot be destroyed as long as the two brushes are interpenetrating each other. The result might be a compelling mechanism for the low frictional forces when both brushes are sliding on top of each other.

Non-stationary Shear

As in SFA experiments, oscillatory motion is used to study the fluid's response to shear. In general, the SFA setup allows to drive the system harmonically by adjusting two independent parameters, the driving amplitude and the driving frequency. In our simulation the strain is connected to the velocities of the walls and the frequency, sampling the fluid in a slightly different manner compared to experiment. The mechanical spectroscopy senses the response to extract the complex modulus $G^*(\omega)$ and its time-domain relaxation modulus $G(t)$ to identify transitions corresponding to the internal molecular time and length scales. The material's response depends on the excitation separating the response into two basic regimes, the free flow or terminal regime and the plateau regime. Both regimes are separated by a

critical inverse time ω_0. In the flow regime the brushes are able to relax. Macroscopic and microscopic observables are reaching steady state. While for the faster harmonic driving the relaxation process is suppressed, the relaxation modulus becomes dependent on the history of the flow. In terms of large amplitude oscillatory shear (LAOS) the frequency, as well as the amplitude, become larger changing the shear protocol from smoothly transition to an almost step-like inversion of the wall velocity. Due to the fast transition a linear velocity profile for both constituents (solvent and brushes) is observed.

Stationary Shear

In the limit of LAOS the responses become constant in time providing the stationary sliding regime. In the simulation, the investigated velocities are fixed and periodic boundary condition provide "infinite" surfaces such that the entire fluid reaches steady state. After the onset of motion depending on the internal degrees of freedom τ_{bilayer} the brushes reach steady state. Usually, systems with explicit solvent respond stronger to shear by squeezing the solvent out forming a fluid layer between the brushes, the brushes tilt and stretch into shear direction, while on the other hand, the bilayers reduces its height for large shear rates. Due to the formation of the fluid layer helping the brushes to lubricate the kinetic friction coefficient is significantly smaller than their solvent-free counterparts. The developed scaling theory introduces the Weissenberg number as the ratio between shear rate and a relevant relaxation time. The inverse of the relaxation time, the critical shear rate $\dot{\gamma}^* = 1/\tau$, separates the response into two general regimes, where first the fluid response linearly to the sliding strength, and second, the non-Newtonian regime. For the microscopic observable, e.g. lateral chain extension in steady state $R_{\text{g},x}^2(\dot{\gamma})$, is compared to its equilibrium extension implying a similar response. The scaling calculation reveals a power-law for the chains extension as a function of the Weissenberg number. The numerically gained data were now scaled in such that the normalized chain extension fits onto the power law by rescaling the shear rate with the critical shear rate. The found $\dot{\gamma}^*$ is also applied to the shear force response of the fluid, revealing a sublinear increase, which fits nicely to the develop scaling theory predicting a shear thinning behavior for large shear rate. Furthermore, the analytical approach is capable of reproducing not only the data stemming from very different numerical models but also from recent experimental observations. A cen-

tral result of the scaling approach is that the critical shear rate, at which the linear response regime is left and non-Newtonian behavior sets in, depends on compression and molecular parameters as

$$\dot{\gamma}^* \sim \frac{k_{\mathrm{B}}T}{\eta_{\mathrm{s}}a^3} \left[N^{-19\nu}(\rho_{\mathrm{g}}a^2)^{20\nu-13} \left(\frac{a}{D_{\mathrm{z}}}\right)^{14\nu-11} \right]^{1/6(3\nu-1)}. \tag{8.1}$$

or, with $\nu \approx 0.588$,

$$\dot{\gamma}^* \sim N^{-2.44}\rho_{\mathrm{g}}^{-0.27}D_{\mathrm{z}}^{0.6}, \tag{8.2}$$

in the limit of strongly compressed, semi-dilute brushes with Zimm dynamics, which is closely related to the chains tilting and stretching.

The scaling calculating were extended to the other limits, still strongly compressed, semi-dilute brushes with Rouse dynamics and under melt condition revealing different exponents for the microscopic and macroscopic responses.

A more accurate approach which takes into account that the chains may diffuse out of the overlap. Thus the critical shear rate depends on compression and molecular parameters as

$$\gamma^* \sim \frac{k_{\mathrm{B}}T}{\eta_{\mathrm{s}}a^3} \left[N^{-3\nu} \left(\frac{\rho_{\mathrm{g}}a^3}{D_z}\right)^{3\nu-2} \right]^{1/(3\nu-1)}, \tag{8.3}$$

or, with $\nu \approx 0.588$,

$$\gamma^* \sim N^{-2.31} \left(\frac{D_z}{\rho_{\mathrm{g}}}\right)^{0.31}. \tag{8.4}$$

Utilizing dynamic mechanical analysis where the system responses to harmonic driving reveals a critical time scale $1/\omega_0$ which is closer related to the equilibrium relaxation time of the chains segment.

The coarse-grained polymer model revealed microscopic time scales that are relevant for the transition between Newtonian and non-Newtonian behavior of the polymeric liquid. The knowledge of that time scales allows expressing the shear force response in terms of the Weissenberg number, which is growing sublinearly for large shear rates.

Appendix A

A list of simulation parameters is given which have been considered for this study.

Simulation parameter

energy scale	ϵ
length scale	σ
mass	m
time scale	$\tau_{LJ} = \sqrt{m\sigma^2/\epsilon}$
time step	$\Delta t = 2 \cdot 10^{-3}\tau_{LJ}$
temperature	$T = 1.68\epsilon/k_{\mathrm{B}}$
equilibrium bond length	$b = 0.98\sigma$
wall distance	$D_z = 12\sigma, 14.75\sigma, 17.5\sigma$
grafting density	$\rho_{\mathrm{g}} = N_{\mathrm{g}}/A$
polymerization	$N = 30, 60, 120$
DPD damping constant $\left[\sqrt{\epsilon/m\sigma}\right]$	$\gamma_{\mathrm{DPD}} = 5$

Table 2: Overview of simulation parameter

Appendix B

D	N	$\rho_{\mathrm{g}}/\rho_{\mathrm{g}}^*$ $(N=30)$	solvent	$R_{\mathrm{g},x}^2(0)$	$R_{\mathrm{g},z}^2(0)$	$\dot{\gamma}^* \cdot 10^4$	$f_x(\dot{\gamma}^*)$	η_0
12	30	1.1	+	2.78	3.17	10.5	25.5	7.5
	30	2.2	+	2.58	3.28	8.70	40.2	16.0
	30	4.4	+	2.37	3.42	5.00	69.4	13.8
	60	1.1	+	5.41	4.88	0.83	11.8	45.0
	60	2.2	+	4.26	4.69	0.57	15.3	90.0
	30	1.1	−	3.42	3.80	133	18.6	1.7
	30	2.2	−	2.98	3.68	40.0	37.3	11.0
	30	4.4	−	2.44	3.48	6.90	72.7	125.0
	60	1.1	−	6.58	5.19	6.25	12.7	25.0
	60	2.2	−	4.92	4.77	0.87	21.8	270.0
14.75	30	1.1	+	2.71	3.56	12.5	24.2	6.0
	30	2.2	+	2.51	3.96	10.5	39.2	12.3
	30	4.4	+	2.26	4.50	6.90	66.4	33.0
	60	1.1	+	5.11	5.59	0.85	10.5	45.0
	60	2.2	+	4.22	5.43	0.63	18.0	85.0
	30	1.1	−	3.37	4.59	182	13.9	0.9
	30	2.2	−	2.97	4.67	66.7	31.2	6.5
	30	4.4	−	2.49	4.66	14.3	72.8	67.0
	60	1.1	−	7.16	6.49	10.3	12.7	15.0
	60	2.2	−	5.17	5.83	1.82	21.8	145.0
17.5	30	1.1	+	2.56	3.61	15.4	24.6	5.0
	30	2.2	+	2.48	4.44	16.7	41.3	8.8
	30	4.4	+	2.12	5.57	8.51	66.4	25.0
	60	1.1	+	5.40	6.69	1.18	21.8	58.0
	60	2.2	+	4.44	6.55	0.74	15.6	85.0
	30	1.1	−	3.21	5.44	500	9.6	0.45
	30	2.2	−	2.85	5.94	118	27.8	3.9
	30	4.4	−	2.49	6.13	25.0	69.4	37.0
	60	1.1	−	7.16	7.53	14.8	12.7	10.0
	60	2.2	−	5.50	7.02	2.86	21.8	85.0

Table 3: Mean square radius of gyration, $R_{\mathrm{g},\alpha}^2(0)$, in shear ($\alpha = x$) and gradient ($\alpha = z$) directions, critical shear rate, $\dot{\gamma}^*$, critical force (see Fig. 4.10), $f_x(\dot{\gamma}^*)$, and zero shear viscosity (see Fig. 4.11) for the different parameter combinations under consideration: distance D_z between grafting planes, chain length N, and ratio between grafting density and (approximate) critical grafting density for chains of length $N = 30$ (+ and − respectively denote systems with and without explicit

Appendix C

The properties of a two composite fluids are discussed, where one fluid is composed of single polymer brush and a solvent of dimers. The brush is attached to the lower wall while dimers fill the system to the wall distance D_z to an overall density $\rho = 0.9$. Figure C-1 shows the density profile of a single brush with the solvent, the sum of both densities, and the externally chosen density. The overall density is given by the number of particles over the volume, $\rho = 0.9$ (black solid line in Figure C-1). The sum of both solvent and brush densities do not reach the overall density due to two effects. The origin of one effect is the highly symmetric walls, where the monomers are able to align in the minima of the substrates, layering occurs. The layering reaches into the system until it disappears towards the middle. The second effect concerns the larger density towards the brush profile, where more solvent is accumulated inside the brush than outside. The excluded volume per monomer may be estimated via

$$ v_{\text{ex,mono}} = 4\pi \int_0^\infty dr\, r^2 \left[1 - \exp\left(-\frac{U(r)}{k_{\text{B}} T} \right) \right] , \qquad \text{(C-1)} $$

where the interaction potential $U(r)$ includes the LJ-potential and additionally the connectivity potential is given by

$$ U(r) = U_{\text{LJ}}(r) + U_{\text{FENE}}(r) . \qquad \text{(C-2)} $$

The two connections to the next neighboring monomers of a bead inside the chains reduces the excluded volume, hence the less connected dimers need more space to occupy. The effect should be stronger when monomeric solvent is used. The effect is not only present in the solvent-brush mixture, but also between the two brushes. When both brushes are driven into steady state and tilt such that the monomer density of the brushes increases towards the wall, solvent molecules are squeezed out of the brush. This effect becomes smaller due to the smaller excluded volume

120
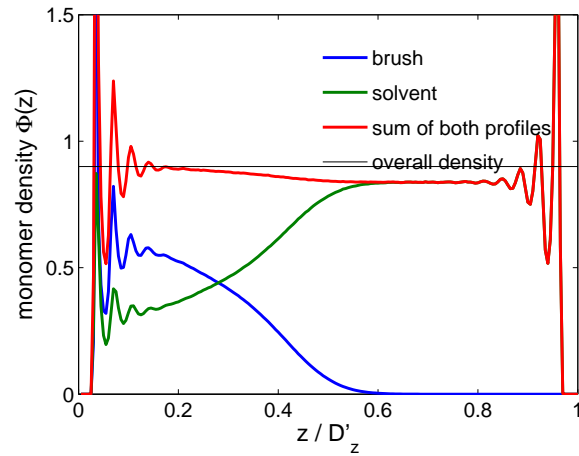
Figure C-1: Density profile of a single brush with explicit solvent confined between two walls. The overall density of the system is set to $\rho = 0.9$. The internal pressure is uniform along the gap. The excluded volume of the brush is smaller, hence more particles occupying the volume in this region.
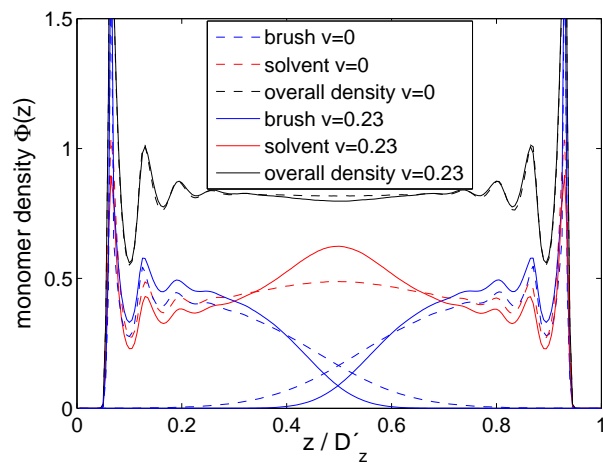
Figure C-2: The overall density of two states in stationary regime are compared. The overall density in steady state with our largest sliding velocity $v = 0.23$ remains almost constant, implying the low compressibility of the system.

effect of the brushes, the overall density reduces slightly around the symmetry axis. In Figure C-2 both overall densities at equilibrium (black dashed line) and steady state (black solid line) are shown. A slight decrease density is observed under steady state. Overall the effect is very small and proofs the low compressibility of the fluid. The thermodynamic boundary in the NVT ensemble is fulfilled by a constant pressure. Therefore, the pressure in the pure solvent-phase must be smaller than in brush-solvent composition.

Appendix D

Equilibrium Description

Throughout we follow the standard Milner-Witten-Cates (MWC)[17] strong stretching description (an equivalent one was developed by Zhulina and coworkers[18]). In the MWC theory, a grafted chain part of the brush with its free end located at a distance z_e from the grafting plane can be described by its optimal configuration only and other paths entering the partition sum can be discarded. This is equivalent to the classical approximation to quantum mechanics. MWC is expected to fail at the soft brush edge, a calculation taking into account fluctuations has been proposed to describe this outermost region. The main additional assumption in MWC is that the tension vanishes at the free chain ends. It follows that in this description the brush is a highly degenerate system all end locations being equivalent. Free ends are hence expected to diffuse through the layer and exchange their positions. Simulataneously, MWC predicts a free end distribution, $g(z)$, which is not flat. As noted by several authors (see [16] and Refs. therein), MWC is not strictly speaking a self-consistent (Mean-Field) theory.

Let us recall the brush height, h, the classical concentration profile, $\phi(Z)$, a small distance $Z \ll h$ from the edge, the correlation length in the bulk of the brush, ξ_c, and at the edge, ξ_0, according to MWC:

$$
\begin{aligned}
h &\sim aN(\rho_g a^2)^{(1-\nu)/2\nu}, \quad \phi(Z) \sim c\left(\frac{Z}{h}\right)^{(6\nu-2)/(3-2\nu)}, \\
\xi_c &\sim a(ca^3)^{\nu/(1-3\nu)}, \quad \xi_0 \sim aN^{2\nu/3}(\rho_g a^2)^{-1/6}.
\end{aligned}
\tag{D-3}
$$

The length ξ_0 describes the soft brush edge for static properties like brush interpenetration at contact or linear dynamics like flow penetration at moderate shear rates. When two brushes slightly overlap their interpenetration length equals ξ_0. In the very opposite limit of strong compression, the concentration profile is almost flat, $\phi(z) = c \sim \rho_g N/D_z$. The brushes hence can be described as molten without concen-

tration fluctuations, provided monomers are renormalized to concentration blobs of radius ξ_c and monomer content $g_c \sim (\xi_c/a)^{1/\nu}$. For a molten brush (of concentration $c \sim a^{-3}$), the classical end distribution, $g(z)$, and penetration length obey

$$g(z) \sim \frac{\rho_g z}{h\sqrt{h^2 - z^2}}, \quad L \sim \left(\frac{N^2 a^4}{h}\right)^{1/3}. \tag{D-4}$$

The end distribution is singular at the brush edge, $g(z) \sim \rho_g\sqrt{2z/h^3}$, but the ends are only weakly localized at the edge and remain marginally free. After renormalization to blobs we obtain

$$g(z) \sim \rho_g\sqrt{\frac{z}{D_z^3}},$$

$$L \sim a\left[N^{2\nu}(\rho_g a^2)^{2(1-2\nu)}\left(\frac{a}{D_z}\right)^{1-\nu}\right]^{1/3(3\nu-1)}. \tag{D-5}$$

Note that the edge singularity of the end distribution does not change upon renormalization to blobs. The end distribution strongly differs from the Alexander-de Gennes distribution.

It is instructive to estimate the penetration depth L for the upper ($D_z \sim h$) and lower boundary ($D_z \sim L$) of the strong compression regime. We obtain $L \sim a[N^{2\nu}(\rho_g a^2)^{1-3\nu}]^{1/(6\nu)}$ and $L \sim a[N^\nu(\rho_g a^2)^{1-2\nu}]^{1/(4\nu-1)}$, respectively. For $D_z \sim L$ the penetration depth merges with the isotropic chain radius at the actual brush concentration. Upon further compression the chains in the brush are not stretched but rather reflected by the surfaces, obviously the strong stretching approximation is no longer appropriate. In practice, the brush may become dense (and the equation of state assumed for the polymer solution fails) before the limit $D_z \sim L$ is reached. At the crossover to weak compression, $D_z \sim h$, each chain spans the interpenetration length with $(L/\xi_c)^2 g_c$ monomers. Inserting values according to Eqs. (D-3) and (D-5) we find $(L/\xi_c)^2 g_c \sim g_0$, i.e. the same number as for brushes that are just in contact. We may conclude that the number of monomers per chain in the interpenetration layer is almost constant over the whole weak interpenetration regime. Thus, the weak compression regime ($d = 2h - D_z \ll h$) is characterized by the correlation length

$$\xi_d \sim \xi_c\left(\frac{d}{h}\right)^{2\nu/(2-3\nu)} \tag{D-6}$$

and the interpenetration depth

$$L \sim \left(\frac{g_0}{g_c}\right)^{1/2}\xi_c \sim \xi_0\left(\frac{d}{\xi_0}\right)^{(1-2\nu)/(3-2\nu)}. \tag{D-7}$$

Inserting $\nu \approx 0.588$ the interpenetration is found to slightly decrease upon weak compression.

Linear Shear Regime The linear shear regime is tightly linked to the previous section as by definition the brush structure is only slightly disturbed and hence is assumed to be preserved to leading order.

It is convenient to start out from the case of a single brush sheared through a solvent layer. This case was thoroughly analysed in Ref. [78]. The penetration depth of the flow into the brush is ξ_0. Assuming that the same chains stay in the sheared edge all the time and sustain the hydrodynamic force, f, we could naively apply the fluctuation dissipation theorem and calculate the mean lateral deflection, $\langle R_x \rangle = f \langle R_x^2 \rangle$ ($k_B T \equiv 1$). This is not justified as chain ends exchange their position over time. Rather, a given end typically leaves the sheared layer after the relaxation time associated with ξ_0, $\tau_0 \sim \eta_s \xi_0^3$. The actual deflection of a chain end depends on its history, more precisely on the previous visits to the sheared layer. Obviously, visits done more than one lateral relaxation time ago do not matter. On the other hand, the response function to the localized shear force only decays as a weak power of time[78]. What finally matters is the average hydrodynamic force exerted on the end about one lateral relaxation time ago. An end currently located in the sheared layer is likely to be most deflected (as compared to those found deeper in the brush). One lateral relaxation time ago its probability density was spread over one isotropic radius in depth. Hence, the average force can be estimated as $\langle f \rangle \approx f \xi_0 / \sqrt{\langle R_x^2 \rangle}$ yielding

$$\frac{R_x}{\sqrt{\langle R_x^2 \rangle}} \sim f \xi_0 \sim \eta_s \xi_0^3 \dot{\gamma}, \qquad (\text{D-8})$$

when we insert the hydrodynamic force, $f \sim \eta_s \xi_0^2 \dot{\gamma}$, exerted on one end within the sheared layer. The threshold to non-Newtonian behavior corresponds to a deflection as large as the thermodynamic fluctuation, hence the critical shear rate corresponds to the relaxation frequency of the last blob, $\dot{\gamma}^* \sim 1/\eta_s \xi_0^3$.

The case of two brushes in contact sheared against each other should be very similar. Formally, there are two sources of dissipation, the drag of the polymers and the shear flow imposed to the solvent in the interface. Both give contributions scaling as $\eta_s \dot{\gamma} h \xi_0$. The drag is that of a blob through a mesh of width similar to its own size, which only marginally differs from the drag through solvent. The dissipation in the shear flow corresponds to the effective velocity drop, $\dot{\gamma} h$, through the interfacial

layer of thickness ξ_0. Taking into account chain-end exchange yields

$$\frac{R_x}{\sqrt{\langle R_x^2 \rangle}} \sim \eta_s \xi_0^3 \frac{h}{\xi_0} \dot{\gamma}. \tag{D-9}$$

This result is identical to Eq. (D-8) if we replace $\dot{\gamma}$ by the effective shear rate in the interface, $\dot{\gamma} D_z / \xi_0$.

In the weak compression regime, the drag force on a chain moving in the interface of thickness L reads $f \sim \eta_s (L/\xi_d)^2 \xi_d \dot{\gamma} D$. Chain-end exchange reduces the force by a factor of $L/\sqrt{\langle R_x^2 \rangle}$. Collecting all factors we obtain a result very similar to Eq. (D-9),

$$\frac{R_x}{\sqrt{\langle R_x^2 \rangle}} \sim \eta_s \frac{L^4}{\xi_d} \frac{D_z}{L} \dot{\gamma}. \tag{D-10}$$

In analogy to the case of brushes at contact, the relaxation time, $\eta_s L^4 / \xi_d$, of a section spanning the interface is multiplied by the effective shear rate in the interface.

In the strong compression regime, Eq. (D-10) remains valid provided ξ_d is replaced by ξ_c. It is nonetheless instructive to recast this formula into the equivalent form,

$$\frac{R_x}{\sqrt{\langle R_x^2 \rangle}} \sim \eta_s \left(\frac{N}{g_c} \right)^2 \xi_c^3 \dot{\gamma}, \tag{D-11}$$

showing that the critical shear rate can be understood as the lateral Rouse/Zimm relaxation frequency of a chain in the brush. Inserting the expression for ξ_c with $c \sim N \rho_g / D_z$ finally gives

$$\gamma^* \sim \frac{1}{\eta_s a^3} \left[N^{-3\nu} \left(\frac{\rho_g a^3}{D_z} \right)^{3\nu-2} \right]^{1/(3\nu-1)}, \tag{D-12}$$

or, with $\nu \approx 0.588$,

$$\gamma^* \sim N^{-2.31} \left(\frac{D_z}{\rho_g} \right)^{0.31}. \tag{D-13}$$

In the Rouse regime of dry, dense (non-swollen) brushes, we obtain

$$\gamma^* \sim \frac{1}{\psi (Na)^2}. \tag{D-14}$$

.

Bibliography

[1] B. Bhushan. *Handbook of Micro/Nano Tribology*. CRC Press, 1998.

[2] H.-J. Butt and M. Kappl. *Surface and Interfacial Forces*, volume 1. Wiley-VCH, Berlin, first edition, 2010.

[3] B.N.J. Persson. *Sliding Friction*. Springer, second edition, 2000.

[4] D. Dowson. *History of Tribology*. Professional Engineering Publisher, London, 1999.

[5] M. H. Müser and M. O. Robbins. Conditions for static friction between flat crystalline surfaces. *Phys. Rev. B*, 61:2335, 2000.

[6] Jean-Michel Martin Ali Erdemir, editor. *Superlubricity*. Elsevier, 1st edition, 2007.

[7] R. C. Advincula, W. J. Brittain, K. C. Caster, and J. Rühe, editors. *Polymer Brushes*. Wiley-VCH, 2005.

[8] J. Klein, D. Perahia, and S. Warburg. Forces between polymer-bearing surfaces undergoing shear. *Nature*, 352:143, 1991.

[9] Jacob Klein. Shear, friction, and lubrication forces between polymer-bearing surfaces. *Annual Review of Materials Science*, 26:581, 1996.

[10] T. Moro, Y. Takatori, K. Ishihara, T. Konno, Y. Takigawa, T. Matsushita, U. Chung, K. Nakamura, and H. Kawaguchi. Surface grafting of artificial joints with a biocompatible polymer for preventing periprosthetic osteolysis. *Nature Mat.*, 3:829, 2004.

128

[11] J. Klein. Molecular mechanisms of synovial joint lubrication. *Proceedings of the Institution of Mechanical Engineers, Part J: Journal of Engineering Tribology*, 220:691, 2006.

[12] M. van der Waarden. Stabilization of carbon-black dispersions in hydrocarbons. *J. Coll. Sci.*, 5:317, 1950.

[13] S. Alexander. Adsorption of chain molecules with a polar head a scaling description. *Journal de Physique*, 38:983, 1977.

[14] P. G. De Gennes. Conformations of polymers attached to an interface. *Macromolecules*, 13:1069, 1980.

[15] A. N. Semenov. *Sov. Phys. JETP*, 61:733, 1985.

[16] R. R. Netz and M. Schick. Classical theory of polymer brushes. *Europhys. Lett.*, page 37, 1997.

[17] S. T. Milner, T. A. Witten, and M. E. Cates. Theory of the grafted polymer brush. *Macromolecules*, 21:2610, 1988.

[18] Ye.B. Zhulina, V.A. Pryamitsyn, and O.V. Borisov. Structure and conformational transitions in grafted polymer chain layers. a new theory. *Polymer Science U.S.S.R.*, 31:205, 1989.

[19] H. C. Brinkman. A calculation of the viscous force exerted by a flowing fluid on a dense swarm of particles. *Appl. Sci. Res. A*, 1:27, 1947.

[20] Jacob Klein, Yoichiro Kamiyama, Hisae Yoshizawa, Jacob N. Israelachvili, Glenn H. Fredrickson, Philip Pincus, and Lewis J. Fetters. Lubrication forces between surfaces bearing polymer brushes. *Macromolecules*, 26:5552, 1993.

[21] G. H. Fredrickson and P. Pincus. Drainage of compressed polymer layers: dynamics of a "squeezed sponge". *Langmuir*, 7:786, 1991.

[22] J. L. Harden and M. E. Cates. Deformation of grafted polymer layers in strong shear flows. *Phys. Rev. E*, 53:3782, 1996.

[23] Y. Rabin and S. Alexander. Stretching of grafted polymer layers. *Europhys. Lett.*, 13:49, 1990.

[24] S. T. Milner. Hydrodynamic penetration into parabolic brushes. *Macromolecules*, 24:3704, 1991.

[25] Jean Francois Joanny. Lubrication by molten polymer brushes. *Langmuir*, 8:989, 1992.

[26] P. A. Schorr, T. C. B. Kwan, S. M. Kilbey, E. S. G. Shaqfeh, and M. Tirrell. Shear forces between tethered polymer chains as a function of compression, sliding velocity, and solvent quality. *Macromolecules*, 36:389, 2003.

[27] Pik-Yin Lai and Kurt Binder. Grafted polymer layers under shear: A monte carlo simulation. *J. Chem. Phys.*, 98:2366, 1993.

[28] Pik-Yin Lai and Chee-Yuen Lai. Polymer brush under strong shear. *Phys. Rev. E*, 54:6958, 1996.

[29] P. S. Doyle, E. S. G. Shaqfeh, and A. P. Gast. Rheology of "wet" polymer brushes via brownian dynamics simulation: Steady vs oscillatory shear. *Phys. Rev. Lett.*, 78:1182, 1997.

[30] P. S. Doyle, E. S. G. Shaqfeh, and A. P. Gast. Rheology of polymer brushes: A brownian dynamics study. *Macromolecules*, 31:5474, 1998.

[31] M. G. Saphiannikova, V. A. Pryamitsyn, and T. Cosgrove. Self-consistent brownian dynamics simulation of polymer brushes under shear. *Macromolecules*, 31:6662, 1998.

[32] Sauro Succi. *The Lattice Boltzmann Equation for Fluid Dynamics and Beyond (Numerical Mathematics and Scientific Computation)*. Oxford University Press, 2001.

[33] A. Malevanets and R. Kapral. Mesoscopic model for solvent dynamics. *J. Chem. Phys.*, 110:8605, 1999.

[34] M. Murat and G. S. Grest. Interaction between grafted polymeric brushes: A molecular-dynamics study. *Phys. Rev. Lett.*, 63:1074, 1989.

[35] G. S. Grest. Interfacial sliding of polymer brushes: A molecular dynamics simulation. *Phys. Rev. Lett.*, 76:4979, 1996.

130

[36] G. S. Grest. Normal and shear forces between polymer brushes. *Polymers In Confined Environments*, 138:149, 1999.

[37] T. Kreer, M. H. Müser, K. Binder, and J. Klein. Frictional drag mechanisms between polymer-bearing surfaces. *Langmuir*, 17:7804, 2001.

[38] Torsten Kreer, Kurt Binder, and Martin H. Müser. Friction between polymer brushes in good solvent conditions: Steady-state sliding versus transient behavior. *Langmuir*, 19:7551, 2003.

[39] C. M. Wijmans and B. Smit. Simulating tethered polymer layers in shear flow with the dissipative particle dynamics technique. *Macromolecules*, 35:7138, 2002.

[40] C. Pastorino, K. Binder, T. Kreer, and M. Müller. Static and dynamic properties of the interface between a polymer brush and a melt of identical chains. *J. Chem. Phys.*, 124:064902, 2006.

[41] F. Yin, D. Bedrov, G. D. Smith, and S. M. Kilbey. A langevin dynamics simulation study of the tribology of polymer loop brushes. *J. Chem. Phys.*, 127:084910, 2007.

[42] F. Yin, D. Bedrov, and G. D. Smith. A molecular simulation study of the structure and tribology of polymer brushes: Comparison of behavior in theta and good solvents. *Eur. Poly. J.*, 44:3670, 2008.

[43] D. Irfachsyad, D. Tildesley, and P. Malfreyt. Dissipative particle dynamics simulation of grafted polymer brushes under shear. *Phys. Chem. Chem. Phys.*, 4:3009, 2002.

[44] F. Goujon, P. Malfreyt, and D. J. Tildesley. Dissipative particle dynamics simulations in the grand canonical ensemble: Applications to polymer brushes. *ChemPhysChem*, 5:457, 2004.

[45] F. Goujon, P. Malfreyt, and D. J. Tildesley. The compression of polymer brushes under shear: the friction coefficient as a function of compression, shear rate and the properties of the solvent. *Molecular Physics: An International Journal at the Interface Between Chemistry and Physics*, 103:2675, 2005.

[46] F. Goujon, P. Malfreyt, and D. J. Tildesley. Mesoscopic simulation of entanglements using dissipative particle dynamics: Application to polymer brushes. *J. Chem. Phys.*, 129:034902, 2008.

[47] F. Goujon, P. Malfreyt, and D. J. Tildesley. Mesoscopic simulation of entangled polymer brushes under shear: Compression and rheological properties. *Macromolecules*, 42:4310, 2009.

[48] H. C. Öttinger. *Stochastic Processes in Polymeric Fluids: Tools and Examples for Developing Simulation Algorithms.* Springer, Berlin, 1996.

[49] M. Fixman. Construction of langevin forces in the simulation of hydrodynamic interaction. *Macromolecules*, 19:1204, 1986.

[50] Kurt Kremer and Gary S. Grest. Dynamics of entangled linear polymer melts: A molecular-dynamics simulation. *J. Chem. Phys.*, 92:5057, 1990.

[51] D. J. Tildeslay M. P. Allen. *Computer Simulation of Liquids.* Oxford University Press, 1987.

[52] T. Soddemann, B. Dünweg, and K. Kremer. Dissipative particle dynamics: A useful thermostat for equilibrium and nonequilibrium molecular dynamics simulations. *Phys. Rev. E*, 68:046702, 2003.

[53] G. S. Grest and K. Kremer. Molecular dynamics simulation for polymers in the presence of a heat bath. *Phys. Rev. A*, 33:3628, 1986.

[54] P. Espanol and P. Warren. Statistical mechanics of dissipative particle dynamics. *Europhys. Lett.*, page 191, 1995.

[55] P. Nikunen, M. Karttunen, and I. Vattulainen. How would you integrate the equations of motion in dissipative particle dynamics simulations? *Comp. Phys. Comm.*, 153:407, 2003.

[56] Kurt Binder, editor. *Monte Carlo and Molecular Dynamics Simulations in Polymer Science.* Oxford University Press, 1995.

[57] B. Dünweg and K. Kremer. Molecular dynamics simulation of a polymer chain in solution. *J. Chem. Phys.*, 99:6983, 1993.

132

[58] T. Kreer, S. Metzger, M. Müller, K. Binder, and J. Baschnagel. Static properties of end-tethered polymers in good solution: A comparison between different models. *J. Chem. Phys.*, 120:4012, 2004.

[59] W. T. Ashurst and W. G. Hoover. Dense-fluid shear viscosity via nonequilibrium molecular dynamics. *Phys. Rev. A*, 11:658, 1975.

[60] J. H. Irving and John G. Kirkwood. The statistical mechanical theory of transport processes. iv. the equations of hydrodynamics. *J. Chem. Phys.*, 18:817, 1950.

[61] Michael Rubinstein and Ralph H. Colby. *Polymer Physics*. Oxford University Press, 2003.

[62] C. Pastorino, T. Kreer, M. Müller, and K. Binder. Comparison of dissipative particle dynamics and langevin thermostats for out-of-equilibrium simulations of polymeric systems. *Phys. Rev. E*, 76:026706, 2007.

[63] T. A. Witten, L. Leibler, and P. A. Pincus. Stress relaxation in the lamellar copolymer mesophase. *Macromolecules*, 23:824, 1990.

[64] P. G. De Gennes. *Scaling Concepts in Polymer Physics*. Cornell University Press, 1980.

[65] K. Binder. Scaling concepts for polymer brushes and their test with computer simulation. *Eur. Phys. J. E*, 9:293, 2002.

[66] F. Varnik, J. Baschnagel, and K. Binder. Static and dynamic properties of supercooled thin polymer films. *Eur. Phys. J. E*, 8:175, 2002.

[67] D. I. Dimitrov, A. Milchev, and K. Binder. Polymer brushes in solvents of variable quality: Molecular dynamics simulations using explicit solvent. *J. Chem. Phys.*, 127:084905, 2007.

[68] D. Irfachsyad, D. Tildesley, and P. Malfreyt. Dissipative particle dynamics simulation of grafted polymer brushes under shear. *Phys. Chem. Chem. Phys.*, 4:3008, 2002.

[69] C. Sendner and R. Netz. Single flexible and semiflexible polymers at high shear: Non-monotonic and non-universal stretching response. *Eur. Phys. J. E*, 30:75, 2009.

[70] H. Bruuns. *Theoretical Microfluidics*. Oxford University Press, 2007.

[71] J. D. Ferry. *Viscoelastic Properties of Polymers*. Wiley & Sons, New York, 1980.

[72] F. Goujon. *Simulation Numeriques mesoscopiques de brosses de Polymers sous compression et cisaillement*. PhD thesis, Universite Blaise Pascal, Clermont-Ferrand, 2003.

[73] M. Urbakh, L. Daikhin, and J. Klafter. Velocity profiles and the brinkman equation in nanoscale confined liquids. *Europhys. Lett.*, 32:125, 1995.

[74] P. S. Doyle, B. Ladoux, and J.-L. Viovy. Dynamics of a tethered polymer in shear flow. *Phys. Rev. Lett.*, 84:4769, 2000.

[75] M. Müller and C. Pastorino. Cyclic motion and inversion of surface flow direction in a dense polymer brush under shear. *Europhys. Lett.*, 81:28002, 2008.

[76] M. Müller and C. Pastorino. Cyclic motion and inversion of surface flow direction in a dense polymer brush under shear. *Europhys. Lett.*, 81:28002, 2008.

[77] C. L. M. H. Navier. Sur les lois du mouvement des fluides. *Mem. Acad. Roy. Sci. Inst. France*, 6:389, 1823.

[78] F. Clement, T. Charitat, A. Johner, and J.-F. Joanny. Self-assembled layers under flow: Stabilization by chain end exchange. *Europhys. Lett.*, 54:65, 2001.

[79] M. Wilhelm. Fourier-transform rheology. *Macromolecular Materials and Engineering*, 287:83, 2002.

[80] Gert Strobl. *The Physics of Polymers*. Springer Berlin Heidelberg New Yorkk, 1997.

[81] M. Chen, W. H. Briscoe, S. P. Armes, and J. Klein. Lubrication at physiological pressures by polyzwitterionic brushes. *Science*, 323:1698, 2009.

[82] William W. Graessley. *Polymeric Liquids and Networks: Dynamics and Rheology.* Taylor & Francis Group, 2008.

[83] Ramanan Krishnamoorti and Emmanuel P. Giannelis. Strain hardening in model polymer brushes under shear. *Langmuir*, 17:1448, 2001.

[84] Christopher O. Klein, Hans W. Spiess, Andreea Calin, Corneliu Balan, and Manfred Wilhelm. Separation of the nonlinear oscillatory response into a superposition of linear, strain hardening, strain softening, and wall slip response. *Macromolecules*, 40:4250, 2007.

[85] T. Kuhl T. Kreer. LAOS problem of polymer brushes in SFA experiment. private communication.

[86] S. N. Ganeriwala and C. Rotz. Fourier transform mechanical analysis for determining the nonlinear viscoelastic properties of polymers. *Polymer Engineering & Science*, 27:165, 1987.

[87] Jean-Pierre Hansen and I.R. McDonald. *Theory of Simple Liquids.* Academic Press, 1989.

[88] Y. Gratton and G. W. Slater. Molecular dynamics study of tethered polymers in shear flow. *Eur. Phys. J. E*, 17:455, 2005.

[89] R. Delgado-Buscalioni. Cyclic motion of a grafted polymer under shear flow. *Phys. Rev. Lett.*, 96:088303, 2006.

[90] L. Bocquet and J.-L. Barrat. Hydrodynamic boundary conditions and correlation functions of confined fluids. *Phys. Rev. Lett.*, 70:2726, 1993.

[91] L. Bocquet and J.-L. Barrat. Hydrodynamic boundary conditions, correlation functions, and kubo relations for confined fluids. *Phys. Rev. E*, 49:3079, 1994.

[92] L. Bocquet and J.-L. Barrat. Flow boundary conditions from nano- to microscales. *Soft Matter*, 3:685, 2007.

[93] C. Pastorino, K. Binder, and M. Muüller. Coarse grained description of a brush-melt interface in equilibrium and under flow. *Macromolecules*, 42:401, 2009.

[94] P. Auroy, Y. Mir, and L. Auvray. Local structure and density profile of polymer brushes. *Phys. Rev. Lett.*, 69:93, 1992.

[95] W. A. Hamilton, G. S. Smith, N. A. Alcantar, J. Majewski, R. G. Toomey, and T. L. Kuhl. Determining the density profile of confined polymer brushes with neutron reflectivity. *J. Polym. Sci. Part B: Polym. Phys.*, 42:3290, 2004.

[96] B. Akgun, D. R. Lee, H. Kim, H. Zhang, O. Prucker, J. Wang, J. Rühe, and M. D. Foster. Self-affine surfaces of polymer brushes. *Macromolecules*, 40:6361, 2007.

[97] G. H. Fredrickson, A. Ajdari, L. Leibler, and J. P. Carton. Surface modes and deformation energy of a molten polymer brush. *Macromolecules*, 25:2882, 1992.

[98] Athanasios Papoulis. *Probability, Random Variables, and Stochastic Processes.* McGraw-Hill Kogakusha, 1991.

[99] W. Li. A bibliograph on 1/f noise. http://www.nslij-genetics.org/wli/1fnoise/. `http://www.nslij-genetics.org/wli/1fnoise/`.

[100] J.B. Johnson. The schottky effect in low frequency circuits. *Phys. Rev.*, 26:71, 1925.

[101] E. Milotti. A pedagogical review of 1/f noise. *arxiv.org*, physics/0204033, 2002.

[102] A. McWhorter. 1/f noise and related surface effects in germanium. *Semiconductor Surface Physics*, 1956.

[103] P. Bak, C. Tang, and K. Wiesenfeld. Self-organized criticality: An explanation of the 1/f noise. *Phys. Rev. Lett.*, 59:381, 1987.